

DEPARTMENT OF PHYSICS, UNIVERSITY OF JYVÄSKYLÄ

**JET TRANSVERSE MOMENTUM DISTRIBUTIONS
MEASURED BY ALICE**

**BY
TOMAS SNELLMAN**

PHD thesis

Supervisors: Jan Rak, Dong Jo Kim

Jyväskylä, Finland
December, 2018

3 Contents

4	1	Introduction	5
5	1.1	Quantum chromodynamics	7
6	1.1.1	Foundation of QCD	7
7	1.1.2	Asymptotic Freedom	10
8	1.2	Heavy-ion physics	13
9	1.2.1	History	13
10	1.3	Features of Heavy-Ion Collisions	15
11	1.3.1	Collision Geometry	15
12	1.3.2	Collective motion	19
13	1.4	Hard processes	25
14	1.4.1	pQCD factorization	25
15	1.4.2	Jet showering	27
16	1.4.3	Soft gluon radiation and angular ordering	29
17	1.4.4	Jet hadronisation	30
18	1.4.5	Interactions between jet and medium	34
19	1.4.6	New paradigm of jet Quenching	38
20	1.5	QGP in Small systems	44
21	1.5.1	Collective phenomena	44
22	1.5.2	Absence of jet quenching	45
23	1.5.3	Centrality determination in small systems	48
24	2	Experimental Setup	51
25	2.1	CERN	51
26	2.2	Large Hadron Collider	52
27	2.2.1	LHC experiments	53
28	2.3	ALICE	54
29	2.3.1	Tracking	55
30	2.3.2	TPC	57
31	2.3.3	TPC upgrade	57
32	2.3.4	Particle identification	61
33	2.3.5	Electromagnetic Calorimeter	62
34	2.3.6	Forward and trigger detectors	63
35	2.3.7	Muon spectrometer	65
36	2.3.8	Triggers	65

37	3 Event and track selection	68
38	3.1 Event selection	68
39	3.2 Track reconstruction	68
40	3.3 Cluster selection	72
41	4 Analysis method	74
42	4.1 Jet Finding	74
43	4.1.1 Anti k_T algorithm	74
44	4.2 Definition of j_T	75
45	4.3 Unfolding detector effects	77
46	4.3.1 Bayesian unfolding	78
47	4.3.2 Toy Monte Carlo	80
48	4.3.3 Pythia Response matrices	81
49	4.3.4 Unfolding algorithm	82
50	4.3.5 Unfolding closure test	82
51	4.4 Background	85
52	4.4.1 Perpendicular cone background	85
53	4.4.2 Random background	86
54	4.4.3 Auto-correlations	86
55	4.4.4 Comparing background methods	87
56	4.5 Fitting	88
57	5 Systematic errors	90
58	5.1 Background	90
59	5.2 Unfolding	90
60	5.2.1 Effect of number of iterations	91
61	5.2.2 Effect of different prior	93
62	5.2.3 Effect of p_T truncation	93
63	5.3 Tracking	94
64	5.4 EMCAL clusters	95
65	5.5 Summary/Combining systematics	95
66	5.6 Additional checks	96
67	5.6.1 Comparison between A and C side	96
68	6 Results	98
69	6.1 High multiplicity	99
70	7 Discussion	102
71	7.1 Comparing dihadron and jet j_T results	102
72	7.1.1 Different R parameters	104
73	7.1.2 Leading tracks versus jet	105

⁷⁴ 8 Summary	108
⁷⁵ Appendices	110
⁷⁶ A Additional graphs	110

77 1 Introduction

78 This thesis focuses on studying Quantum Chromodynamics (QCD) [1], a part of
79 the standard model of particle physics [2], which is the theory describing the strong
80 interactions. Strong interaction is the force responsible for interactions that holds
81 the nucleus of an atom together. Fundamentally it describes the interactions be-
82 tween quarks and gluons, the elementary constituents of the building blocks of the
83 nucleus, protons and neutrons. Because of specifics of this interaction quarks and
84 gluons, together dubbed partons, can never be seen free [?]. Under ordinary con-
85 ditions they are confined into bound states called hadrons. In extreme conditions
86 they can form a medium of asymptotically free quarks and gluons, quark-gluon
87 plasma (QGP) [3].

88 Indirectly the effect of quarks can be studied using for example jets, collimated
89 streams of particles observed in high energy particle collisions [4]. The physics
90 of these jets is the primary topic discussed in this thesis. Understanding jets is
91 important when one is interested in the processes that produce the partons that
92 eventually fragment into jets. By themselves jets can provide an insight into QCD
93 when the fragmentation is studied. Jets can also be used as probes of the QGP
94 medium.

95 Experimentally jets are often studied with a jet reconstruction algorithm which
96 clusters observed tracks to find a reasonable estimate of the initial parton. That is
97 also the case in this thesis. The main observable studied is the jet fragmentation
98 transverse momentum j_T which is defined as the perpendicular component of the
99 momentum of jet constituents with respect to the jet axis, the best estimate of
100 the initial parton. j_T measures the transverse nudge that fragmentation products
101 receive.

102 The analysis studies collisions between protons and lead nuclei. Originally
103 meant as a reference for lead-lead collisions to rule out possible cold nuclear mat-
104 ter effects [5]; effects caused by the regular 'cold' nuclear matter of a nucleus
105 as opposed to QGP. No cold nuclear matter effects have been observed [5], but
106 p–Pb collisions have provided interesting physics by themselves. Many of the col-
107 lective phenomena that in Pb–Pb collisions were attributed to QGP have been
108 observed in high multiplicity p–Pb collisions [6] and even in ultra high multiplicity
109 pp collisions [6]. However observables of jet modification show no conclusive
110 signals in p–Pb collisions [5, 6].

111 This thesis is organised as follows: Chapter 1 first gives a general introduction
112 into the history and properties of QCD and Heavy-Ion physics. It is followed by a
113 description of hard processes, jet fragmentation and hadronisation and how these
114 processes might look like in a Heavy-Ion environment. Finally there is a discussion
115 on the physics of small systems.

116 The experimental setup that was used to collect the data in this thesis is

117 described in Chapter 2. It starts by explaining the accelerator facilities at CERN
118 and LHC in more detail. This is followed by a description of the ALICE experiment
119 and its sub-detectors as all measurements used in this thesis come from ALICE. A
120 part of Chapter 2 is dedicated to coming upgrades of ALICE as this a timely topic.
121 In 2019-2020 ALICE will be upgraded and I have made a personal contribution to
122 the TPC upgrade.

123 Chapter 3 gives a description of the event, track and cluster selection criteria
124 used in the analysis. This is followed in Chapter [?] by the specific analysis
125 methods used in this thesis. First the jet reconstruction algorithm used, anti-
126 k_T , is described. Chapter [?] continues by introducing the j_T observable, how
127 it is obtained and what further methods are used to get the signal distributions.
128 Finally the fitting method used for the final results is described. Chapter 5 gives
129 the different systematic uncertainties that arise from the analysis.

130 Finally the results from the analysis are presented in Chapter 6. The results
131 are compared to PYTHIA and Herwig Monte Carlo generators. Further discussion
132 of the results is given in Chapter 7 when the results are compared to j_T results
133 obtained with a different analysis method. Chapter 8 summarises the main results
134 and gives an outlook for future.

135 **1.1 Quantum chromodynamics**

136 **1.1.1 Foundation of QCD**

137 There are four known basic interactions in the universe: gravity, electromagnetic,
138 weak and strong interactions. The standard model of particle physics [2] includes
139 three of these, electromagnetic, weak and strong interactions. The fourth one,
140 gravity, is described well in all but the most extreme of cases by the theory of
141 general relativity [7]. The standard model is a quantum field theory where particle
142 interactions are dictated by local gauge symmetries [4].

143 The first interaction included in the standard model was the electromagnetic
144 interaction. The foundations of quantum field theory and Quantum Electrody-
145 namics (QED) were already laid out by the work by Dirac in 1927 [8]. The full
146 theory of QED was formulated in 1946-1949 by Tomonaga [9], Schwinger [10, 11],
147 Feynman [12]

148 Motivated by the success of a quantum field theory approach for the elec-
149 tromagnetic interaction physicists started working on the remaining interactions.
150 However, the weak and strong nuclear interactions proved more challenging to
151 formulate [13]. In the end the weak interaction was unified with the electromag-
152 netic interaction into the electroweak theory. The final theory was formulated by
153 Glashow [14], Salam [15] and Weinberg [16].

154 The theory of strong interactions became to be known as Quantum Chromo-
155 dynamics (QCD). The search for a theory of strong interactions began after the
156 formulation of QED and drew further inspiration from the introduction of new
157 powerful particle accelerators that were capable of particle physics research in the
158 1950s. Before this particles were mainly discovered from cosmic rays. Positrons,
159 neutrons and muons were discovered in the 1930s and charged pions were discov-
160 ered in 1947 [17, 18]. The neutral pion was discovered in 1950 [19].

161 The Lawrence Berkeley National Laboratory started the Bevalac accelerator in
162 1954, Super Proton Synchrotron (SPS) in CERN began operating in 1959 and the
163 Alternating Gradient Synchrotron (AGS) at Brookhaven started in 1960. With
164 an energy of 33 GeV AGS was the most powerful accelerator of that time. By the
165 beginning of 1960s several new particles had been discovered. These included an-
166 tiprotons [20], antineutrons [21], Δ -particles and the six hyperons (Ξ^0 [22], Ξ^- [23],
167 Σ^\pm [24], Σ^0 [25] and Λ [26]).

168 Facing this avalanche of new particles, physicists started the search for symme-
169 tries within them. Already in 1932 Heisenberg [27] had proposed an isospin model
170 to explain similarities between the proton and the neutron. In 1962 Gell-Mann
171 and Ne’eman presented that particles sharing the same quantum numbers (spin,
172 parity) could be organised using the symmetry of SU(3). [28] Heisenberg’s Isospin
173 model followed the symmetry of SU(2). Using the SU(3) model known baryons

¹⁷⁴ and mesons could be presented as octets. This also lead to the discovery of the
¹⁷⁵ Ω^- [29] particle since this was missing from the SU(3) decouplet that included
¹⁷⁶ heavier baryons.

¹⁷⁷ The most simple representation of SU(3) was a triplet. Inside this triplet
¹⁷⁸ particles would have electric charges $2/3$ or $-1/3$. However, these had not been
¹⁷⁹ detected. In 1964 Gell-Mann [30] and Zweig [31] proposed that baryons and mesons
¹⁸⁰ would be bound states of these three hypothetical triplet particles that Gell-Mann
¹⁸¹ called quarks and Zweig called aces. Now we know that these are the u , d and s
¹⁸² quarks. However, this original quark model without colour was violating the Pauli
¹⁸³ exclusion principle. For example the Ω^- particle is comprised of three s quarks,
¹⁸⁴ two of which would have exactly the same quantum states, since spin can only
¹⁸⁵ have two values.

¹⁸⁶ The idea of colour had already been presented by Greenberg in 1964 [32]. In
¹⁸⁷ 1971 Gell-Mann and Fritzsch presented their model [33], which solved the antisym-
¹⁸⁸ metry problem. They added a colour quantum number to quarks, which separated
¹⁸⁹ quarks of the same species. In the new colour model the baryonic wave function
¹⁹⁰ became

$$(qqq) \rightarrow (q_r q_g q_b - q_g q_r q_b + q_b q_r q_g - q_r q_b q_g + q_g q_b q_r - q_b q_g q_r), \quad (1)$$

¹⁹¹ The colour model was also supported by experimental evidence. The decay rate
¹⁹² of a neutral pion with the addition of colours is

$$\Lambda(\pi^0 \rightarrow \gamma\gamma) = \frac{\alpha^2}{2\pi} \frac{N_c^2}{3^2} \frac{m_\pi^3}{f_\pi^2}. \quad (2)$$

¹⁹³ For $N_c = 3$ this gives 7.75 eV and the measured value is (7.86 ± 0.54) eV [34].

¹⁹⁴ Another observable that combines the colour information also to the number
¹⁹⁵ of quark flavours is the Drell-Ratio R [35]

$$R = \frac{\sigma(e^+ + e^- \rightarrow \text{hadrons})}{\sigma(e^+ + e^- \rightarrow \mu^+ + \mu^-)} = N_c \sum_f Q_f^2. \quad (3)$$

¹⁹⁶ This ratio has the numerical value 2 when including the three light quarks u , d
¹⁹⁷ and s . When the collision energy reaches the threshold of heavy quark (c and
¹⁹⁸ b) production processes this increases to $^{10}/3$ (for $f = u, d, s, c$) and $^{11}/3$ (for $f =$
¹⁹⁹ u, d, s, c, b). The energy threshold ($\sqrt{s} \approx 350$ GeV) of $t\bar{t}$ production, has not been
²⁰⁰ reached so far by any e^+e^- colliders.

²⁰¹ The colour model explained why no free quarks had been observed as only
²⁰² colour neutral states are possible. The simplest ways of producing a colour neu-
²⁰³ tral object are the combination of three quarks, and the combination of a quark-
²⁰⁴ antiquark pair. These are known as baryons and mesons.

205 First experimental indication of the existence of quarks came in 1969 when a
206 series of experiments at the Stanford Linear Accelerator Center (SLAC) revealed
207 that protons and neutrons appeared to have some substructure [?, 36]. For this
208 discovery they eventually received the Nobel Prize in Physics in 1990 [37]. Bjorken
209 demonstrated that these results could be explained if protons and neutrons were
210 composed of virtually noninteracting pointlike particles [38, 39]. Feynman [40]
211 interpreted these objects as real particles and suggested they would be the quarks
212 of Gell-Mann’s model. At the time, however, this seemed mysterious; if all strongly
213 interacting particles, hadrons, were composed of quarks, then quarks should surely
214 be strongly interacting themselves. Why would they appear to be almost free
215 inside hadrons? This turned out to be a key clue in formulating the theory of
216 strong interactions. [13]

217 After the addition of colour the main ingredients of QCD had been established.
218 The final quantum field theory of Quantum Chromodynamics formed quickly be-
219 tween 1972 and 1974. Main part of this was the work by Gross, Wilczek, Politzer
220 and George for non-abelian gauge field theories [1, 41–44]. The work showed that
221 quarks would indeed be asymptotically free in a non-abelian theory, which ex-
222 plained the results from SLAC. Gross, Wilczek and Politzer received the Nobel
223 Prize in Physics for their work [45]. The role of gluons as a colour octet was pre-
224 sented by Fritzsch, Gell-Mann and Leutwyler in 1973 [46]. The theory had now 8
225 massless gluons to mediate the strong interaction.

226 The quark model was extended in 1974 when the discovery of the charm quark
227 and the first charmed hadron, J/Ψ , was simultaneously published by teams from
228 the SLAC [47], from Brookhaven National Laboratory [48] and from the ADONE
229 collider in Frascati, Italy [49]. In 1976 the Nobel Prize in Physics was awarded to
230 Richter and Ting for the discovery of the charm quark [?]. The existence of a fourth
231 quark had already been speculated in 1964 by Bjorken and Glashow [50], but a
232 proper prediction was provided by Glashow, Iliopoulos and Maiani in 1970 [14]
233 based on symmetries between leptons and quarks in weak interactions.

234 However, these gluons had not been discovered. Indirect evidence of the ex-
235 istence had been seen as it was observed that only about half of the momentum
236 of protons was transported by the quarks [51]. Direct evidence should be seen in
237 electron-electron collisions as a third, gluonic, jet in addition to two quark jets.
238 Three jet events were first seen in 1979 at the PETRA accelerator at DESY [52–54].

239 The two remaining quarks, bottom and top, were introduced by Kobayashi
240 and Maskawa to explain CP-violation [55]. For this they received the Nobel Prize
241 in Physics in 2008 [56]. Bottom quark was discovered soon after, in 1977, at
242 Fermilab [57]. The heaviest quark, top quark, would eventually be discovered in
243 1995 by the CDF [58] and DØ [59] experiments at Fermilab.

244 **1.1.2 Asymptotic Freedom**

245 In Quantum Electrodynamics (QED) the electric charge is screened. In the vicinity
246 of a charge, the vacuum becomes polarized. Virtual charged particle-antiparticle
247 pairs around the charge are arranged so that opposing charges face each other.
248 Since the pairs also include an equal amount opposite charge compared to the
249 original charge the average charge seen by an observer at a distance is smaller.
250 When the distance to the charge increases the effective charge decreases until the
251 coupling constant of QED reaches the fine-structure constant $\alpha = \frac{1}{137}$. [4]

252 Contrary to QED, QCD is a non-abelian theory. In other words the generators
253 of the symmetry group of QCD, SU(3), do not commute. This has the practical
254 consequence that gluons interact also with other gluons, whereas in QED the
255 neutral carrier particles, photons, only interact with charged particles. There
256 is screening also in QCD because of the colour charges, but in addition to that
257 there is antiscreening because of the gluon interactions. In QCD the antiscreening
258 effect dominates over screening. Thus for larger distances to the colour charge
259 the coupling constant is larger. This explains why no free colour charges can be
260 observed. When the distance between charges increases the interaction strengthens
261 until it is strong enough to produce a new quark-antiquark pair. On the other
262 hand, at very small distances the coupling constant approaches zero. This is
263 called asymptotic freedom. [4]

264 In 1975 Collins [60] predicted a state where individual quarks and gluons are
265 no longer confined into bound hadronic states. Instead they form a bulk QCD
266 matter that Edward Shuryak called Quark-Gluon plasma in his 1980 review of
267 QCD and the theory of superdense matter [3]. QGP can be seen as a separate
268 state of matter. A schematic view of a phase diagram for QCD matter is shown
269 in Fig. 1.

270 In the early universe at the age of 10^{-6} s after the Big Bang the conditions
271 preferred the existence of QGP instead of hadronic matter. Nowadays bulk QCD
272 matter, its properties and its phase transitions between hadronic matter and the
273 quark-gluon plasma (QGP) can be explored in the laboratory, through collisions
274 of heavy atomic nuclei at ultra-relativistic energies. The study of QCD matter at
275 high temperature is of fundamental and broad interest. The phase transition in
276 QCD is the only phase transition in a quantum field theory that can be probed by
277 any present or foreseeable technology.

278 One important property of the QGP is the shear viscosity to entropy ratio,
279 η/s . It is believed that this ratio has an universal minimum value of $1/4\pi \approx 0.08$,
280 among all substances in nature. This limit would be reached in the strong coupling
281 limit of certain gauge theories [62]. The temperature dependance of the ratio is
282 shown in Fig. 2. The minimum value of η/s is found in the vicinity of the critical
283 temperature, T_c [63]. Finding the η/s values in QGP matter would therefore also

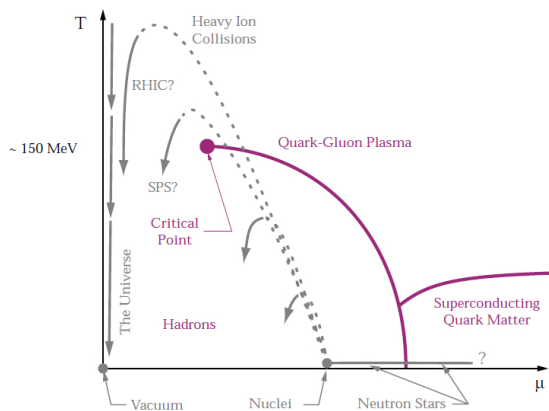


Figure 1: A schematic outline for the phase diagram of QCD matter at ultra-high density and temperature. The quark chemical potential μ that is on the x-axis represents the imbalance between quarks and antiquarks. At zero temperature this corresponds to the number of quarks but at higher temperatures there are also additional pairs of quarks and antiquarks. Along the horizontal axis the temperature is zero, and the density is zero up to the onset transition where it jumps to nuclear density, and then rises with increasing μ . Neutron stars are in this region of the phase diagram, although it is not known whether their cores are dense enough to reach the quark matter phase. Along the vertical axis the temperature rises, taking us through the crossover from a hadronic gas to the quark-gluon plasma. This is the regime explored by high-energy heavy-ion colliders. [61]

²⁸⁴ provide a way of determining the critical point of QCD matter.

²⁸⁵ The η/s value for the matter created in Au-Au collisions at RHIC ($\sqrt{s_{NN}} =$
²⁸⁶ 200 GeV) has been estimated to be 0.09 ± 0.015 [63], which is very close to the
²⁸⁷ lowest value for a wide class of thermal quantum field theories [62] for all relativistic
²⁸⁸ quantum field theories at finite temperature and zero chemical potential. This
²⁸⁹ suggests that the the matter created goes through a phase where it is close to the
²⁹⁰ critical point of QCD.

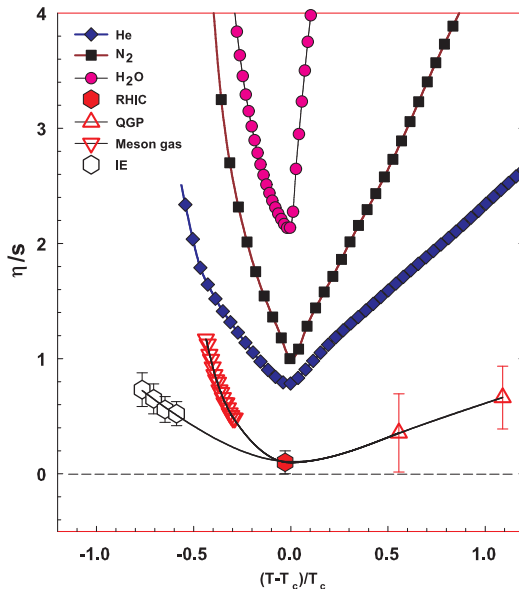


Figure 2: η/s as a function of $(T - T_c)/T_c$ for several substances as indicated. The $\eta/s = 0.09 \pm 0.015$ estimate at RHIC comes from Au-Au collisions at $\sqrt{s_{NN}} = 200$ GeV. The calculated values for the meson-gas have an associated error of $\sim 50\%$. The lattice QCD value $T_c = 170$ MeV is assumed for nuclear matter. The lines are drawn to guide the eye. [63]

291 **1.2 Heavy-ion physics**

292 The Quark Gluon Plasma (QGP) is experimentally accessible by colliding heavy-
293 ions at high energies. Nowadays research of Heavy-Ion Collisions is mainly per-
294 formed at two particle colliders; The Relativistic heavy-ion Collider (RHIC) at
295 BNL in New York, USA and the Large Hadron Collider (LHC) at CERN in Switzer-
296 land. Energy densities at these colliders should be enough to produce QGP and
297 convincing evidence of the creation has been seen at both colliders. Complimen-
298 tary research with heavy nuclei is also performed at the Super Proton Synchrotron
299 (SPS) at CERN.

300 The development of heavy-ion physics is strongly connected to the development
301 of particle colliders. Experimental study of relativistic heavy-ion collisions has been
302 carried out for three decades, beginning with the Bevalac at Lawrence Berkeley
303 National Laboratory (LBNL) [64], and continuing with the AGS at Brookhaven
304 National Laboratory (BNL) [65], CERN SPS [66], RHIC at BNL and LHC at
305 CERN.

306 **1.2.1 History**

307 The first heavy-ion collisions were performed at the Bevalac experiment at the
308 Lawrence Berkeley National Laboratory [64] and at the Joint Institute for Nu-
309 clear Research in Dubna [67] at energies up to 1GeV per nucleon. In 1986 the
310 Super Proton Synchrotron (SPS) at CERN started to look for QGP signatures in
311 O+Pb collisions. The center-of-mass energy per colliding nucleon pair ($\sqrt{s_{NN}}$)
312 was 19.4 GeV [66]. These experiments did not find any decisive evidence of the
313 existence of QGP. In 1994 a heavier lead (Pb) beam was introduced for new experi-
314 ments at $\sqrt{s_{NN}} \approx 17$ GeV. At the same time the Alternating Gradient Synchrotron
315 (AGS) at BNL, Brookhaven collided ions up to ^{32}S with a fixed target at energies
316 up to 28 GeV [65]. In 2000 CERN [68] presented compelling evidence for the ex-
317 istence of a new state of matter. Now SPS is used with 400 GeV proton beams
318 for fixed-target experiments, such as the SPS heavy-ion and Neutrino Experiment
319 (SHINE) [69], which tries to search for the critical point of strongly interacting
320 matter.

321 The Relativistic heavy-ion Collider (RHIC) at BNL in New York, USA started
322 its operation in 2000. The top center-of-mass energy per nucleon pair at RHIC,
323 200 GeV, was reached in the following years. The results from the experiments at
324 RHIC have provided a lot of convincing evidences that QGP was created [70–73].
325 The newest addition to the group of accelerators capable of heavy-ion physics is the
326 Large Hadron Collider (LHC) at CERN, Switzerland. LHC started operating in
327 November 2009 with proton-proton collisions. First Pb-Pb heavy-ion runs started
328 in November 2010 with $\sqrt{s_{NN}} = 2.76$ TeV, over ten times higher than at RHIC.

Since then LHC has provided both Pb–Pb and p–Pb collisions and a short period of XeXe collisions. Table 1 shows a summary of these. Among the six experiments at LHC, the Large Ion Collider Experiment (ALICE) is dedicated to heavy-ion physics. Also CMS and ATLAS have active heavy-ion programs and LHCb uses its SMOG [74] to perform unique fixed target collisions with heavy ions.

Table 1: Summary of datasets. The integrated luminosities are from ALICE.

Run 1 (2009-2013)			Run 2 (2015-2018)		
pp	0.9 TeV	$\sim 200 \mu\text{b}^{-1}$	pp	5.02 TeV	$\sim 1.3 \text{ pb}^{-1}$
	2.76 TeV	$\sim 100 \text{ nb}^{-1}$		13.0 TeV	$\sim 25 \text{ pb}^{-1}$
	7.0 TeV	$\sim 1.5 \text{ pb}^{-1}$	p–Pb	5.02 TeV	$\sim 3 \text{ nb}^{-1}$
	8.0 TeV	$\sim 2.5 \text{ pb}^{-1}$		8.16 TeV	$\sim 25 \text{ nb}^{-1}$
p–Pb	5.02 TeV	$\sim 15 \text{ nb}^{-1}$	XeXe	5.44 TeV	$\sim 0.3 \mu\text{b}^{-1}$
Pb–Pb	2.76 TeV	$\sim 75 \mu\text{b}^{-1}$	Pb–Pb	5.02 TeV	$\sim 1 \text{ nb}^{-1}$

334 1.3 Features of Heavy-Ion Collisions

335 1.3.1 Collision Geometry

336 In contrast to protons atomic nuclei are objects with considerable transverse size.
337 The properties of a heavy-ion collision depend strongly on the impact parameter
338 \vec{b} which is the vector connecting the centres of the two colliding nuclei at their
339 closest approach. One illustration of a heavy-ion collision is shown in Fig. 3.

340 Impact parameter defines the reaction plane which is the plane spanned by b
341 and the beam direction. Ψ_{RP} gives the angle between the reaction plane and some
342 reference frame angle. Experimentally the reference frame is fixed by the detector
343 setup. Reaction plane angle cannot be directly measured in high energy nuclear
 collisions, but it can be estimated with the event plane method [75].

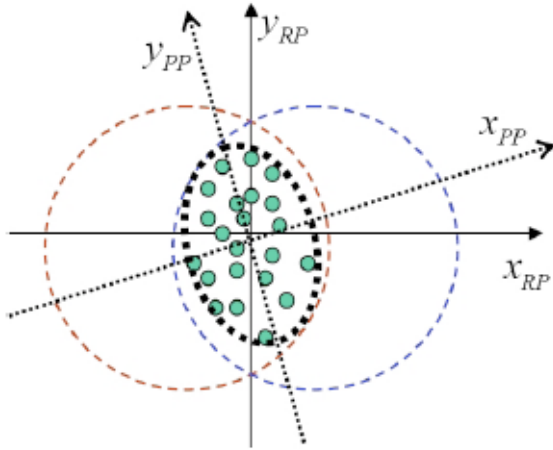


Figure 3: The definitions of the Reaction Plane and Participant Plane coordinate systems [76]. The dashed circles represent the two colliding nuclei and the green dots are partons that take part in the collision. x_{PP} and x_{RP} are the participant and reaction planes. The angle between x_{RP} and x_{PP} is given by Eq. (4). y_{PP} and y_{RP} are lines perpendicular to the participant and reaction planes.

344
345 Participant zone is the area containing the participants. The distribution of
346 nucleons in the nucleus exhibits time-dependent fluctuations. Because the nucleon
347 distribution at the time of the collision defines the participant zone, the axis of
348 the participant zone fluctuates and can deviate from the reaction plane. The angle
349 between the participant plane and the reaction plane is defined by [77]

$$\psi_{PP} = \arctan \frac{-2\sigma_{xy}}{\sigma_y^2 - \sigma_x^2 + \sqrt{(\sigma_y^2 - \sigma_x^2)^2 + 4\sigma_{xy}^2}}, \quad (4)$$

350 where the σ -terms are averaged over the energy density.

$$\sigma_y^2 = \langle y^2 \rangle - \langle y \rangle^2, \sigma_x^2 = \langle x^2 \rangle - \langle x \rangle^2, \sigma_{xy} = \langle xy \rangle - \langle x \rangle \langle y \rangle \quad (5)$$

351 The impact parameter is one way to quantize the centrality of a heavy-ion
 352 collision but it is impossible to measure in a collision. It can be estimated from
 353 observed data using theoretical models, but this is always model-dependent and
 354 to compare results from different experiments one needs an universal definition for
 355 centrality.

356 Instead in practice centrality is defined by dividing collision events into per-
 357 centile bins by the number participants or experimentally by the observed mul-
 358 tiplicity. Centrality bin 0-5% corresponds to the most central collisions with the
 359 highest multiplicity and higher centrality percentages correspond to more periph-
 360 eral collisions with lower multiplicities. A multiplicity distribution from ALICE
 361 measurements [78] illustrating the centrality division is shown in Fig. 4. The dis-
 362 tribution is fitted using a phenomenological approach based on a Glauber Monte
 363 Carlo [79] plus a convolution of a model for the particle production and a negative
 364 binomial distribution.

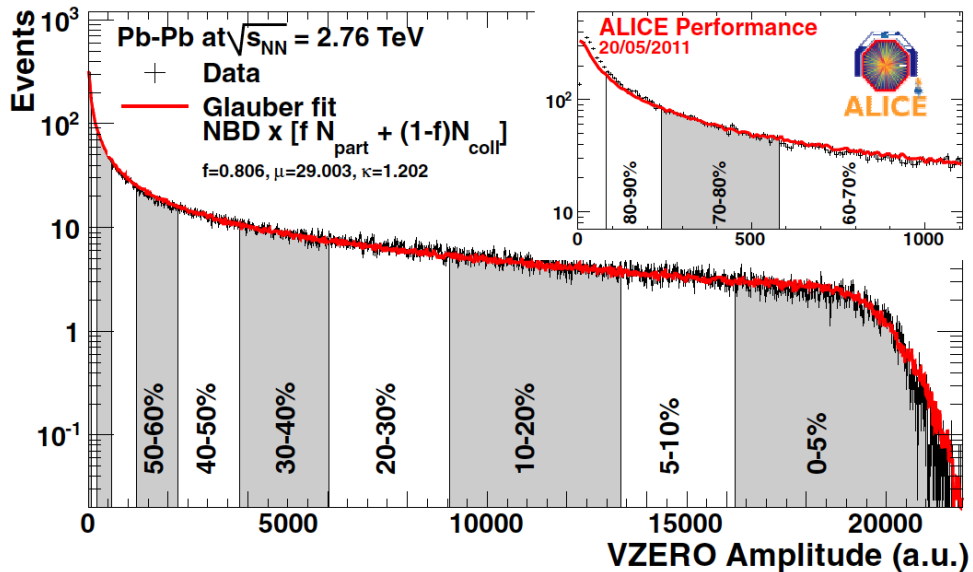


Figure 4: An illustration of the multiplicity distribution in ALICE measurements. The red line shows the fit of the Glauber calculation to the measurement. The data is divided into centrality bins [78]. The size of the bins corresponds to the indicated percentile.

365 The Glauber Model is often used to model the nuclear geometry in a heavy-

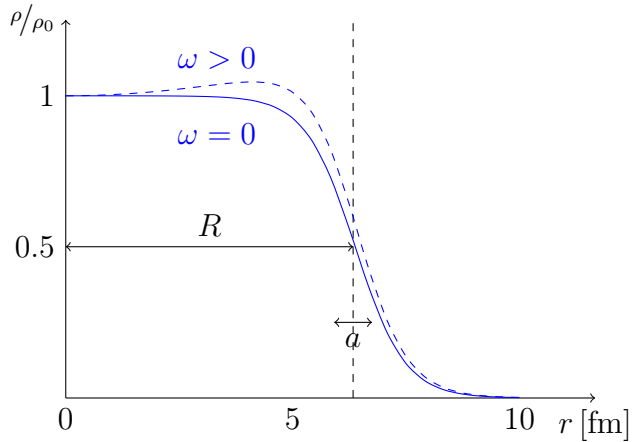


Figure 5: Woods-saxon distribution, with typical values for a Pb nucleus, $a = 0.55\text{fm}$ and $R = 6.68\text{fm}$.

³⁶⁶ ion collision. The model was originally introduced already in 1958 [80] and the
³⁶⁷ modern terminology and tools were introduced in 1976 [81] by Białas, Bleszyński,
³⁶⁸ and Czyż to model inelastic nuclear collisions.

³⁶⁹ The model starts by defining the thickness function which is the integral of the
³⁷⁰ nuclear density over a line going through the nucleus with minimum distance s
³⁷¹ from its center

$$T_A(s) = \int_{-\infty}^{\infty} dz \rho(\sqrt{s^2 + z^2}), \quad (6)$$

³⁷² where $\rho(\sqrt{s^2 + z^2})$ is the number density of nuclear matter. This can be exper-
³⁷³ imentally determined by studying the nuclear charge distribution in low-energy
³⁷⁴ electron scattering experiments [79]. For a spherically symmetric nucleus a good
³⁷⁵ approximation is given by the Woods-Saxon potential []

$$\rho(r) = \frac{\rho_0(1 + \omega r^2/R^2)}{1 + \exp(\frac{r-R}{a})}, \quad (7)$$

³⁷⁶ where ρ_0 is the nucleon density in center of the nucleus, R is the nuclear radius,
³⁷⁷ a parametrizes the depth of the skin and ω can be used to introduce a surface
³⁷⁸ excess. Figure 5 shows how this distribution looks like. With $\omega = 0$ the density
³⁷⁹ stays relatively constant as a function of r until around R where it drops to almost
³⁸⁰ 0 within a distance given by a .

³⁸¹ Overlap function is an integral of the thickness functions of two colliding nuclei
³⁸² over the overlap area. This can be seen as the material that takes part in the
³⁸³ collision. It is given as a function of the impact parameter b

$$T_{AB}(\vec{b}) = \int d^2s T_A(\vec{s}) T_B(\vec{s} - \vec{b}) \quad (8)$$

³⁸⁴ The average overlap function, $\langle T_{AA} \rangle$, in an A-A collisions is given by [82]

$$\langle T_{AA} \rangle = \frac{\int T_{AA}(b) db}{\int (1 - e^{-\sigma_{pp}^{inel} T_{AA}(b)}) db}. \quad (9)$$

³⁸⁵ Using $\langle T_{AA} \rangle$ one can calculate the mean number of binary collisions

$$\langle N_{coll} \rangle = \sigma_{pp}^{inel} \langle T_{AA} \rangle, \quad (10)$$

³⁸⁶ where the total inelastic cross-section, σ_{pp}^{inel} , gives the probability of two nucleons
³⁸⁷ interacting. As each binary collision has equal probability for direct production
³⁸⁸ of high-momentum partons, the number of binary collisions is related to the hard
³⁸⁹ processes in a heavy-ion collision. Thus the number of high momentum particles
³⁹⁰ is proportional to $\langle N_{coll} \rangle$ [83–85]. This required knowledge of σ_{inel}^{NN} , which can be
³⁹¹ measured in proton-proton collisions at different energies. At the LHC the most
³⁹² precise cross section measurements come from TOTEM [?].

³⁹³ Soft production on the other hand is related to the number of participants [84].
³⁹⁴ It is assumed that in the binary interactions participants get excited and further
³⁹⁵ interactions are not affected by previous interactions because the time scales are
³⁹⁶ too short for any reaction to happen in the nucleons. After the interactions excited
³⁹⁷ nucleons are transformed into soft particle production. The average number of
³⁹⁸ participants, $\langle N_{part} \rangle$ can be calculated from the Glauber model

$$\begin{aligned} \langle N_{part}^{AB}(\vec{b}) \rangle &= \int d^2s T_A(\vec{s}) \left[1 - \left[1 - \sigma_{NN} \frac{T_B(\vec{s} - \vec{b})}{B} \right]^B \right] \\ &+ \int d^2s T_B(\vec{s}) \left[1 - \left[1 - \sigma_{NN} \frac{T_A(\vec{s} - \vec{b})}{A} \right]^A \right]. \end{aligned} \quad (11)$$

³⁹⁹ There are two often used approaches to Glauber calculations. The optical ap-
⁴⁰⁰ proximation is one way to get simple analytical expressions for the nucleus-nucleus
⁴⁰¹ interaction cross-section, the number of interacting nucleons and the number of
⁴⁰² nucleon-nucleon collisions. In the optical Glauber it is assumed that during the
⁴⁰³ crossing of the nuclei the nucleons move independently and they will be essentially
⁴⁰⁴ undeflected.

⁴⁰⁵ With increased appreciation of the physics emerging from fluctuations in the
⁴⁰⁶ collision geometry the Glauber Monte Carlo (GMC) approach has emerged as a

method to get a more realistic description of the collisions. In GMC the nucleons are distributed randomly in a three-dimensional coordinate system according to the nuclear density distributions [83]. A heavy-ion collision is then treated as a series of independent nucleon-nucleon collisions, where in the simplest model nucleons interact if their distance in the plane orthogonal to the beam axis, d , satisfies

$$d < \sqrt{\sigma_{\text{inel}}^{\text{NN}}} \quad (12)$$

The average number of participants and binary collisions can then be determined by simulating many nucleus-nucleus collisions. The results of one GMC Pb-Pb event with impact parameter $b = 9.8 \text{ fm}$ is shown in Fig. 6

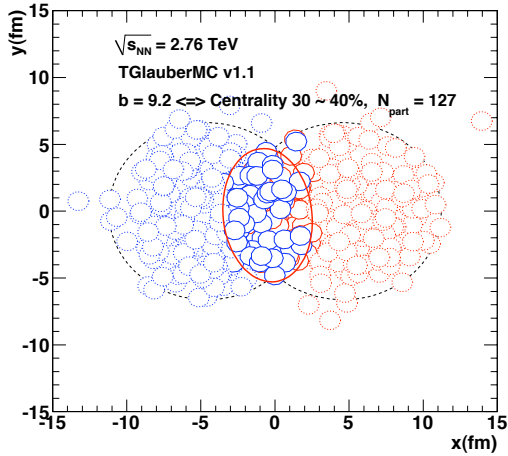


Figure 6: The results of one Glauber Monte Carlo simulation. Big circles with black dotted boundaries represent the two colliding nuclei. The participant zone is highlighted with the solid red line. Small red and blue circles represent nucleons. Circles with thick boundaries are participants i.e. they interact with at least one nucleon from the other nucleus. Small circles with dotted boundaries are spectators which do not take part in the collision. []

1.3.2 Collective motion

Quite often the evolution of a heavy-ion event can be divided into four stages. A schematic representation of the evolution of the collisions is shown in Fig. 7. Stage 1 follows immediately the collision. This is known as the pre-equilibrium stage. The length of this stage is not known but it is assumed to last about $1 \text{ fm}/c$ in proper time τ .

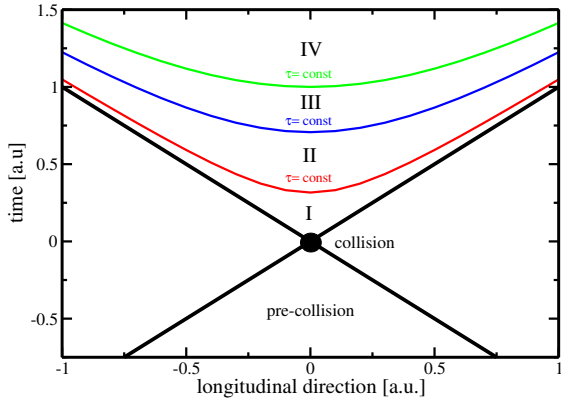


Figure 7: Schematic representation [86] of a heavy-ion collision as the function of time and longitudinal coordinates z . The various stages of the evolution correspond to proper time $\tau = \sqrt{t^2 - z^2}$ which is shown as hyperbolic curves separating the different stages.

422 The second stage is the regime where thermal equilibrium or at least near-
 423 equilibrium is reached. This lasts about $5 - 10$ fm/ c until the temperature of the
 424 system sinks low enough for hadronization to occur [?] and the system loses its
 425 deconfined, strongly coupled state. The third stage is the hadron gas stage where
 426 the hadrons still interact with each other. This ends when hadron scattering
 427 becomes rare and they no longer interact. In the final stage hadrons are free
 428 streaming and they fly in straight lines until they reach the detector.

429 In a heavy-ion collision the bulk collective particle production that is emitted
 430 from the QGP medium is referred to as flow. After the formation of the QGP, the
 431 matter begins to expand as it is driven outwards by the strong pressure difference
 432 between the center of the collision zone and the vacuum outside the collision vol-
 433 ume. The pressure-driven expansion is transformed into flow of low-momentum
 434 particles in the hadronization phase. Since the expansion is mainly isotropic the
 435 resulting particle flow is isotropic with small anisotropic corrections that are of the
 436 order of 10% at most. The isotropic part of flow is referred to as radial flow.

437 The transverse momentum spectra dN/dp_T in heavy-ion collisions is shown
 438 in Fig. 8. The vast majority of produced particles have small p_T . The difference
 439 between the yield of 1 GeV/ c and 4 GeV/ c particles is already 2-3 orders of mag-
 440 nitude. Any observables that are integrated over p_T are therefore dominated by
 441 the small momentum particles.

442 The geometry of the heavy-ion collision produces an anisotropic component to
 443 the collective motion. In a non-central heavy-ion collision, with a large impact
 444 parameter, the shape of the impact zone is almond-like. In a central collision
 445 the overlap region is almost symmetric in the transverse plane. In this case the

446 impact parameter is small. Collisions with different impact parameters are shown
 447 in Fig. 9.

448 The pressure gradient is largest in-plane, in the direction of the impact pa-
 449 rameter b , where the distance from high pressure, at the collision center, to low
 450 pressure, outside the overlap zone, is smallest. This leads to stronger collective
 451 flow along the direction of b , which in turn results in enhanced thermal emission
 452 through a larger effective temperature into this direction, as compared to out-of-
 453 plane [88–90]. The resulting flow is illustrated in Fig. 9.

454 Flow is typically quantified in the form of a Fourier composition

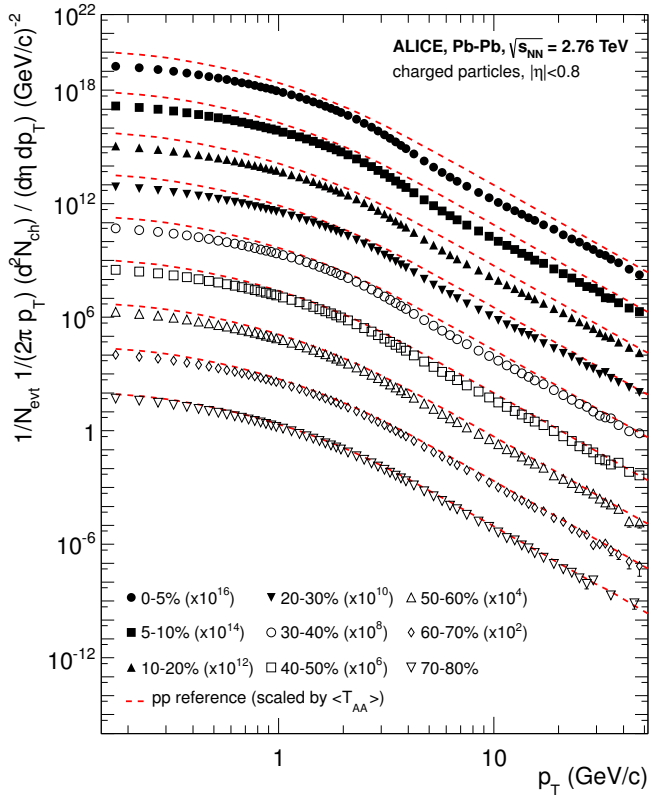


Figure 8: Charged particle spectra measured by ALICE [87] for the 9 centrality classes given in the legend. The distributions are offset by arbitrary factors given in the legend for clarity. The distributions are offset by arbitrary factors given in the legend for clarity. The dashed lines show the proton-proton reference spectra scaled by the nuclear overlap function determined for each centrality class and by the Pb-Pb spectra scaling factors [87].

$$E \frac{d^3N}{dp^3} = \frac{1}{2\pi p_T} \frac{d^2N}{dp_T d\eta} \left(1 + \sum_{n=1}^{\infty} 2v_n(p_T, \eta) \cos(n(\phi - \Psi_n)) \right), \quad (13)$$

where the coefficients v_n give the relative strengths of different anisotropic flow components and the overall normalisation gives the strength of radial flow. Elliptic flow, i.e. flow with two maxima, is represented by v_2 and v_3 represents triangular flow. The first coefficient, v_1 , is connected to directed flow [?]. This will however in total be zero because of momentum conservation. It can be nonzero in some rapidity or momentum regions but it must be canceled by other regions.

In a peripheral collision v_2 is the dominant part of anisotropic flow as it arises from the asymmetric geometry of the collision region. Higher harmonics, the most notable of which is the triangular flow, come from fluctuations in the initial conditions []. As the colliding nuclei are not static objects, the arrangement of the nucleons at the time of the collision is random. The shape of the collision zone is not a perfect almond. Instead it can have a more complex shape. Also inside the collision zone the density of the created medium is not homogenous but it can have denser hot spots

It has been noted that higher harmonics of v_n would be suppressed by viscous

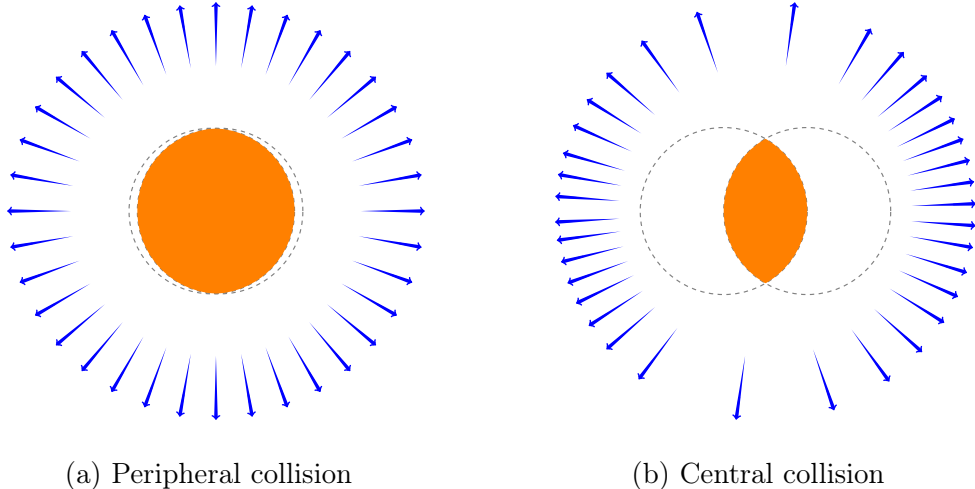


Figure 9: Illustration of flow in momentum space in central and peripheral collisions. The density of the arrows represent the magnitude of flow seen at a large distance from the collision in the corresponding azimuthal direction. In a peripheral collision momentum flow into in-plane direction is strong and flow into out-of-plane direction is weak. In a central collision anisotropy in flow is smaller, but the total yield of particles is larger.

470 effects and that the shape of v_n as a function of n would provide another valuable
471 tool for studying η/s [91]. For a long time it was believed that the odd harmonics
472 would be negligible. In 2007 Mishra *et al.* [92] argued that density inhomogeneities
473 in the initial state would lead to non-zero v_n values for higher harmonics including
474 v_3 .

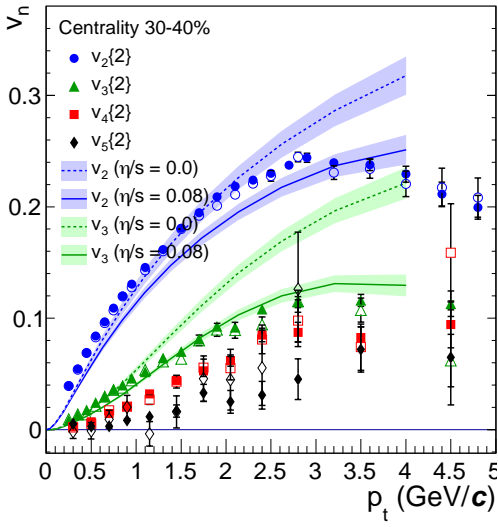
475 The first one to predict anisotropic flow in heavy-ion collisions was Ollitrault
476 in 1992 [88]. However, the first papers on anisotropy did not discuss the Fourier
477 composition. Instead they approached the problem with a classic event shape
478 analysis. (sphericity) The first experimental studies of anisotropy were performed
479 at the AGS [93] in 1993, where it was noted that the anisotropy of particle pro-
480 duction in one rapidity region correlates with the reaction plane angle defined in
481 another rapidity region. The first ones to present the Fourier decomposition were
482 Voloshin and Zhang in 1996 [94]

483 Measurements of different flow harmonics are shown in Fig. 10. The left panel
484 shows different flow harmonics as a function of p_T as measured by ALICE [95] in
485 peripheral collisions. In general flow coefficients decrease as a function of n after
486 $n = 2$. Central collisions are an exception. The right panel of Fig. 10 shows v_n as
487 a function of n in central collisions as measured by ALICE [96]. The results are
488 compared to hydrodynamic predictions [97].

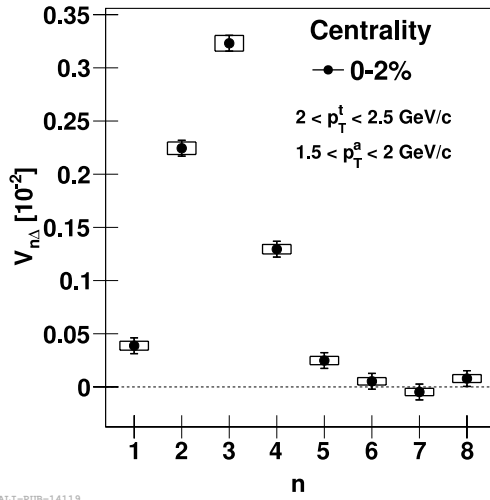
489 The measured collective flow in heavy-ion collisions has been successfully mod-
490 elled with the relativistic version of hydrodynamics. The power of relativistic
491 hydrodynamics lies in its simplicity and generality. Hydrodynamics only requires
492 that there is local thermal equilibrium in the system. In order to reach thermal
493 equilibrium the system must be strongly coupled so that the mean free path is
494 shorter than the length scales of interest [86], which is assumed to hold for QGP
495 phase of a heavy-ion collision [].

496 The use of relativistic hydrodynamics in high-energy physics dates back to
497 Landau [98] and the 1950's, before QCD was discovered. Back then it was used
498 in proton-proton collisions. Development of hydrodynamics for the use of heavy-
499 ion physics has been active since the 1980's, including Bjorken's study of boost-
500 invariant longitudinal expansion and infinite transverse flow [99]. Major steps
501 were taken later with the inclusion of finite size and and dynamically generated
502 transverse size [100, 101], a part of which was done at the University of Jyväskylä.

503 **What has been learned**



(a) ALICE measurement of v_2, v_3, v_4, v_5 as a function of transverse momentum. The flow coefficients are determined by two-particle correlations using different rapidity separations. The full and open symbols are for $\Delta\eta > 0.2$ and $\Delta\eta > 1.0$. The results are compared to hydrodynamic predictions [97] with different values of η/s [95].



(b) Amplitude of v_n harmonics as a function of n for the 2% most central collisions as measured by ALICE [96].

Figure 10: Flow measurements of higher harmonics

504 **1.4 Hard processes**

505 **1.4.1 pQCD factorization**

506 The term Hard Scattering is used in connection with the scattering of two point-
507 like constituents (partons) of colliding nucleons, when the momentum transfer Q^2
508 is large ($Q \gg \Lambda_{\text{QCD}}$). Figure 11 shows the incoming partons, quarks or gluons, as
509 they exchange a space-like virtual gluon and produce two highly virtual outgoing
510 partons. The outgoing partons will eventually fragment into collimated showers of
511 partons, referred to as jets.

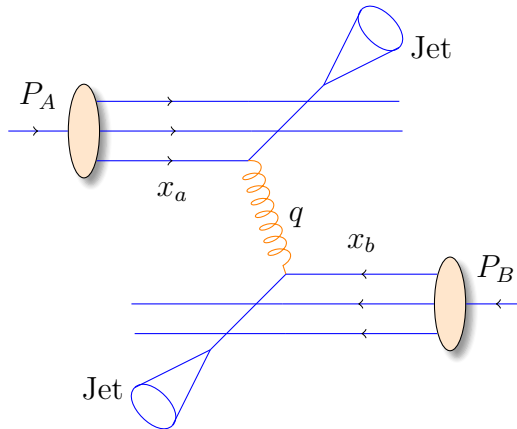


Figure 11: Schematic view of hard scattering process between 2 protons, producing 2 jets

512 Historically one would study hard scatterings foremost with inclusive hadron
513 spectra. In this context hadron production from hard scatterings can be factorised
514 into three components; the parton distribution functions f_a , f_b that give the prob-
515 ability of getting a parton with momentum fraction x of the proton, the cross
516 section of the elementary scattering $ab \rightarrow cd$, (A summary of the $2 \rightarrow 2$ pro-
517 cesses in QCD is shown in Fig. 12) and the fragmentation functions that give the
518 probability of getting hadron h from the parton.

$$\frac{d\sigma_{pp}^h}{dy d^2p_T} = K \Sigma_{abcd} \int dx_a dx_b f_a(x_a, Q^2) f_b(x_b, Q^2) \frac{d\sigma}{dt} (ab \rightarrow cd) \frac{D_{h/c}^0}{\pi z_c}, \quad (14)$$

519 where

$$x_{a,b} = \frac{|p_{a,b}|}{|p_{\text{proton}}|}. \quad (15)$$

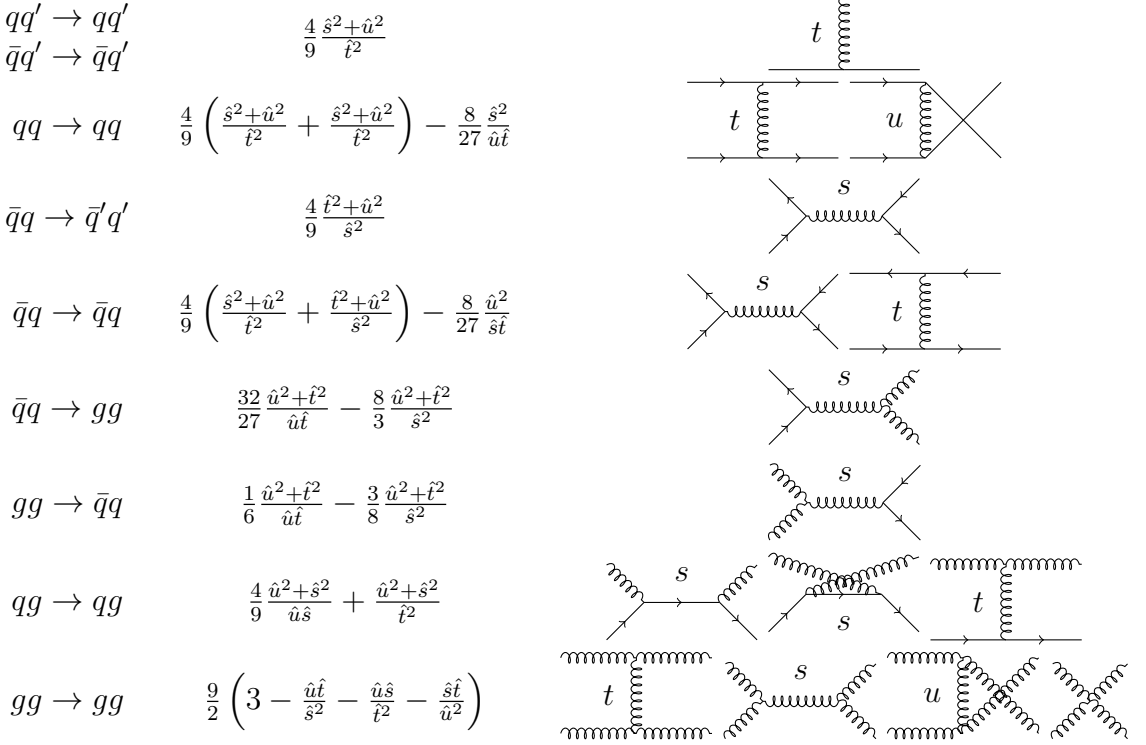


Figure 12: The basic pQCD processes and their quadratic matrix elements

520 Parton Distribution Function

521 Parton Distribution Functions (PDFs) $f_a(x)$ give the differential probability for
 522 parton a to carry momentum fraction x of the proton momentum. As the PDFs
 523 cannot be calculated from first principles they are measured in Deeply Inelastic
 524 Scattering (DIS) experiments [?] and are extrapolated to the relevant momen-
 525 tum scales using the Dokshitzer-Gribov-Lipatov-Altarelli-Parisi (DGLAP) evolu-
 526 tion scheme [102–104]

$$\mu_F^2 \frac{\partial f_i(x, \mu_F^2)}{\partial \mu_F^2} = \sum_j \frac{\alpha_s(\mu_F)}{2pi} \int_x^1 \frac{dz}{z} P_{ij}(z) f_j \left(\frac{x}{z}, \mu_F^2 \right), \quad (16)$$

527 where μ_F is a factorization scale. The splitting functions P_{ij} describe a probability
 528 to radiate parton i from parton j as a function of the momentum fraction z carried
 529 away by the offspring parton. Different theory interpretation and experimental
 530 data gives rise to different PDF's. Thus there are several commonly used PDF
 531 sets: CTEQ [?], HERAPDF [?], PDF4LHC [?], etc.

532 Fragmentation functions

533 improve The final component in the factorization, fragmentation functions, de-
 534 scribe the distribution of the fractional momenta of fragments radiated from the
 535 outgoing parton. Fragmentation function $D(z)$ gives the average multiplicity m
 536 of jet fragments having $z > z_0$ [?] as

$$m(z_0) = \int_{z_0}^1 D(z) dz \Rightarrow m(0) \equiv \langle m \rangle = \int_0^1 D(z) dz, \quad (17)$$

537 where z is the longitudinal momentum fraction of jet momentum p_{jet} carried away
 538 by the jet fragment p_{part}

$$z = \frac{\vec{p}_{\text{part}} \cdot \vec{p}_{\text{jet}}}{p_{\text{jet}}^2} = \frac{p_{\text{part}}}{p_{\text{jet}}} \Big|_{\vec{p}_{\text{part}} \parallel \vec{p}_{\text{jet}}} \quad (18)$$

539 Because of momentum conservation the sum of all jet fragments must be equal
 540 to the jet momentum, i.e.

$$\sum p_{i,\text{part}} = p_{\text{jet}} \Rightarrow \sum z_i = 1 \Rightarrow \int_0^1 z D(z) dz = 1 \quad (19)$$

541 1.4.2 Jet showering

542 More detailed studies of the hard processes require a formulation of the showering
 543 process. The full picture is a complicated $2 \rightarrow n$ scattering, but it is typically seen
 544 as a series of $1 \rightarrow 2$ splittings with decreasing virtuality following the initial $2 \rightarrow 2$
 545 scattering [105].

546 To first order the cascade is governed by the DGLAP evolution equation [102–
 547 104]

$$dP_a(z, Q^2) = \frac{dQ^2}{Q^2} \frac{\alpha_s}{2\pi} P_{a \rightarrow bc}(z) dz, \quad (20)$$

which gives the differential probability that parton a (mother) will branch to two
 partons b and c (daughters), at a virtuality scale Q^2 . Daughter b takes a fraction
 z of the parton a energy and daughter c takes energy fraction $1 - z$. The splittings
 kernels $P_{a \rightarrow bc}(z)$ are

$$P_{q \rightarrow qg}(z) = \frac{4}{3} \frac{1+z^2}{1-z} \quad (21)$$

$$P_{g \rightarrow gg}(z) = 3 \frac{(1-z)(1-z)^2}{z(1-z)} \quad (22)$$

$$P_{g \rightarrow q\bar{q}}(z) = \frac{n_f}{2} (z^2 + (1-z)^2), \quad (23)$$

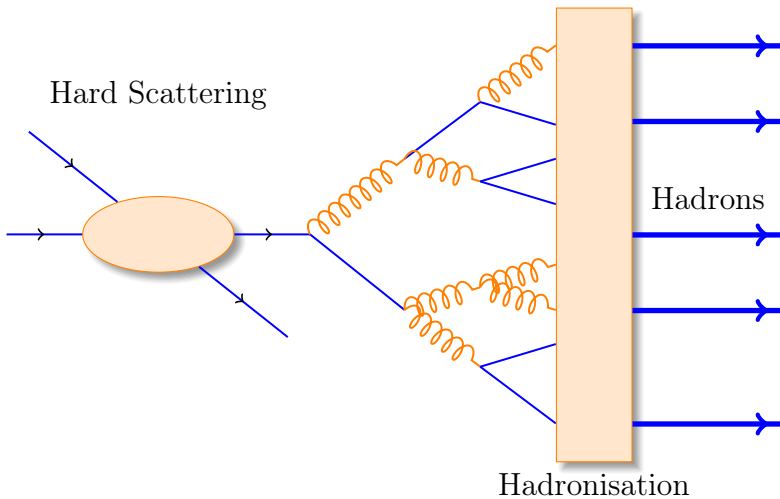


Figure 13: An illustration of jet showering. The highly virtual parton from the hard scattering will produce a shower of softer partons. When the virtuality is low enough the shower will go through a hadronisation process that produces the hadrons, which will be eventually observed in the detector.

548 where n_f is the kinematically allowed number of quark flavours. There is some
 549 freedom in how the evolution variable Q^2 is chosen. If $Q^2 = f(z)m^2$ and $f(z)$ is
 550 a positive and a smooth function it holds that

$$\frac{dQ^2}{Q^2} dz = \frac{dm^2}{m^2} dz. \quad (24)$$

551 Of the Monte Carlo generators used in this thesis PYTHIA uses m^2 as the
 552 evolution variable [?], while HERWIG uses an energy-weighted emission angle
 553 $E^2(1 - \cos\theta) \approx m^2/z(1-z)$ [?].

554 Formally eq 20 corresponds to the emission of an infinite number of partons.
 555 However very soft and collinear gluons need not be considered and one can introduce
 556 an effective cut-off scale Q_0 , usually taken to be of the order of 1 GeV.

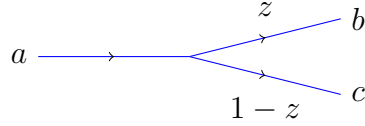
557 Going further one approach is to introduce time ordering, i.e. to decide which
 558 of the emissions occurs first. This is done in the form of a Sudakov form factor [?]

$$P_a^{no}(Q_{\max}^2, Q^2) = \exp \left(- \int_{Q^2}^{Q_{\max}^2} \int_{z_{\min}}^{z_{\max}} dP_a(z', Q'^2) \right), \quad (25)$$

559 which gives the probability that no emissions occur between the initial maximum
 560 scale Q_{\max}^2 and a given Q^2 and within limits $z_{\min} < z < z_{\max}$. Thus the probability
 561 for the first branching to occur at $Q^2 = Q_a^2$ is given by

$$d\Delta_a(z, Q_a^2, Q_{\max}^2) = dP_a(z, Q_a^2) P_a^{no}(Q_{\max}^2, Q_a^2). \quad (26)$$

562 Partons b and c that were produced will further branch with maximum virtuality scale Q_{\max}^2 given by Q_a^2 . Similarly their daughters will continue branching
563 until the cutoff scale is reached, thus producing a shower.
564



565 1.4.3 Soft gluon radiation and angular ordering

566 Let us now consider a case where a gluon splits into two quarks, and one of the
567 created quarks emits a soft gluon as seen in Fig. 14. In the laboratory frame the
568 time it takes for a gluon to be emitted from a quark can be estimated to be

$$t_{\text{emit}} \approx \frac{1}{E_q}, \quad (27)$$

569 where the energy of the quark is given by E_q . In the rest frame of the quark
570 its energy is given by its virtuality M_{virt} and assuming the quark is massless the
571 Lorentz factor between the rest frame and the laboratory frame is

$$\gamma = \frac{E_q}{M_{\text{virt}}}. \quad (28)$$

572 Thus the emission time can be written as

$$t_{\text{emit}} \approx \frac{E_q}{M_{\text{virt}}^2} = \frac{E_q}{(k + p)^2}, \quad (29)$$

573 where k and p are the four-momenta of the gluon and the quark after the gluon
574 emission. This can be written open in the laboratory frame. Through assuming
575 that the end products are massless and Taylor-expanding the resulting cosine term
576 gives a form that expresses the emission time using the opening angle θ_{kq} between
577 the quark and the gluon

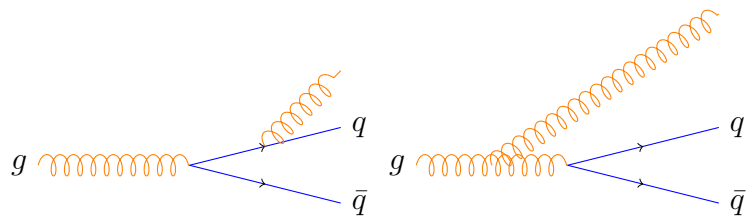


Figure 14: Soft gluon production

$$t_{\text{emit}} \approx \frac{1}{k\theta_{\text{kq}}^2}. \quad (30)$$

578 The transverse wavelength of the emitted gluon is $\lambda_{\perp}^{-1} = k_{\perp} \approx k\theta_{\text{kq}}$. Thus we get

$$t_{\text{emit}} \approx \frac{\lambda_{\perp}}{\theta_{\text{kq}}}. \quad (31)$$

579 The secondary gluon can only probe the quark of the earlier splitting if the trans-
580 verse wavelength is smaller than the transverse separation of the produced $q\bar{q}$ pair.

581 The transverse separation is given by

$$r_{\perp}^{q\bar{q}} \approx \theta_{q\bar{q}} t_{\text{emit}} \approx \lambda_{\perp} \frac{\theta_{q\bar{q}}}{\theta_{\text{kq}}}. \quad (32)$$

582 Thus in order for the emission to probe the individual quark, the opening angle
583 of the $q\bar{q}$ splitting, $\theta_{q\bar{q}}$, must be larger than θ_{kq} . If the opening angle θ_{kq} is larger,
584 the gluon can't distinguish between the quark and the antiquark, so it probes the
585 state of the system before the splitting, i.e. it can be treated like it was emitted
586 from the primary gluon.

587 This leads to the angular ordering of soft gluon radiation. Each successive
588 angle must be smaller than the previous one. The effect can be calculated in all
589 orders [?] and in the DGLAP formalism one can select the evolution variable Q^2
590 in a way that ensures angular ordering [?].

591 (The soft gluon behaves as if testing the colour charge of the jet as a whole)=
592 As a results to describe the jet evolution in terms of independent sequential parton
593 splittings one has to include the Angular ordering (AO) condition. This is imple-
594 mented differently in Monte Carlo generators. In PYTHIA8 this is strictly not
595 included, but the transverse momentum ordered showers are as accurate in de-
596 scribing the soft gluon emissions as the angular ordered showers [106]. In Herwig
597 angular ordering is a consequence of the choice of the evolution variable.

598 1.4.4 Jet hadronisation

599 When the virtuality of the shower is low enough, the shower starts to hadronise. In
600 this regime the parton shower reaches a scale close to Λ_{QCD} and the perturbative
601 description is no longer valid. Thus the hadronisation stage must be described in a
602 non-perturbative manner. In general hadronisation is assumed to be universal, i.e.
603 it shouldn't depend on the collision energy or system. The most simple scenario
604 that is used in several theory calculations is the so-called local parton-hadron
605 duality [107]. In the local parton-hadron duality hypothesis it is assumed that
606 there exists a low virtuality scale Q_0 in which the hadronisation happens, that is
607 independent of the scale of the primary hard process. At this scale the partons

608 are transformed into hadrons, assuming that the flow of momentum and quantum
 609 numbers for the hadrons can be directly obtained from those of partons introducing
 610 only small normalising constants.

611 The next sections will present more complicated hadronisation models used in
 612 Monte Carlo generators, PYTHIAand Herwig.

613 Lund string model

614 One common implementation in MC generators is the Lund string fragmentation
 615 algorithm [108]. The string model is based on the fact that in QCD linear confine-
 616 ment is expected over large distances [106]. This can be modelled by imagining
 617 a colour flux tube being stretched between the outgoing partons. The left side of
 618 Fig. 15 illustrates this point for a $q\bar{q}$ -pair. The tube is assumed to have a uni-
 619 form fixed transverse size of about 1 fm along its length, which leads to a linearly
 620 rising potential $V(r) = \kappa r$, where the string constant κ describes the amount of
 621 energy per unit length. A value of $\kappa \approx 1 \text{ GeV/fm} \approx 0.2 \text{ GeV}^2$ can be obtained
 622 from hadron mass spectroscopy [?].

623 The evolution of string fragmentation is illustrated schematically on the right
 624 side of Fig. 15. This figure is drawn in a light cone presentation, so the initial
 625 quark and antiquark are going to separate directions at the speed of light, which
 626 assumes them as massless. The string between them, illustrated in the figure by
 627 the red line, stretches until its potential energy becomes high enough that it can
 628 break, forming a new quark-antiquark pair. If the original pair was $q\bar{q}$ and the
 629 new pair $q'\bar{q}'$, now two new pairs $q\bar{q}'$ and $q'\bar{q}$ have formed. As these particles
 630 are also moving away from each other, the strings between them can stretch and
 631 break, creating yet more pairs. The process continues until the invariant mass of
 632 the system connected by the string becomes small enough and a final state meson
 633 is formed.

634 To mathematically model the string one can use a massless relativistic string
 635 with no transverse degrees of freedom. The gluons are represented as energy and
 636 momentum carrying kinks on the string with incoherent sums of one colour charge
 637 and one anticolour charge. When this string breaks, it is classically required that
 638 the created quark and antiquark are produced at a certain distance if they are to
 639 have any mass or transverse momentum. However, taking into account quantum
 640 mechanics, the pair must be created at one point and then tunnel out to the
 641 classically allowed region. Thus the probability to create a new quark-antiquark
 642 pair becomes proportional to the tunnelling probability [108].

$$P_{\text{tunnelling}} \propto \exp\left(\frac{-\pi m_\perp^2}{\kappa}\right) = \exp\left(\frac{-\pi m^2}{\kappa}\right) \left(\frac{-\pi p_\perp^2}{\kappa}\right), \quad (33)$$

643 where the transverse mass m_\perp is defined as $m_\perp^2 = m^2 + p_\perp^2$. The transverse

644 momentum is now defined to be transverse to the string axis. This formula gives
645 flavour-independent Gaussian p_\perp -distribution for the created $q\bar{q}$ pairs.

646 As explained above the string fragmentation would only produce mesons in
647 the final state, but we know that also baryons are created in the process. In the
648 string fragmentation model baryon production is included by adding a probability
649 that a diquark-antidiquark pair is created instead of a quark-antiquark pair when
650 a string breaks.

651 The kinematics of each string breaking are determined iteratively. Since there
652 is no natural ordering, the string breaking can be considered in any order and
653 the answer obtained must be the same. One can start from the q leg and work
654 one's way to the \bar{q} leg, or vice versa. This give a left-right symmetry of the
655 string fragmentation. In the Lund model this is taken into account by defining a
656 symmetric fragmentation function

$$f(z) \propto \frac{1}{z} (1-z)^a \exp\left(-\frac{bm_\perp^2}{z}\right) \quad (34)$$

657 to break the string into a hadron and a remainder system. Here z is the fraction
658 of light-cone momentum p^+ given to the hadron in the string breaking, m_\perp is the
659 transverse mass of the hadron and a and b are tunable parameters of the model.
660 For heavy quarks this has to be modified as

$$f(z) \propto \frac{1}{z^{1+bm_Q^2}} (1-z)^a \exp\left(-\frac{bm_\perp^2}{z}\right) \quad (35)$$

661 The process can be thought as follows: first start from the q -leg of a $q\bar{q}$ system
662 and choose to consider the breaking to new $q'\bar{q}'$ pair closest to this leg. Now the
663 breaking will produce a hadron $q\bar{q}'$ and a remainder system spanning from $q'\bar{q}$.
664 Then the process is continued until the \bar{q} -leg is reached. A small detail here is
665 that in equation (34) it is assumed that the mass of the remainder system is large.
666 Thus some patching up is needed for the last two hadrons coming from a string.
667 The patching up is done such that the place where it happens looks as closely like
668 any other string break as possible.

669 One additional possibility one must consider is that a string can have such a
670 low mass that it cannot break at all. In this case a single hadron is generated out
671 of the string and if necessary energy and momentum are exchanged with other
672 partons in the event.

673 After all the hadrons are produced, the short-lived ones can still decay before
674 the set of final state particles in the simulation is obtained [?]

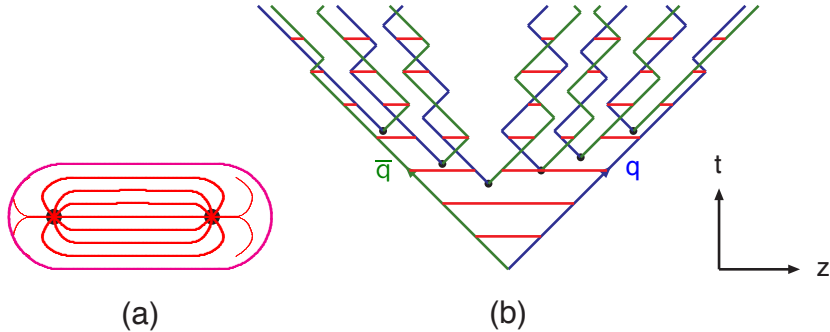


Figure 15: (a) A flux tube spanned between a quark and an antiquark. (b) The motion and breakup of a string system, with the two transverse degrees of freedom suppressed (diagonal lines are (anti)quarks, horizontal ones snapshots of the string field) [106].

675 Cluster model

676 Instead of a string model HERWIG [109] uses a cluster model for hadronisation.
 677 The advantage of cluster models is that they require a smaller number of param-
 678 eters than string models. The model is based on the preconfinement property of
 679 parton showers, i.e. the colour structure of the shower at any evolution scale Q_0 is
 680 such that colour singlet combinations of partons can be formed with an asympto-
 681 tically universal invariant mass distribution. The invariant mass does not depend
 682 on the initial hard process scale Q , but only on Q_0 and the QCD scale Λ_{QCD} , when
 683 $Q \gg Q_0$.

684 The cluster model starts from transforming all gluons non-perturbatively into
 685 $q\bar{q}$ pairs, which requires that the gluons get a mass, which must be at least twice
 686 the lightest quark mass. After the gluons are transformed into quarks, the adjacent
 687 colour lines can be clustered together to colour singlet states with mesonic quantum
 688 numbers. The momentum of these clusters is defined to be the sum of the momenta
 689 of the clustering partons. According to preconfinement, the mass distribution of
 690 these clusters is independent of the details of the hard scattering. Additionally the
 691 clusters can be regarded as highly excited hadron resonances and decayed into the
 692 final state hadrons.

693 Some of these initial clusters are too heavy to reasonably describe an excited
 694 state of a hadron. These must be split before they are allowed to decay. The
 695 cluster C is split if its mass fulfills the condition [?]

$$M_C^p \geq M_{\max}^p + (m_1 + m_2)^p, \quad (36)$$

696 where $m_{1,2}$ are the masses of the constituents partons of the cluster and M_{\max} and
 697 p are the main parameters of the model. These have to be chosen separately for

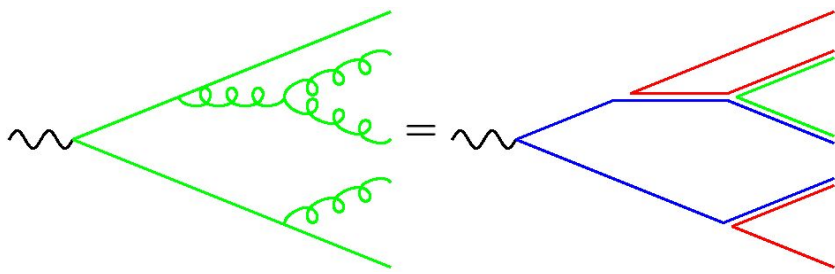


Figure 16: Colour structure of a parton shower to leading order in N_c . [106]

clusters containing light, charmed and bottom quarks. When a cluster is split, a pair of light quarks is generated from the vacuum and two new clusters are made, both containing one quark from the original cluster and one from the newly generated pair. The splitting is continued until no clusters with masses M_C fulfilling the equation 36 remains.

When the clusters are light enough, they decay into final state hadrons. If the mass of the cluster is high enough for decaying into a baryon-antibaryon pair, there is a parameter deciding whether the cluster undergoes mesonic or baryonic decay. For a mesonic decay a quark-antiquark pair is created from the vacuum and for the baryonic decay a diquark-antidiquark pair is made. Then the exact decay products are chosen and the cluster decays isotropically in the rest frame of the cluster. If there are partons produced in the perturbative phase involved in the decay, they retain their original direction in the cluster rest frame, up to some Gaussian smearing. If the cluster mass is too low to decay into a pair of mesons, it decays into the lightest possible hadron and some energy and momentum is exchanged with the adjacent clusters. At the end we are left with the final state hadrons, some of which might still decay until the end of the simulation if they are very short-lived. [?]

1.4.5 Interactions between jet and medium

Let us now look at what happens to jet production in heavy-ion collisions. High momentum particles are very rare and they are only produced in the initial collisions. In a heavy ion collision, where a QGP medium is formed, the hard scattered quarks and gluons are expected to interact strongly with the medium due to their colour charges and thus lose energy, either through collisions with medium partons, or through gluon bremsstrahlung [5]. This is referred to as jet quenching. Figure 17 shows a dijet inside QGP medium. Studying the modification of jets inside the medium gives another key approach to constraining the properties of QGP. Modification can be also observed in jet shapes, particle composition, fragmentation, splitting functions and many others.

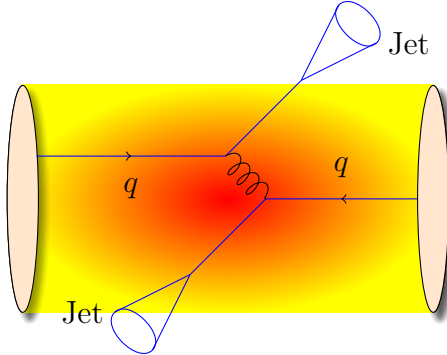


Figure 17: If hard scatterings happen in conjunction with QGP medium the produced jets must traverse the medium. Thus they are subject to interactions with the medium. Note that the dijet pair can be created anywhere within the medium volume and thus the two jets will have differing path lengths through the medium.

727 Discovery of jet quenching via leading hadron suppression

728 First evidence of jet quenching comes from observing high p_T tracks, i.e. the
729 leading hadrons of jets. In this picture jet quenching in heavy-ion collisions is
730 usually quantified with the nuclear modification factor R_{AA} , which is defined as

$$R_{AA}(p_T) = \frac{(1/N_{AA}^{evt}) dN^{AA}/dp_T}{\langle N_{coll} \rangle (1/N_{pp}^{evt}) dN^{pp}/dp_T} \quad (37)$$

731 where dN^{AA}/dp_T and dN^{pp}/dp_T are the yields in heavy-ion and proton-proton
732 collisions, respectively and $\langle N_{coll} \rangle$ is the average number of binary nucleon-nucleon
733 collisions in one heavy-ion event. The number of binary collisions can be calculated
734 from the Glauber model as shown in Sec. ???. From the point of view of direct
735 production at high p_T a heavy-ion collision can be estimated relatively well to be
736 only a series of proton-proton collisions. At low p_T this scaling breaks down as the
737 determining factor in direct production is the number of participants.

738 If the medium has no effect on high p_T particles the nuclear modification factor
739 should be 1. At RHIC and LHC this has been observed to be as low as 0.2, which is
740 a clear signal that jet quenching is happening. Measurements of R_{AA} from different
741 sources are shown in Fig. 18. One should note that the physical interpretation is
742 not that 80 % of high momentum tracks disappear, rather they are shifted to
743 smaller momenta. The relation between the shift in momentum and R_{AA} depends
744 on the steepness of the dN/dp_T spectra. At LHC energies the spectrum is flatter
745 and thus the same R_{AA} value as in RHIC requires a larger momentum shift, which
746 results from the larger temperature of the medium.

747 The reaction plane dependence of inclusive particle R_{AA} demonstrates that en-

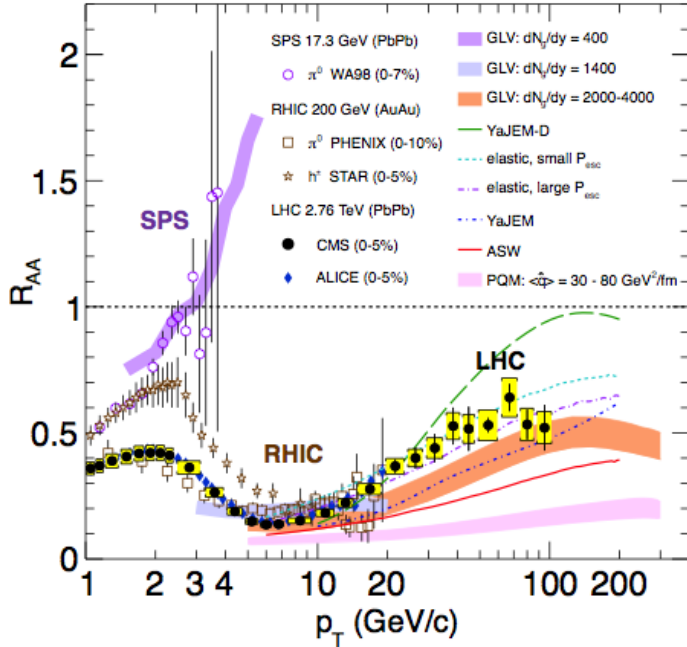


Figure 18: Measurements of the nuclear modification factor R_{AA} in central heavy-ion collisions at three different center-of-mass energies, as a function of p_T , for neutral pions (π^0), charged hadrons (h^\pm), and charged particles [110–114], compared to several theoretical predictions [66, 115–119]. The error bars on the points are the statistical uncertainties, and the yellow boxes around the CMS points are the systematic uncertainties. The bands for some of the theoretical calculations represent their uncertainties [120].

ergy loss is path length dependent [121], as expected from models. The path length can be affected by collisions centrality and system size. However the temperature and lifetime of the QGP also changes with changing centrality and system size. Thus to study different path lengths the angle relative to the reaction plane gives the cleanest signal, as the properties of medium remain the same. Additionally it was concluded that there is no suppression for path lengths below $L = 2$ fm. Similar indications about path length dependence are given by jet v_2 both at RHIC [122] and at LHC [123, 124].

756 QED Bremsstrahlung

757 Many of the energy loss models exploit the analogy between the QCD interaction
 758 of parton propagating through the coloured medium and the QED energy loss of
 759 electron propagating through material. An electron propagating through matter
 760 loses its energy by photon Bremsstrahlung radiation. In the simplest case, each

761 individual scattering center results in a single emission of a photon. This is known
 762 as the Bethe-Heitler regime [125]. The energy spectrum of radiated photons dN/dE
 763 is, in this case, proportional to $1/E$. However, the Bremsstrahlung photon, can be
 764 radiated only when the distance between the scattering centers is larger than the
 765 formation length. In the limit, when the scattering centers are closer than the
 766 formation length, the Bremsstrahlung process is suppressed. This phenomenon
 767 is known as the Landau-Pomeranchuk-Migdal (LPM) [126, 127] suppression. The
 768 radiated spectrum in this regime is proportional to $1/\sqrt{E}$.

769 Lower energy photons are further suppressed by the destructive interference
 770 leading to the suppression of Bremsstrahlung photons of $E < \gamma\omega_p$, where ω_p is
 771 the plasma frequency of the radiator. This is known as Dielectric suppression.
 772 The photon energy distribution in this regime is proportional to the energy of the
 773 photon. A schematic view of the effect of these three regimes is shown in Fig. 19.

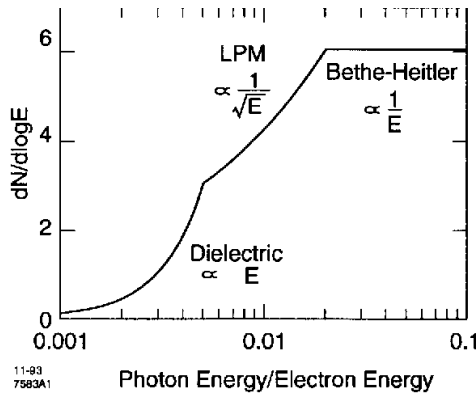


Figure 19: The expected bremsstrahlung spectrum for an electron propagating through material. [128].

774 QCD

775 In QCD the radiative energy loss mechanism is given in terms of the transport co-
 776 efficient $\langle \hat{q} \rangle$, which describes the average momentum transfer between the medium
 777 and parton [129]. The exact definition of this depends on the theoretical formalism
 778 used to describe the energy loss mechanism.

779 The simplest energy loss process is elastic QCD scattering off the medium par-
 780 tons. In elastic scatterings the recoil energy of the scattered partons are absorbed
 781 by the thermal medium, which reduces the energy of the initial parton. The mean
 782 energy loss from elastic scatterings can be estimated by

$$\langle \Delta E \rangle_{\text{el}} = \sigma \rho L \langle E \rangle_{\text{scatt}} \propto L, \quad (38)$$

783 where σ is the interaction cross section and $\langle E \rangle_{1scatt}$ is the mean energy transfer
 784 of one individual scattering [130]. This assumption holds if the mean energy is
 785 independent of the total energy of the parton (E). The transport coefficient of
 786 elastic scattering, $\langle \hat{q}_{el} \rangle = \langle \Delta E \rangle / L$, is defined as the mean energy los per unit path
 787 length.

788 Another energy loss mechanism is medium-induced radiation. In QCD this
 789 radiation is mainly due to the elementary splitting processes, $q \rightarrow qg_r$ and $g \rightarrow gg_r$.
 790 Assuming that the parton is moving with the speed of light radiation energy loss
 791 can be estimated by

$$\langle \Delta E \rangle_{rad} \propto T^3 L^2, \quad (39)$$

792 where L is the length of the medium and T is its temperature [131]. The differ-
 793 ent exponents of L in equations 38 and 39 indicate that radiative energy loss is
 794 dominant over elastic energy loss.

795 There are several models that attempt to describe the nature of the energy loss
 796 mechanism. The most used models can be divided into four formalisms.

797 In the Gyulassy-Levai-Vitev (GLV) [132] opacity expansion model the radia-
 798 tive energy loss is consiered on a few scattering centers N_{scatt} . The radiated gluon
 799 is constructed by pQCD calculation as summing up the relevant scattering am-
 800 plitudes in terms of the number of scatterings. Another approach into opacity
 801 expansion is the ASW model by Armesto, Salgado and Wiedermann [133].

802 Thermal effective theory formulation by Arnold, Moore and Yaffe (AMY) [134]
 803 uses dynamical scattering centers. It is based on leading order pQCD hard thermal
 804 loop effective field theory. This model assumes that because of the high temper-
 805 ature of the plasma the strong coupling constant can be treated as small. The
 806 parton propagating through the medium will lose energy from soft scatterings and
 807 hard scatterings.

808 The above models calculate the energy loss while the parton propagates through
 809 the medium, focusing on the pQCD part. The higher twist (HT) approach by Wang
 810 and Guo [135] implements the energy loss mechanism in the energy scale evolution
 811 of the fragmentation functions.

812 The last category is formed by the Monte Carlo methods. The PYTHIA event
 813 generator [136] is widely used in high-energy particle physics. Two Monte Carlo
 814 models based on PYTHIA describing the energy loss mechanism are PYQUEN [137]
 815 and Q-Pythia [138]. Other Monte Carlo models include JEWEL [139] and Ya-
 816 JEM [140].

817 1.4.6 New paradigm of jet Quenching

818 As described in the previous sections the first indications of jet quenching, such
 819 as R_{AA} , looked essentially at the leading hadrons of jets, the hard part, ignoring

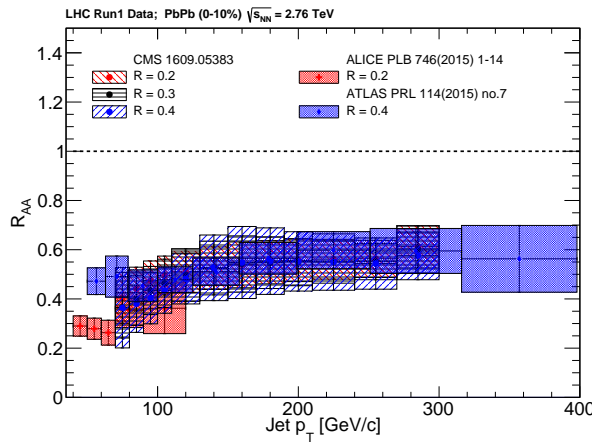


Figure 20: Reconstructed anti- k_T jet R_{AA} from ALICE [141] with $R = 0.2$ for $|\eta| < 0.5$, ATLAS [142] with $R = 0.4$ for $|\eta| < 2.1$, and CMS [143] with $R = 0.2, 0.3$ and 0.4 for $|\eta| < 2.0$. The ALICE and CMS data are consistent within uncertainties while the ATLAS data are higher. This may be due to the ATLAS technique, which could impose a survivor bias and lead to a higher jet RAA at low momenta. Figure from [5]

the soft scale part of jet phenomena. However, experimental methods have since improved; jet reconstruction algorithms have become reliable in the LHC era. Instead of the leading hadron we can study the entire jet shower and its structure.

The first evidence of jet quenching in reconstructed jets at the LHC was observed by measuring the dijet asymmetry, A_j [5]. In jet observables one must consider what happens to the lost energy. Radiated gluons may end up being clustered with the jet, depending on the radiation angle, the parameters of jet reconstruction and whether the gluon reaches equilibrium with the medium or not. Thus the suppression on the jet level is expected to be smaller. Figure 21 shows jet R_{AA} in central Pb–Pb collisions measured by ALICE,ATLAS and CMS and indeed jet R_{AA} is about 0.5 instead of 0.2. Of course this begs the question, what counts as being part of the jet. If a gluon radiated from the jet thermalises with the medium, is it a part of the jet or the medium?

Thus, on the level of the reconstructed jet, energy loss manifests itself as broadening and softening of the jet. This is seen for example in jet-hadron correlations. Figure ?? shows $\Delta\eta$ correlations with the leading jet. $\Delta\phi$ correlations have similar trends. Jets in Pb–Pb are observed to be broader, with the greatest increase in the width for low momentum associated particles. This is consistent with expectations from partonic energy loss. These studies found that the subleading jet was broadened even more than the leading jet, indicating a bias towards selecting less

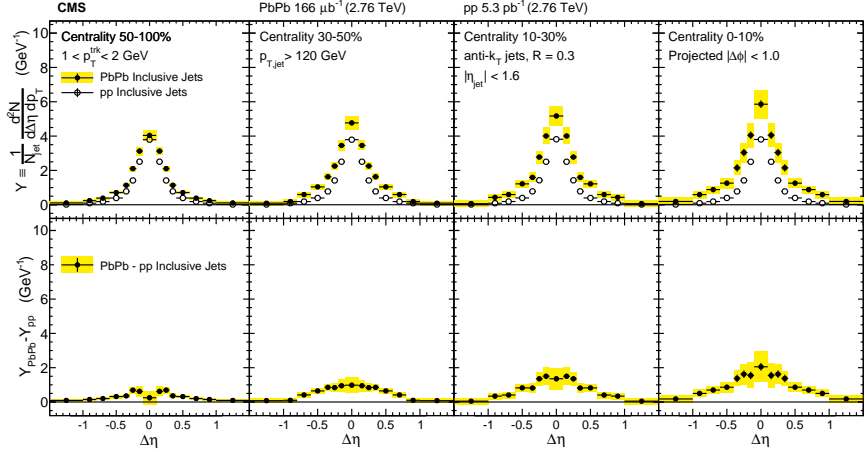


Figure 21: Measurement by CMS [145]. Symmetrized $\Delta\eta$ distributions correlated with Pb–Pb and pp inclusive jets with $p_T > 120$ GeV are shown in the top panels for tracks with $1 < p_T < 2$ GeV. The difference between per-jet yields in Pb–Pb and pp collisions is shown in the bottom panels. These measurements indicate that the jet is broadened and softened, as expected. The effect is stronger in more central collisions. $\Delta\phi$ correlations have similar trends.

modified jets as the leading jet. Jet hadron correlations have also been studied at RHIC with similar conclusion [144].

Thus the new paradigm in jet quenching in heavy-ion collisions involves multi-scale problems [146, 147]. The elementary scattering and the subsequent branching process down to non-perturbative scales are dominated by hard scales in the vacuum as well as in the medium. Soft scales, of the order of the temperature of the medium, characterise the interactions of soft partons produced in the shower with the QGP. Soft scales also rule hadronisation, which is expected to take place in vacuum for sufficiently energetic probes, even though some modifications can persist from modifications of colour flow [148–150]. Understanding the contributions from the different processes to the jet shower evolution in medium and their scale dependence is crucial to constrain the dynamics of jet energy loss in the expanding medium, the role of colour coherence [151], and fundamental medium properties like temperature dependent transport coefficient [152, 153].

Phase-space view of the medium modified parton cascade

Let us now look at medium modification of jets in a $\log(p) - \log(\theta)$ plane as shown in [146]. The different momentum and angular scales are subject to different physical phenomena. Figure 22 shows the relevant medium modification phenomena for different regions of the phase space at time t , when a jet propagates through

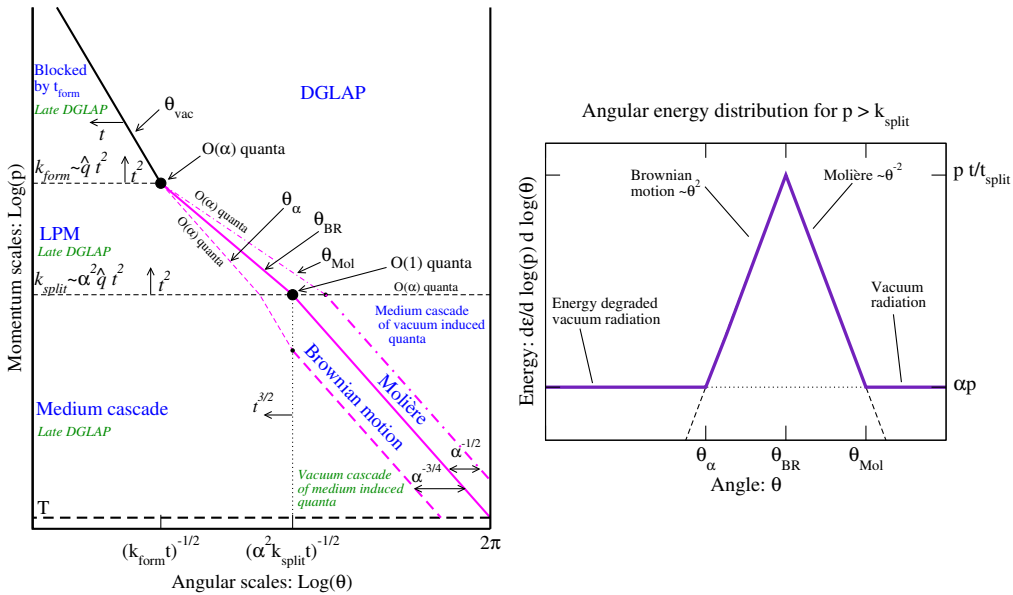


Figure 22: *Left:* Phase space view of dominant contributions in a medium-modified parton cascade. *Right* The distribution of energy as a function of angle for a fixed $p > k_{\text{split}}$. Large angular scales $\theta > \theta_{\text{Mol}}$ are dominated by DGLAP vacuum radiation from the leading parton at the scale Q . At $\theta < \theta_\alpha$ the energy density is dominated by vacuum radiation of the leading parton after it has degraded its energy propagating through the medium. Areas $\theta_\alpha < \theta < \theta_{\text{BR}}$ and $\theta_{\text{BR}} < \theta < \theta_{\text{Mol}}$ dominated by Brownian motion and rare large angle (Moli  re) scatterings [146].

859 a thermal cloud of temperature T . As in practice jets propagate over a finite
 860 path-length L in QCD matter, Fig. 22 can be taken as a representation of the
 861 distribution of partonic jet fragments at moment $t \approx L$, when the jet escapes the
 862 medium. [146]

863 The region marked as DGLAP is dominated by the primary vacuum splittings
 864 explained in section 1.4.2. This region is determined by $\theta > \theta_{\text{vac}}$ with

$$\theta_{\text{vac}} \propto 1/\sqrt{p_T}. \quad (40)$$

865 Medium-induced parton branching fills the $\log p$ - $\log \theta$ -plane from the bottom up
 866 (in p) and from the inside out (in θ). This is because transverse momentum is
 867 acquired by Brownian motion in the medium, $k_\perp^2 \propto \hat{q}t$. Then the formation time
 868 constraint $t \geq p/k_\perp^2 \approx p/\hat{q}t$ implies that medium-induced quanta can be formed in
 869 the region $p \leq k_{\text{form}}$ where

$$k_{\text{form}}(t) = \hat{q}t^2. \quad (41)$$

870 The probability of finding a splittee with a momentum p with $p < k_{\text{form}}$ is

$$\frac{dP_{\text{find}}(t)}{d \log p} \propto \alpha_s t/t_{\text{form}}(p) \propto \alpha_s \hat{q}^{nicefrac{1}{2}} p^{-1/2} t \quad (42)$$

871 Not all quanta will stay where they were created. Those modes that have time
 872 to lose a significant fraction of their energy will cascade to a significantly lower
 873 scale p . For LPM-type radiation, the splitting that degrades energy the most is
 874 the hardest splitting.

875 The $\log p$ distribution has the same $\frac{1}{\sqrt{p}}$ dependence as in the LPM region

$$\frac{dn}{d \log p} = \frac{1}{p} \frac{d\epsilon}{d \log p} \approx \alpha_s \frac{\sqrt{\hat{q}t}}{\sqrt{p}} \quad (43)$$

876 Also the quanta originating from the DGLAP region will undergo medium inter-
 877 actions that will make the quanta radiate and split. The distribution of radiation
 878 is the same as from any other mode. Above a certain momentum scale k_{split} the
 879 distribution of originating daughters is

$$\frac{dP_{\text{find}}}{d \log p d \log \theta} \approx \alpha_s \frac{t}{t_{\text{split}}(p)}, \quad (44)$$

880 Note that the ratio t/t_{split} is smaller than 1 for nodes above k_{split} and therefore
 881 the number of daughters is smaller than the number of vacuum splitted quanta.
 882 Below k_{split} the cascade is similar to the medium cascade and the number of quanta
 883 become

$$\frac{dn}{d \log p d \log \theta} \approx \alpha_s \frac{t}{t_{\text{split}}(p)}, \text{ for } p < k_{\text{split}}(p) \quad (45)$$

884 The angular distribution is driven by two mechanisms; Multiple soft scatterings
 885 give rise to transverse Brownian motion, which determines the distribution at small
 886 angles. The typical angle reached in the LPM region is

$$\theta_{\text{BR}}(p) \approx \frac{\sqrt{\hat{q}t}}{p}, \text{ for } k_{\text{form}} > p > k_{\text{split}}, \quad (46)$$

887 while in the medium cascade region of the phase space this becomes

$$\theta_{\text{BR}}(p) \approx \left(\frac{T}{p}\right)^{\frac{3}{4}} \quad (47)$$

888 Large angular scales cannot be reached by Brownian motion, but can arise from
 889 rare large angle scatterings with partons in the medium, described first by Molière [?].

890 Influence of jet on medium

891 Energy loss of hard partons is well established by experimental observations. Nat-
 892 urally energy can't just disappear, but is transferred to daughter partons or the
 893 medium. For radiation that stays inside the jet cone energy loss manifests itself
 894 as softening and broadening. If a daughter parton loses energy and becomes equi-
 895 librated with the medium it may no longer be correlated with the parent parton.
 896 This energy would then be distributed at distances far from the jet cone. There is
 897 some evidence for out-of-cone radiation by CMS [154], but the interpretation is not
 898 clear. Other possible phenomena include the mach cone and Molière scattering,
 899 but there is no experimental evidence for these. Evidence for all of these effects
 900 is difficult to find as the underlying event gives already a large and fluctuating
 901 background. Additionally its unclear how this energy would be different from the
 902 underlying event [5].

903 **1.5 QGP in Small systems**

904 After the existence of QGP in heavy-ion collisions has been established, attention
905 has been turned to small systems. Proton-proton (pp) and proton-Lead
906 ($p\text{-Pb}$) collisions have been studied at LHC and RHIC has studied a host of dif-
907 ferent collision systems; namely proton-gold ($p\text{Au}$) [?], deuteron-gold ($d\text{Au}$) [?]
908 and helium³-gold (He^3Au) [?] collisions starting from 2000.

909 Already before the era of modern colliders, collective behaviour in proton-
910 proton collisions was considered by names like Heisenberg, Fermi and Bjorken [6].
911 Eventually there were some experimental searches of QGP in pp and $p\bar{p}$ collisions
912 in E735 at Tevatron [155] and MiniMAX [156]. However no conclusive evidence
913 was found.

914 In the early years of RHIC these small systems were mostly considered as con-
915 trol measurement, for example in constraining nuclear modified parton distribution
916 functions (nPDFs) that determine the initial gluon distributions that determine
917 the first epoch of heavy-ion collisions [157, 158].

918 In 2010 ultrahigh-multiplicity pp collisions were studied at CMS [159]. The
919 study found that particles had a weak but clear preference to be emitted along a
920 common transverse ϕ angle across all rapidities [160]. This seemed like behaviour
921 were similar to AA collisions, but it was argued that it could as well come from
922 momentum correlations present in the earliest moments of the collision.

923 In 2012 LHC ran its first $p\text{-Pb}$ data taking period. Around the same time
924 $d\text{Au}$ data was re-examined at RHIC. Now it was revealed that most of the flow
925 signatures attributed to hydrodynamic expansion in AA collisions also existed in
926 smaller systems.

927 **1.5.1 Collective phenomena**

928 The most rugged analysis of collective behaviour concerns the two (or more) par-
929 ticle correlations, often parametrised via the relative azimuthal angle and pseu-
930 dorapidity differences, $\Delta\phi$ and $\Delta\eta$ respectively. Figure 23 shows two-particle
931 correlations measurements in Pb-Pb , $p\text{-Pb}$ and pp collisions at the LHC [161].
932 In Pb-Pb collisions long-range correlations dominate over short-range phenomena.
933 This shows in the two ridges at $\Delta\phi = 0$ and $\Delta\phi = \pi$. At $\Delta\phi \approx \Delta\eta \approx 0$, there is a
934 peak coming from single jet fragmentation. Since the away-side jet can be spread
935 out in $\Delta\eta$, this contribution disappears when compared to the flow contribution
936 at the away side ridge. In $p\text{Pb}$, and pp the near side peak is more distinguished
937 and the away-side jet contribution starts to show. Still, one can see long-range
938 correlations that seem like flow-like collective behaviour in both systems.

939 In addition to the two particle correlations, correlations have been observed in
940 the form of v_n coefficients both at LHC [162] and at RHIC [163]. The results have

also been described with hydrodynamical models, although the applicability of said models might be questionable, because of the large Reynolds numbers in small systems [164, 165]. Figure 24 shows results for v_2 in different collisions systems at RHIC as measured by PHENIX and Fig. 25 shows the eccentricities and the resulting hydrodynamic evolution in the systems. These different systems provide also different initial geometries. dAu collisions naturally have an ellipsoidal form, while a He³ collision has a triangular form and thus produces larger triangular flow, v_3 components.

Other observations that produce flow-like results include mass ordered v_2 coefficients [?] and higher order harmonics coming from fluctuations in the initial geometry [162]. Thus all the major collective flow phenomena observed in heavy-ion collisions have been also identified in small systems.

One open question is identifying the point the point, where flow-like correlations end. The question has proved challenging since low multiplicity events are dominated by non-flow phenomena. This makes observations in low multiplicity events model/method dependant. Different methods assess non-flow contributions differently. Thus some methods fail to observe a signal in cases, where others do and it is unclear whether this is true collective motion or it comes from non-flow contributions.

1.5.2 Absence of jet quenching

In A+A collisions, an important confirmation of the standard model comes from the energy loss of high p_T partons traversing the medium, as discussed in Sec. ???. Originally the interest in small systems was due to ruling out possible cold nuclear matter effects that might affect the results also in Pb-Pb. In 2003 the jet quenching effect was observed to disappear in d+Au collisions at RHIC [167–170]. This was taken as an indication that no QGP was created. Similarly at LHC no jet modification has been observed in pPb collisions. Fig. 26 shows the nuclear

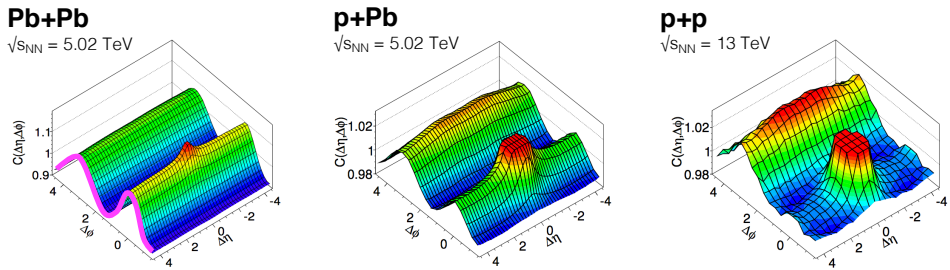


Figure 23: Two-particle correlation results in PbPb, pPb, and pp collisions at the LHC [161].

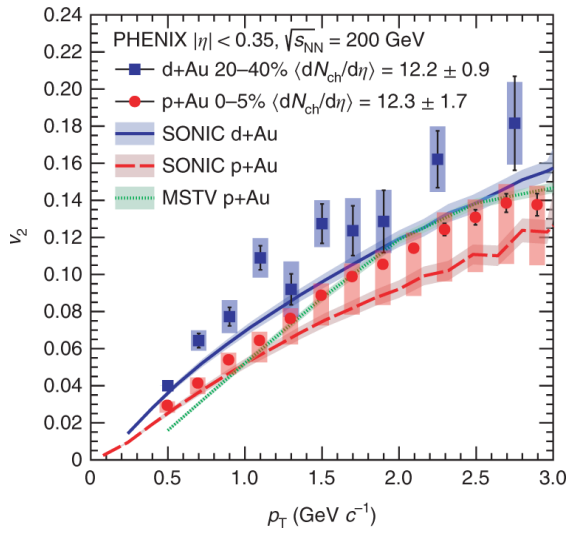


Figure 24: Comparison between hydrodynamic calculations and data from $p + \text{Au}$, $d + \text{Au}$ and ${}^3\text{He} + \text{Au}$ collisions [166]

modification factor R_{pA} and v_2 in pPb collisions as measured at the LHC [171,172].

Now the lack of jet modification seems surprising considering the multitude of flow observations supporting the existence of QGP in small systems. One possible explanation is simply the size of medium. In PbPb collision partons traversing

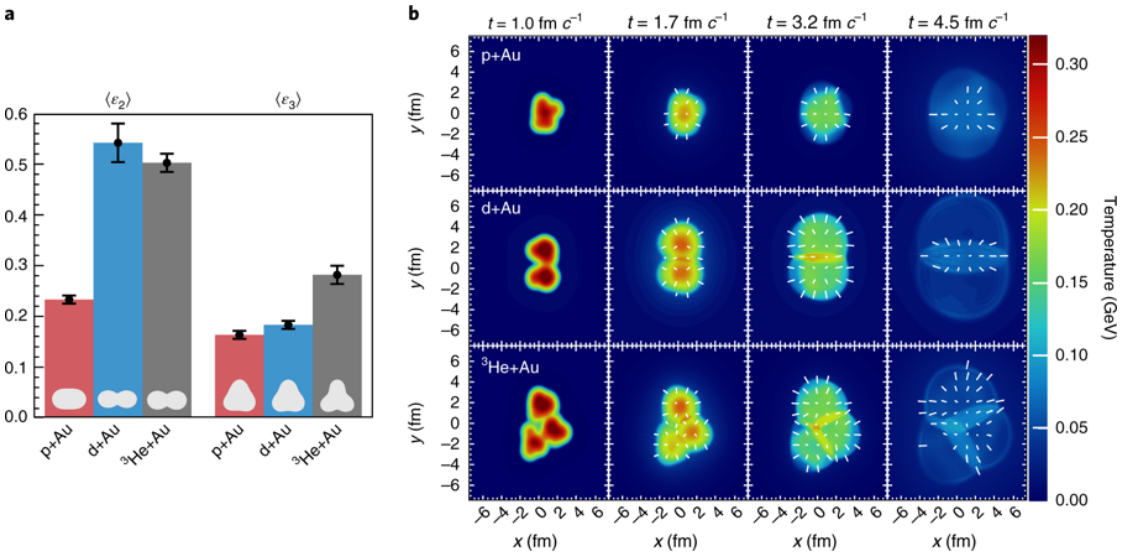


Figure 25: *left* Eccentricities in different systems. *right* Calculations of the initial energy density in small collision systems at RHIC and the resulting hydrodynamic evolution [166].

through the medium lose energy to the medium. If the medium is very small there is limited time for interaction with the medium. Reaction plane dependent R_{AA} measurements [?] in Pb–Pb collisions indicated that 2 fm could be the minimum path length required for energy loss.

Some calculations [173–175] indicate that there should be modification in the most central p–Pb collisions, but selecting these in the analysis is complicated [6]. In Pb–Pb collisions most of the particle production comes from the medium and thus the total multiplicity is a good indicator of centrality. However in p–Pb collisions the total multiplicity is smaller and is more strongly influenced by jet phenomena. Events with jets have naturally larger multiplicities and are more likely to be classified as central events.

So far the only observable indicative of jet quenching in pPb collisions is the high $p_T v_2$. In heavy-ion collisions this is not explained by hydrodynamics. Instead it is assumed to come from jet quenching with different path lengths through the medium in different directions. In Fig.26 ATLAS [172] and CMS [?] measurements of v_2 in pPb and PbPb collisions are shown. The pPb results seem to follow a very similar pattern.

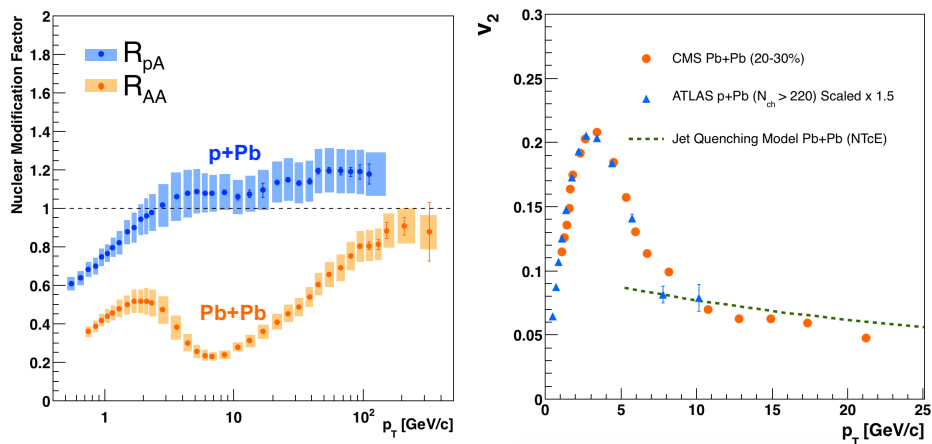


Figure 26: The nuclear modification factor R_{pA} in p–Pb collisions [171]. Compared to R_{AA} R_{pA} shows no sign of modification. *right* The v_2 coefficient as a function of p_T in Pb–Pb and p–Pb at the LHC [172, 173]. For shape comparison the p–Pb results have been scaled up by a factor 1.5.

Table 2: Summary of observations in small system

Observable	PbPb	pPb	pp
Jet RpA/RAA	Modified	No modification	-
Hadron RpA/RAA	Modified	No modification	-
Heavy flavors			
Jet shape	Broadening	No observations	-
Two-particle correlations	Ridge	Ridge	Ridge
v_2	Observed	Observed	Observed
Mass ordered flow			
Higher ordered harmonics			
High $p_T v_2$	Observed	Maybe	-

1.5.3 Centrality determination in small systems

In lead-lead collisions the total multiplicity of the event is a good indicator of the geometric centrality of the collision [?, 83]. In proton-lead collisions the connection between multiplicity and centrality is less clear [176]. In p–Pb collisions the impact parameter is only loosely correlated to N_{part} or N_{coll} . Hence, although one uses traditionally the term centrality to refer to these measurements, the relevant parameters are N_{part} and N_{coll} [176].

As in Pb–Pb collisions the Glauber model [79] is generally used to calculate geometrical quantities of p–Pb collisions. In this model, the impact parameter b controls the average number of participating nucleons N_{part} and the corresponding number of collisions N_{coll} . It is expected that variations of the amount of matter overlapping in the collision region will change the number of produced particles,

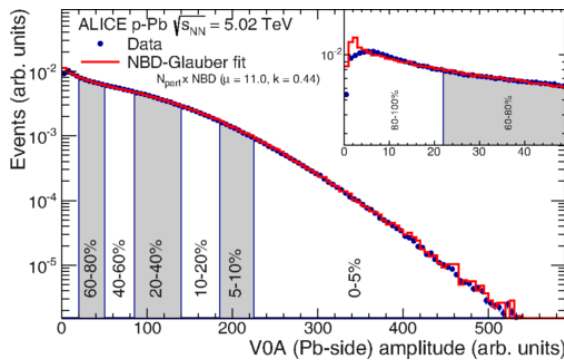


Figure 27: Distribution of the sum of amplitudes in the V0A hodoscopes (Pb-going), as well as the NBD-Glauber fit. Centrality classes are indicated by vertical lines. The inset shows a zoom-in on the most peripheral events. [176]

1001 and parameters such as N_{part} and N_{coll} have traditionally been used to describe
1002 those changes quantitatively, and to relate them to pp collisions. Figure 27 shows
1003 the measured V0A amplitude distribution in ALICE and the best NBD Glauber
1004 fit to the distribution [176].

1005 The problem in p–Pb collisions is that fluctuations in multiplicity coming from
1006 for example hard scatterings are of the same order as the differences in multiplicity
1007 between centrality classes. In Pb–Pb collisions these multiplicity fluctuations have
1008 little influence on the centrality determination as the range of N_{part} or N_{coll} is large
1009 and both $P(M|N_{\text{part}})$ and $P(M|N_{\text{coll}})$ converge quickly to a Gaussian with a small
1010 width relative to the range of $N_{\text{part}}/N_{\text{coll}}$. This is illustrated in Fig. 28. In practice
1011 selecting high multiplicity in p–Pb one chooses not only large average N_{part} , but
1012 also positive multiplicity fluctuations leading to deviations from the binary scaling
1013 of hard processes. These fluctuations are partly related to qualitatively different
1014 types of collisions. High multiplicity nucleon-nucleon collisions show a significantly
1015 higher mean transverse momentum. They can be understood either as harder
1016 collisions with larger momentum transfer Q^2 or as nucleon-nucleon collisions where
1017 multiple parton-parton interactions (MPI) take place.

1018 Of particular interest are estimators from kinematic regions that are causally
1019 disconnected after the collision. The measurement of a finite correlation between
1020 them unambiguously establishes their connection to the common collision ge-
1021 ometry. Typically these studies are performed with observables from well sep-
1022 arated pseudorapidity (η) intervals, e.g. at zero-degree (spectators, slow-nucleons,
1023 deuteron break-up probability) and multiplicity in the rapidity plateau.

1024 One centrality selection that is argued not to induce a bias on the binary scaling
1025 of hard processes is provided by the energy measurement with the Zero Degree
1026 Calorimeters (ZDC) in ALICE, due to their large η -separation from the central
1027 barrel detectors. They detect the "slow" nucleons produced in the interaction by
1028 nuclear de-excitation processes or knocked out by wounded nucleons [177].

1029 Additional kinematic biases exist for events containing high- p_{T} particles, which
1030 arise from the fragmentation of partons produced in parton-parton scattering with
1031 large momentum transfer. Their contribution to the overall multiplicity increases
1032 with increasing parton energy and thus can introduce a trivial correlation between
1033 the centrality estimator and the presence of a high- p_{T} particle in the event. For the
1034 very peripheral collisions, the multiplicity range that governs the centrality for the
1035 bulk of soft collisions can represent an effective veto on hard processes. For the
1036 nuclear modification factor this would lead to $R_{\text{pPb}} < 1$ [176].

1037 [More citations to final discussion?](#)

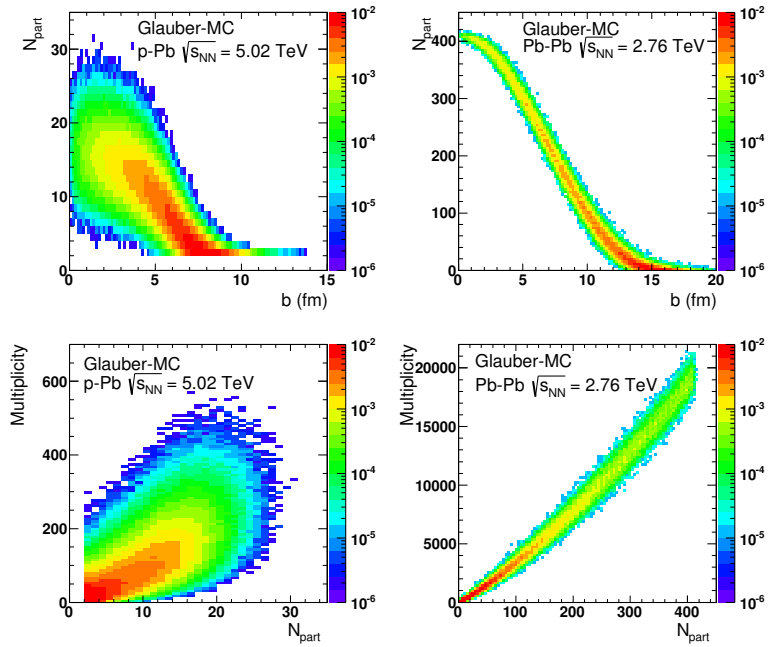


Figure 28: Top: Scatter plot of number of participating nucleons versus impact parameter; Bottom: Scatter plot of multiplicity versus the number of participating nucleons from the Glauber fit for V0A. The quantities are calculated with a Glauber Monte Carlo of p-Pb (left) and Pb-Pb (right) collisions. [176]

1038 2 Experimental Setup

1039 2.1 CERN

1040 The European Organization for Nuclear Research (CERN), established in 1954, op-
 1041 erates the largest particle physics laboratory in the world. In 2019 CERN consists
 1042 of 22 member states. Additionally CERN has contacts with a number of associate
 1043 member states and various individual institutions. The laboratory, also referred
 1044 to as CERN, itself is located near Geneva at the border of France and Switzerland
 1045 employs about 2500 people. Additionally some 12000 visiting scientists from over
 1046 600 institutions in over 70 countries come to CERN for their research.

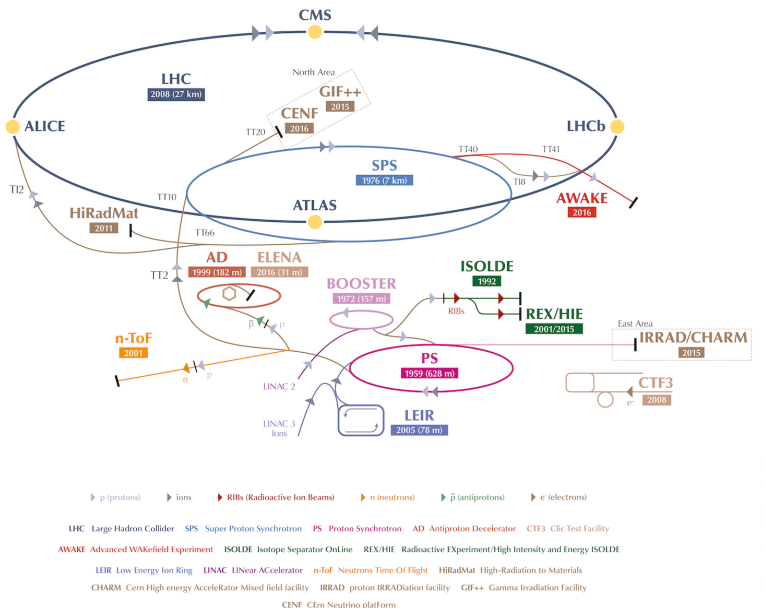


Figure 29: A schematic view of the accelerator complex at CERN. Before particles can be injected into the LHC they require a series of accelerators with increasing size. Until 2018 protons started their journey in LINAC2 (Linear Accelerator) and continue through the Booster, Proton Synchrotron (PS) and Super Proton Synchrotron (SPS). Between 2019 and 2020 LINAC2 will be replaced by LINAC4 [178]

1047 The laboratory includes a series of accelerators, which are used to accelerate
 1048 the particle beams used. A schematic view of the complex as of 2019 is shown in
 1049 Figure 29. In the framework of this thesis the most important component is the
 1050 Large Hadron Collider (LHC), the largest collider at CERN. LHC will be discussed

in more detail in Sec. 2.2. Other accelerators in the series are used to inject the particle beams into LHC, but they are also used in itself for various experimental studies.

The second largest accelerator is the super proton synchrotron (SPS). It is the final step before the particle beam is injected into LHC. Commissioned in 1976, it was the largest accelerator at CERN until the the Large Electron-Positron Collider (LEP) was finished in 1989. Originally it was used as a proton-antiproton collider and as such provided the data for the UA1 and UA2 experiments, which resulted in the discovery of the W and Z bosons [179]. At the moment there are several fixed target experiments utilising the beam from the SPS. These study the structure (COMPASS) and properties (NA61/SHINE) of hadrons, rare decays of kaons (NA62) and radiation processes in strong electromagnetic fields (NA63). Additionally the AWAKE and UA9 experiments are used for accelerator research and development.

The third largest accelerator in CERN is the proton synchrotron (PS). Capable of accelerating beams up to an energy of 25 GeV PS provides the beam to SPS. Additionally PS has experiments for studying strong force (DIRAC), the effect of cosmic rays on cloud formation (CLOUD) and neutron-nucleus interactions (nTOF).

Additionally PS provides the beam to the antiproton decelerator (AD), which uses the beam and a block of metal to produce antiprotons. These are then decelerated in AD into a useful low-energy beam, which is provided to a host of experiments studying the properties of antimatter.

PS gets proton beams from LINAC2 through BOOSTER and ion beams from LINAC3 through LEIR. From BOOSTER beams are also provided to the On-Line Isotope Mass Separator (ISOLDE). ISOLDE directs the beam into thick targets to produce low energy beams of radioactive nuclei. These beams are used to study the properties of even the most exotic of atomic nuclei in a host of experiments.

More information of the various experiments at CERN can be found online from [180].

2.2 Large Hadron Collider

The Large Hadron Collider (LHC) with its circumference of 26.7 km is the largest accelerator at CERN and the largest particle collider ever built. The LHC is designed to accelerate protons up to an energy of 8 TeV and lead ions up to 2.76 TeV per nucleon [181]. The design luminosity of the LHC is $10^{34} \text{ cm}^{-2}\text{s}^{-1}$. In 2017 it achieved a record peak luminosity of $2 \cdot 10^{34} \text{ cm}^{-2}\text{s}^{-1}$. For lead beams luminosities of up to $6 \cdot 10^{27} \text{ cm}^{-2}\text{s}^{-1}$ were reached in 2018. All this is achieved with a ring consisting of 1232 superconducting dipole magnets that keep particles in orbit.

1090 The LHC receives beams with energies of 450 GeV from the SPS. In the LHC
1091 the particles are accelerated through the use of radio-frequency (RF) cavities.
1092 Electromagnetic waves become resonant and build up inside the cavity. As they
1093 consist of electromagnetic waves, the field in the RF cavity oscillates. Charges
1094 passing through the cavity feel the overall force and are pushed forward along the
1095 accelerator. Particles must enter the cavity at the correct phase of oscillation to
1096 receive a forward push. When timed correctly, the particles will feel zero acceler-
1097 erating voltage when they have exactly the correct energy. Particles with higher
1098 energies will be decelerated and particles with lower energies will be accelerated.
1099 This focuses particles in distinct bunches. The RF oscillation frequency at the
1100 LHC is 400.8 MHz. Thus RF "buckets" are separated by 2.5 ns. However only 10
1101 % are actually filled with particles, so the bunch spacing in the LHC is 25 ns, at
1102 a bunch frequency of 40 MHz.

1103 With 7 TeV proton beams the dipole magnets used to bend the beam must
1104 produce a magnetic field of 8.33 T. This can be only achieved through making
1105 the magnets superconducting, which requires cooling them down with helium to a
1106 temperature of 1.9 K. The 1232 dipole magnets make up roughly 2/3 of the LHC
1107 circumference. The remaining part is made up of the RF cavities, various sensors
1108 and higher multipole magnets used to keep the beam focused. The most notable
1109 of these are the 392 quadrupole magnets.

1110 The LHC is divided into octants, where each octant has a distinct function.
1111 Octants 2 and 8 are used to inject beam into the LHC from SPS. The 2 beams
1112 are crossed in octants 1,2,5 and 8. The main experiments are built around these
1113 crossing points. Octants 3 and 7 are used for beam cleansing. This is achieved
1114 through collimators that scatter particles with too high momentum or position
1115 offsets off from the beam. The RF cavities used for acceleration are located in
1116 octant 4 and octant 6 is used for dumping the beam. The beam dump is made
1117 up of two iron septum magnets, one for each beam, that will kick the beam away
1118 from machine components into an absorber when needed.

1119 2.2.1 LHC experiments

1120 As of 2018 there are four main experiments at the LHC; ALICE, ATLAS, CMS
1121 and LHCb and three smaller ones LHCf, TOTEM and MoEDAL. ALICE will be
1122 covered in detail in section 2.3.

1123 ATLAS (A Toroidal LHC ApparatuS) and CMS (Compact Muon Solenoid) are
1124 the two largest experiments at the LHC. They are both multipurpose experiments
1125 designed to be sensitive to many different possible new physics signals, such as ex-
1126 tra dimensions and dark matter particles. The biggest discovery made by these so
1127 far is the discovery of the Standard Model Higgs boson, which was simultaneously
1128 published by the experiments in 2012 [182,183].

1129 The LHCb (LHC beauty) experiment [184] is made for studying the bottom
1130 (beauty) quark. Main physics goals of the LHCb include the measurement of the
1131 parameters of CP violation with decays of hadrons containing the bottom quark.
1132 One of the most important results published by LHCb is the first measurement of
1133 $B_s^0 \rightarrow \mu^+ \mu^-$ decay, which was found to be in line with the Standard Model.

1134 In addition to the four large experiments there are three smaller experiments
1135 along the LHC ring. LHCf (LHC forward) [185] is located at interaction point 1
1136 with ATLAS. It aims to simulate cosmic rays by the particles thrown forwards by
1137 the collisions in ATLAS.

1138 TOTEM (TOTal Elastic and diffractive cross section Measurement) is located
1139 near the CMS experiment at point 5. This allows it to measure particles emerging
1140 from CMS with small angles. The main goals is to measure the total, elastic and
1141 inelastic cross-sections in pp collisions [186].

1142 The MoEDAL (Monopole and Exotics Detector At the LHC) experiment [187]
1143 is located at the interaction point 8 together with the LHCb experiment. MoEDAL
1144 tries to measure signatures of hypothetical particles with magnetic charge, mag-
1145 netic monopoles.

1146 2.3 ALICE

1147 ALICE (A Large Ion Collider Experiment) [188] is the dedicated heavy ion ex-
1148 periment at the LHC. ALICE was designed to cope with the expected very high
1149 multiplicity environment of heavy ion collisions. The design allows measurement
1150 of a large number of low momentum tracks. The different detector subsystems are
1151 optimised to provide high momentum resolution and excellent particle identifica-
1152 tion capabilities over a broad range of momentum.

1153 A schematic view of the ALICE detector in 2018 is presented in Figure 30.
1154 This section will go through the composition of ALICE as it has been during run 2
1155 between 2014 and 2018. The detector will go through significant upgrades during
1156 Long Shutdown 2 (LS2) in 2019-2020.

1157 As in all the major high energy physics experiments the positioning of the de-
1158 tectors follows a layered structure. Closest to the interaction point are the tracking
1159 detectors. The main task of these detectors is to locate the position of the pri-
1160 mary interaction vertex accurately and to record the tracks of charged particles.
1161 To achieve this they need a very good spatial resolution close to the interaction
1162 point. Tracking detectors do not significantly alter the tracks of traversing parti-
1163 cles. Thus they can be located in the innermost layers.

1164 Calorimeters are designed to stop any particles hitting them and use the ab-
1165 sorption to measure the energy of the particles. Thus they must be located behind
1166 the tracking detectors. ALICE has two separate calorimeter systems, the elec-
1167 tromagnetic calorimeters measure mainly electrons and photons, while the muon

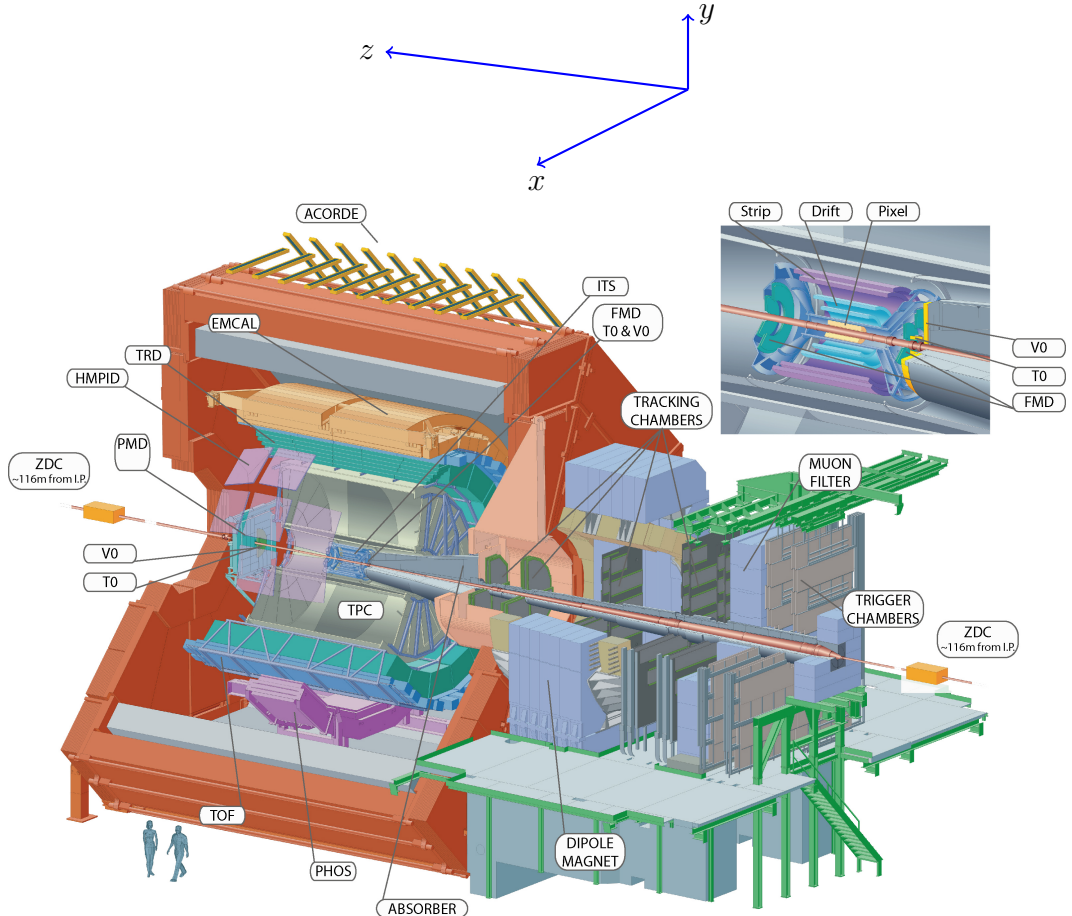


Figure 30: Schematic view of the ALICE detector with the definition of coordinates. The positive direction of *z* is also referred to as the A side and the negative direction as the C side

₁₁₆₈ detection system measures muons.

₁₁₆₉ 2.3.1 Tracking

₁₁₇₀ The main design guideline for the tracking detectors in ALICE was the require-
₁₁₇₁ ment to have good track separation and high granularity in the high multiplicity
₁₁₇₂ environment of heavy ion collisions. Before the LHC started heavy ion runs the
₁₁₇₃ wildest estimates put the particle density at 8000 charged particles per unit of ra-
₁₁₇₄ pidity [188]. In reality the particle density turned out to be significantly smaller,
₁₁₇₅ about 1600 charged particles per rapidity unit [189].

₁₁₇₆ The main tracking detector in ALICE is the Time Projection Chamber
₁₁₇₇ (TPC) [190]. TPS is discussed in more detail in section 2.3.2

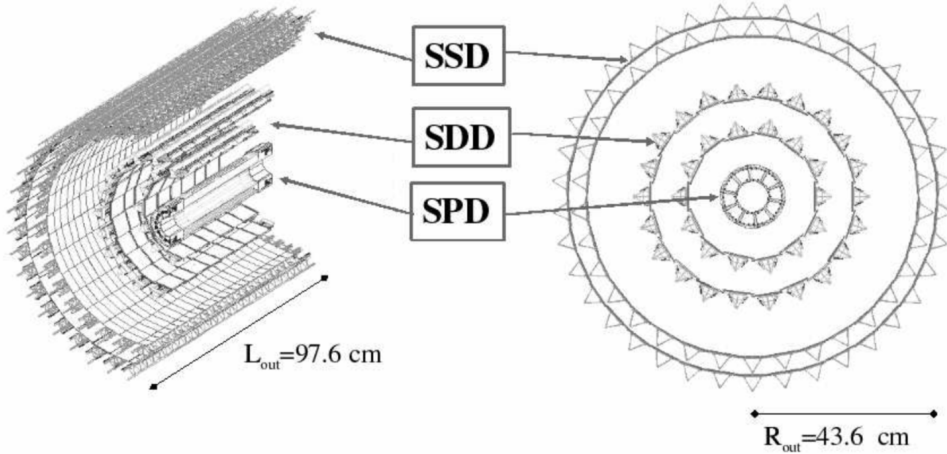


Figure 31: Schematic view of ALICE Inner Tracking System

1178 Between TPC and the beam pipe there is an array of six layers of silicon
 1179 detectors, called the inner tracking system (ITS) [191]. The main tasks of the
 1180 ITS are to locate the primary vertex with a resolution better than $100 \mu\text{m}$, to
 1181 reconstruct the secondary vertices from decaying particles, to track and identify
 1182 particles with momenta below 200 MeV and to compliment the momentum and
 1183 angle measurements of TPC. During long shutdown 2 in 2019-2020 the entire ITS
 1184 will be replaced [192]. As of 2018 the two innermost layers are made of the silicon
 1185 pixel detector (SPD). As it is the closest detector to the interaction point it requires
 1186 a very high spatial resolution. Thus the choice of pixel technology is natural. In
 1187 heavy ion collisions the particle density is around 50 particles per cm^2 .

1188 The next two layers together are the silicon drift detector (SDD). The layers
 1189 are made out of homogeneous neutron transmutation doped silicon, that is ionized
 1190 when a charged particle goes through the material. The generated charge then
 1191 drifts to the collection anodes, where it is measured. The maximum drift time
 1192 in SDD is about $5 \mu\text{s}$. This design gives very good multitrack capabilities and
 1193 provides two out of the four dE/dx samples in the ITS.

1194 The two remaining layers in the ITS are the silicon strip detector (SSD). The
 1195 strips work in a similar way as silicon pixels, but by itself one layer only provides
 1196 good resolution in one direction. Combining two crossing grids of strips provides 2
 1197 dimensional detection. Each charged particle will hit two intervening strips. The
 1198 position of the hit can be deduced from the place where the strips cross each other.

₁₁₉₉ **2.3.2 TPC**

₁₂₀₀ The time projection chamber (TPC) is a cylindrical detector filled with 88 m^3
₁₂₀₁ of Ne – CO₂ (90/10 %) gas mixture. The gas is contained in a field cage that
₁₂₀₂ provides an uniform electric field of 400 V/cm along the z-axis. Charged particles
₁₂₀₃ traversing through the TPC volume will ionise the gas along their path. This
₁₂₀₄ liberates electrons that drift towards the end plates of the cylinder. A schematic
₁₂₀₅ of the TPC is shown in Fig. 32.

₁₂₀₆ The field cage is separated into two detection volumes by the central high
₁₂₀₇ voltage electrode. Both sides have a drift length of 2.5 m and inner and outer
₁₂₀₈ diameters of 1.2 m and 5 m respectively. This means the central electrode must
₁₂₀₉ provide a maximum potential of 100 kV to achieve the design field magnitude. The
₁₂₁₀ maximum time required for electrons to drift through the chamber is about 90 μs .

₁₂₁₁ When electrons reach the end of the main cylinder they enter the readout
₁₂₁₂ chambers. The readout section of both sides consists of 18 outer chambers and
₁₂₁₃ 18 inner chambers. Each of them is made of multiwire proportional chambers
₁₂₁₄ with cathode pad readouts. This design has been used in many TPCs before.
₁₂₁₅ During LS2 in 2019-2020, the multiwire chambers will be replaced by Gas Electron
₁₂₁₆ Multipliers (GEMs, see section 2.3.3).

₁₂₁₇ **2.3.3 TPC upgrade**

₁₂₁₈ During LS2 in 2019-2020 ALICE will go through significant modifications. The
₁₂₁₉ goal is to be able have continuous readout [193] in heavy ion collisions at an
₁₂₂₀ interaction rate of 50 kHz. ALICE will add a new Forward Interaction trigger
₁₂₂₁ (FIT) to replace the V0 and T0 detectors.

₁₂₂₂ Additionally the current inner tracking system (ITS) will be completely re-
₁₂₂₃ placed. The current layered structure with three different technologies will be
₁₂₂₄ replaced by an all pixel detector with significantly reduced pixel size. Additionally
₁₂₂₅ the first layer will be brought closer to the beam pipe. The new ITS will have
₁₂₂₆ better tracking efficiency and better impact parameter resolution.

₁₂₂₇ The muon detection will be complimented by the Muon Forward Tracker
₁₂₂₈ (MFT) [194]. Based on the same technology as the new ITS, MFT will be placed
₁₂₂₉ before the hadron absorber that sits in front of the existing muon spectrometer.
₁₂₃₀ MFT should significantly increase the signal/background ratio in heavy quark
₁₂₃₁ measurements.

₁₂₃₂ Many subdetectors will make small improvements to enhance the readout rate.
₁₂₃₃ The central trigger processor will be replaced and ALICE will introduce a new
₁₂₃₄ framework O^2 that combines both online data acquisition and offline analysis.

₁₂₃₅ The detector restricting the readout the most at the moment is the TPC.
₁₂₃₆ The current wire chamber based system limits the readout rate to 3.5 kHz. To

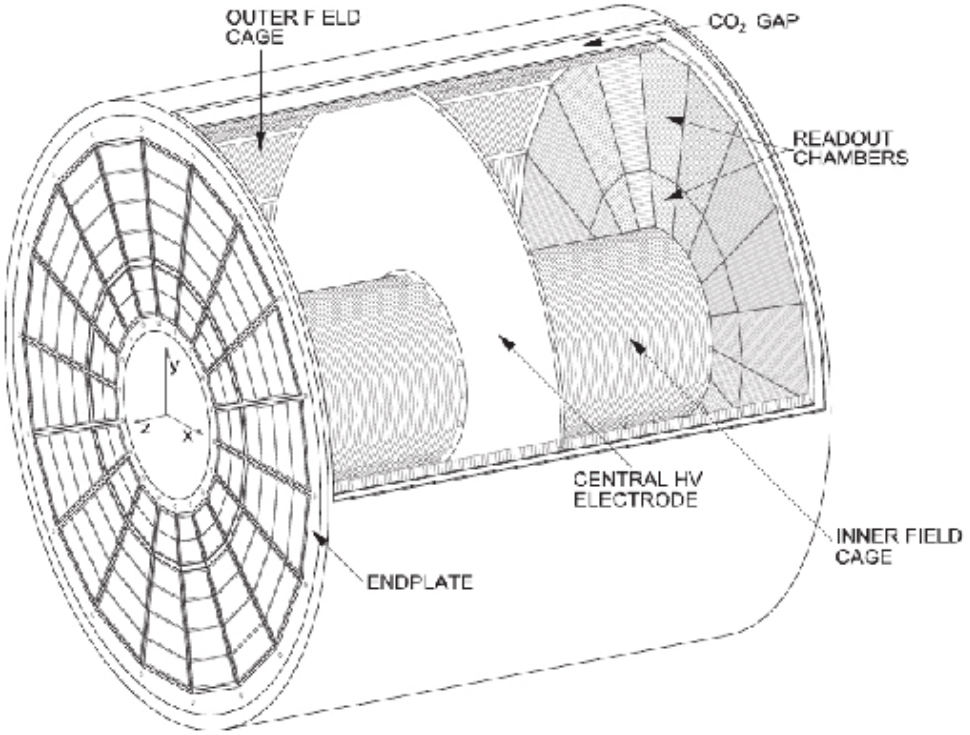


Figure 32: Schematic view of ALICE Time Projection Chamber

1237 achieve the 50 kHz readout rate goal the wire chambers will be replaced by a Gas
 1238 Electron Multiplier (GEM) based system. The GEMs are designed to minimise
 1239 ion backflow to allow continuous, ungated and untriggered readout. I have made
 1240 a personal contribution to the quality assurance of the new GEM readout of TPC.

1241 TPC has a total of 36 inner and 36 outer readout chambers. Each of these will
 1242 consist of 4 layers of GEM foils. The inner chambers will only have one foil for
 1243 each layer. The outer chambers are separated into three sections, each with its
 1244 own layer of foils. Each GEM foil is made up of a $50 \mu\text{m}$ thick resistive capton
 1245 layer, coated on both sides by $5\mu\text{m}$ thick layers of copper. Each foils is separated
 1246 into a number (20-24 depending on the size of the foil) of distinct active areas.
 1247 The active areas are pierced densely with holes. They have 50-100 holes in the
 1248 area of a single mm^2 . The density of holes changes from layer to layer. The two
 1249 middle layers of foils have a larger (double) pitch (smaller hole density) while the
 1250 top and bottom layers have a smaller (normal) pitch (larger hole density).

1251 The purpose of the multilayered structure is to reduce the ion backflow [?]; not
 1252 only one layer of GEM foils will be installed, but a 4 layer stack. In the stack there
 1253 are 2 standard pitch GEM foils, where the pitch size, i.e. the separation of the

holes inside a foil is around $140 \mu\text{m}$, and 2 large pitch GEM foils, there the hole spacing is two times larger, $280 \mu\text{m}$. The two outer layers will have standard pitch and the two middle layers have large pitch. The middle layers with large pitch serve as extra insulator against the ion backflow. Additionally the setup allows operating individual GEM foils at lower voltages and still have an increase in the gain of a few orders of magnitude. [195]

The holes have a conical shape which they acquire during a two step chemical etching process. The designed inner and outer diameters of the holes are $50 \pm 5 \mu\text{m}$ and $70 \pm 5 \mu\text{m}$ respectively. Fig. 33 shows the cross-section of a hole alongside with the operation principle of a GEM foil.

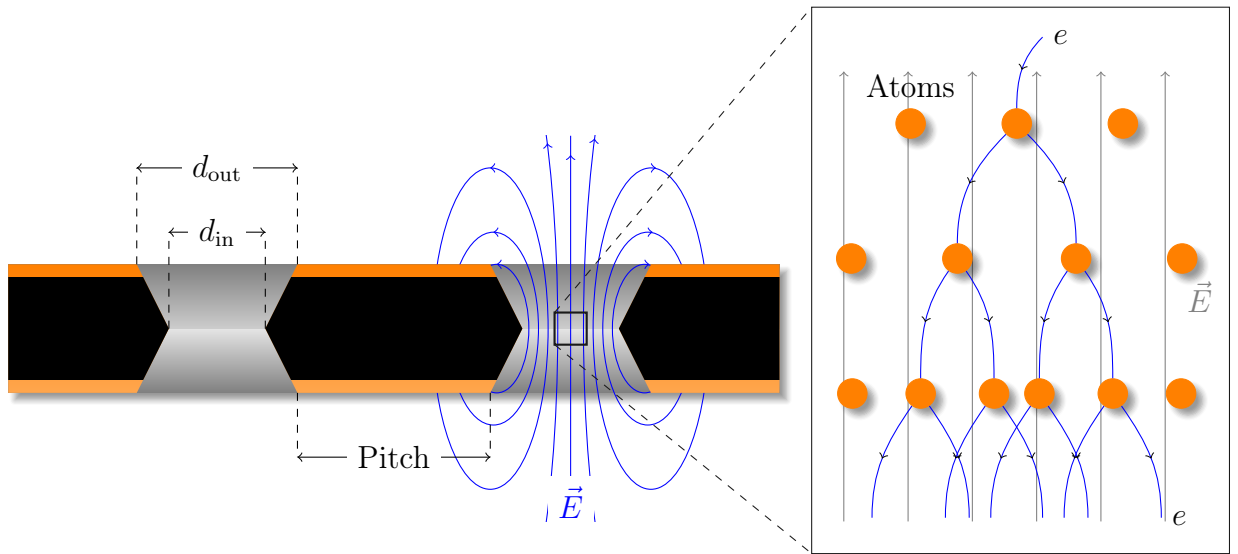


Figure 33: *left* Cross-section of a GEM foil. (Not to scale). The hole diameters are $d_{\text{in}} = 50 \pm 5 \mu\text{m}$ and $d_{\text{out}} = 70 \pm 5 \mu\text{m}$ and pitch is either 140 or 280 μm . *right* The amplification of a GEM foil is based on the Townsend avalanche phenomenon. Electrons entering the electric field inside the hole are accelerated. If they gain enough energy before colliding with atoms they can liberate additional electrons, which are further accelerated leading to a chain reaction.

The working principle of these foils is based on the Townsend avalanche phenomenon, which is also used in proportional counters such as Geiger counters. There is a large potential difference (140-400 V) applied to the two sides of the foil, which results in large field in each hole. Electrons gain energy in the field and if the electric field is strong enough, the free electron can gain sufficient velocity (energy) to liberate another electron when it next collides with a molecule. The two free electrons then travel along the electric field and can gain sufficient energy from the electric field to cause further impact ionisations, and so on, leading to a

chain reaction. Under the right conditions a single electron entering any hole will create an avalanche containing 100–1000 electrons; this is the gain of the GEM foil.

As opposed to wire chambers, which typically have one voltage setting, a GEM-based detector requires several independent voltage settings: there is a drift voltage which drives the electrons from the ionisation point to the GEM, an amplification voltage, and an extraction voltage that brings electrons from the GEM exit to the readout plane. In a multilayer system this is further complicated by the voltages between layers of foils.

Quality Assurance of the GEM foils

The GEM foils are produced at CERN, where they will undergo a basic QA (QA-B) procedure, that includes a coarse optical inspection for any large defects ($\gtrsim 1\text{ mm}$) and a short term high voltage measurement. Afterwards the foils are sent for an advanced quality assurance (QA-A) procedure which is performed in one of the two QA-A centers, one in the Helsinki Institute of Physics (HIP) and one in the Wigner Research Centre in Budapest. Details of the QA-A procedure can be found in the thesis of Márton Vargyas [196] and in [197]. In the QA-A centers all foils are put through a detailed optical scanning process and a long term high voltage measurement. I was personally performing the QA production in Helsinki for the final 6 months of the project.

The optical scan is performed with the help of a scanning robot. The setup along with most of the software was developed at the Detector Laboratory of the Helsinki Institute of Physics [198]. The optical scan is able to distinguish every single hole on the GEM foil and measure their properties. The purpose of the scan is two-fold; to catch defects that could affect the performance and classify the foils based on their hole parameters. It is expected that these are connected with the foil's electric properties [198]. For example, smaller holes create more intense and focused fields, which would result in larger amplification of their avalanche electrons, i.e. the local gain is expected to be larger.

After the optical scanning, the foils are subjected to a long term (5-12 hours) high voltage leakage current measurement. Each segment of the GEM foil is connected to a high voltage of 500 V and the leakage current is measured separately for each segment. The accepted leakage current in each segment is 0.16 nA.

Foils that fail the criteria are either trashed or sent to CERN for recleaning or repairing, after which they will go through the QA pipeline again.

Additionally some foils will be put through a gain mapping procedure. As it is time consuming can only be performed in the QA-A center in Budapest it is only a small subset of foils. However, by measuring the gain in some foils the gain can be correlated with foil properties. Thus the single foil gain can be predicted based

1311 on the results of the optical scan. Details can be found in [196].

1312 2.3.4 Particle identification

1313 One guiding principle in the design of ALICE was to achieve good particle iden-
1314 tification (PID) over a large part of phases space and for several different particle
1315 types. In ALICE there are several detectors taking part in the identification of
1316 particles.

1317 One of the particle identification detectors is the transition radiation detector
1318 (TRD) [199]. Its main task is identifying electors with momenta larger than 1 GeV.
1319 Transition radiation is produced when highly relativistic particles traverse the
1320 boundary between two media having different dielectric constants. The average
1321 energy of the emitted photon is approximately proportional to the Lorentz factor γ
1322 of the particle, which provides an excellent way of discriminating between electrons
1323 and pion. ALICE TRD is made of a composite layer of foam and fibres. The
1324 emitted photons are then measured in six layers of Xe/CO₂ filled time expansion
1325 wire chambers.

1326 The time of flight (TOF) detector [200] uses a very simple physics principle,
1327 i.e. calculating the velocity of the particle using the time of flight between two
1328 points. Combining this with the momentum of particle, obtained from the tracking
1329 detectors, one can calculate the mass of the particle, which identifies particles. The
1330 TOF detector consists of multigap resistive wire chambers. These are stacks of
1331 resistive plates spaced equally. They allow time of flight measurements in large
1332 acceptance with high efficiency and with a resolution better than 100 ps.

1333 The third specific particle identification detector is the high momentum particle
1334 identification (HMPID) detector [201]. The HMPID uses a ring imaging Cherenkov
1335 counter to identify particles with momenta larger than 1 GeV. Particles moving
1336 through a material faster than the speed of light in the material will produce
1337 Cherenkov radiation. The velocity of the particle determines the angle at which
1338 the radiation is emitted. Measuring this angle gives the velocity of the particle.
1339 This can be again used to calculate the mass of the particle, if the momentum is
1340 known. In HMPID the material is a liquid radiator and the photons are measured
1341 with multiwire proportional chambers in conjunction with photocathodes.

1342 In addition to the specific particle identification detectors, the general purpose
1343 tracking detectors can be used for identification through the use of specific energy
1344 loss of charged particles traversing through a medium and the transition radiation
1345 emitted by charged particles when crossing the boundary between two materials.

1346 dE/dx measurements are provided by the last four layers of the ITS detector,
1347 i.e. the SDD and the SSD, thanks to their analog readout [202]. ITS can provide
1348 particle identification in the low p_T region, up to 1 GeV, and pions reconstructed in
1349 the standalone mode can be identified down to 100 MeV. Similar to ITS the TPC

1350 detector provides specific energy loss measurements. TPC can identify charged
1351 hadrons up to p_T $1 - 2$ GeV as well as light nuclei, He3 and He4.

1352 2.3.5 Electromagnetic Calorimeter

1353 Calorimeters are designed to measure the energy of particles. Electromagnetic
1354 calorimeters specialise in detecting particles that interact primarily through the
1355 electromagnetic interaction, namely photons and electrons. They are required in
1356 many neutral meson and direct photon analyses. In addition the energy informa-
1357 tion enhance jet measurements.

1358 ALICE has two electromagnetic calorimeters, the photon spectrometer
1359 (PHOS) [203] and the electromagnetic calorimeter (EMCal) [204]. PHOS is a
1360 homogeneous calorimeter that consists of scintillating PbWO_4 crystals, which
1361 generate a bremsstrahlung shower and produce scintillation light. The energy of
1362 the particle determines the amount of light produced. To improve the charged
1363 particle rejection, PHOS includes a charged particle veto detector (CPV) [?].
1364 PHOS is built to have a very fine granularity, making it well suited for measuring
1365 direct photons and neutral mesons.

1366 In comparison to PHOS, EMCal has coarser granularity, but a significantly
1367 larger acceptance, making it suitable for jet physics. The acceptance of EMCal in
1368 the azimuthal angle is $80 \text{ deg} < \phi < 187 \text{ deg}$. During long shutdown 1 in 2013-
1369 2015, EMCal was extended with the di-jet calorimeter (DCal) [205], giving an
1370 additional acceptance region of $260 \text{ deg} < \phi < 320 \text{ deg}$. This provides partial
1371 back-to-back coverage.

1372 EMcal is segmented into 10 full size super modules (SM), 5 for A side and 5 for
1373 C side, and two 1/3 sized SMs, one for each side. This segmentation can be seen
1374 in Fig. 34. Each SM is divided into 24 strips, each covering full η (24 towers) and
1375 2 towers in η . Each strip is composed of 2×2 tower modules. Thus each full size
1376 super module includes 1152 towers and in total the EMCal is made up of 12288
1377 towers.

1378 The build of individual towers is shown in Fig. 35. Each tower is built up from
1379 76 alternating layers of 1.44 mm Pb and 77 layers of 1.76 mm polystyrene base
1380 injection moulded scintillator. The lead tiles produce the shower and scintillator
1381 tiles the light. Each tower scintillator is equipped with reflectors on all sides
1382 to provide better gain and keep the four towers inside one module isolated. The
1383 scintillation photons produced in the active volume of the tower are collected by 36
1384 longitudinally placed wave length shifting light guide fibres. The light is eventually
1385 directed to the Avalanche Photo Diodes (APD) for readout.

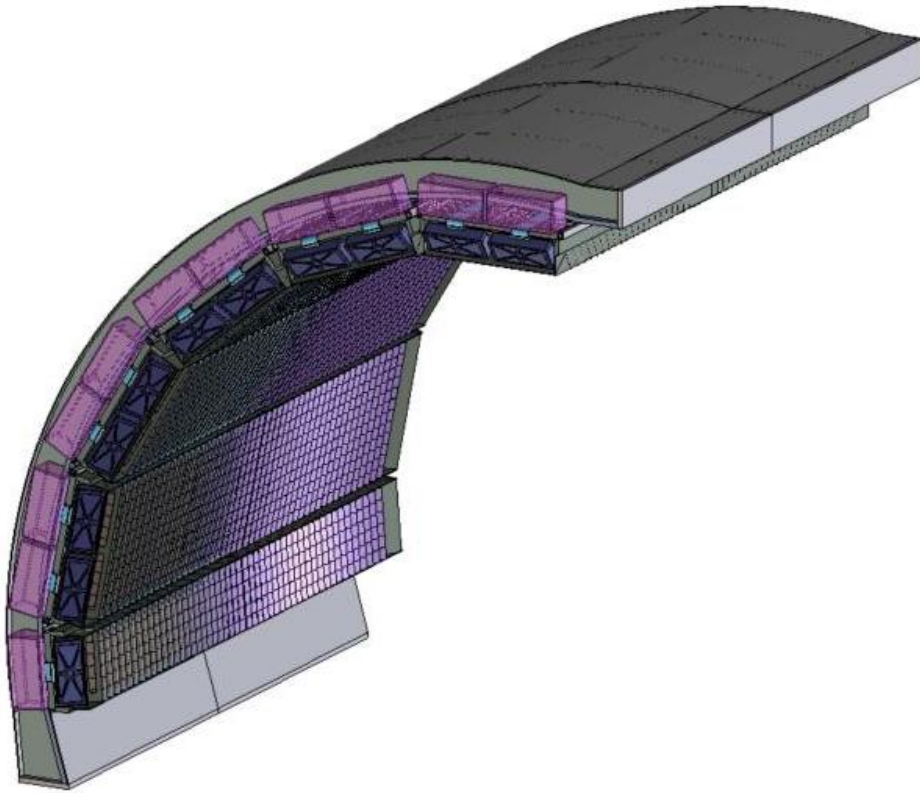


Figure 34: The EMCal detector arc, where the segmentation into 10 full size and 2 $\frac{1}{3}$ -sized (5 and 1 per side) supermodules can be seen.

2.3.6 Forward and trigger detectors

ALICE includes a few small and specialised detectors of importance. The event time is determined with very good precision (< 25 ns) by the T0 detector [206]. T0 consists of two sets of Cherenkov counters that are mounted around the beam pipe on both sides of the interaction point. T0 gives the luminosity measurement in ALICE.

Another small detector in the forward direction is the V0 detector [206]. This consists of two arrays of segmented scintillator counters located at $-3.7 < \eta < -1.7$ and $2.8 < \eta < 5.1$. V0 is used as a minimum bias trigger and for rejection of beam-gas background. Particle multiplicity in the forward direction can be related to the event centrality. Thus V0 is the main detector used in centrality determination in PbPb collisions.

The multiplicity measurement of V0 is complimented by the forward multiplicity detector (FMD) [206]. FMD includes five rings of silicon strip detectors that

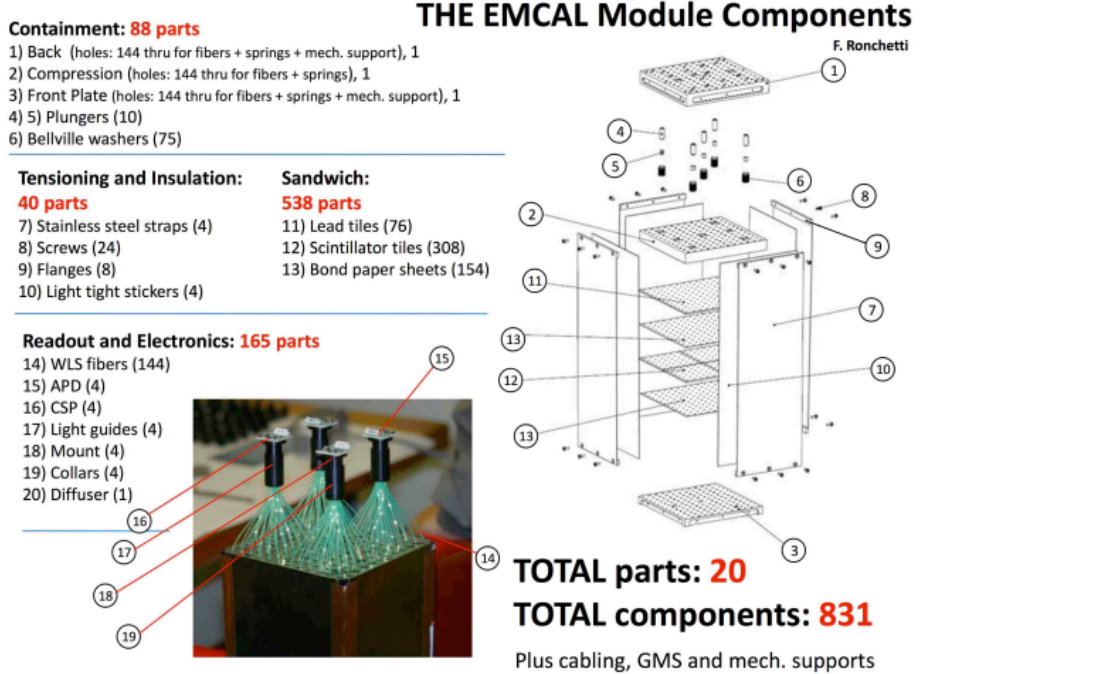


Figure 35: The exploded EMCAL tower view

make up the FMD. FMD gives acceptance in the range $-3.4 < \eta < -1.7$ and $1.7 < \eta < 5.0$.

During long shutdown 2 in 2019-2020, V0 and T0 will be replaced by the Fast Interaction Trigger (FIT) detector [207]. For historical reasons elements of FIT are also referred to as V0+ and T0+. FIT will allow centrality, event plane, luminosity and interaction time determination in the continuous readout mode, that ALICE will operate in after 2020.

For photon multiplicity measurement ALICE has the photon multiplicity detector (PMD) [208]. PMD uses two planes of gas proportional counters with a cellular honeycomb structure. PMD gives the multiplicity and spatial distribution of photons in the region $2.3 < \eta < 3.7$.

On top of the ALICE magnet there is an array of 60 large scintillators called the ALICE cosmic ray detector (ACORDE) [209]. ACORDE is used as a trigger for cosmic rays for calibration and alignment.

The only hadronic calorimeters in ALICE are the zero degree calorimeters (ZDC) [210], which are located next to the beam pipe in the machine tunnel about 116 m from the interaction point. There are two sets of calorimeters. One is made of tungsten, specialising in measuring neutrons, while the other, made of

1418 brass, is specialised in measuring protons. ZDC is meant to detect spectators, i.e.
1419 parts of the colliding ions that do not take part in the interaction. If there are more
1420 spectators, the collisions is likely to be more peripheral. Thus ZDC gives informa-
1421 tion about the centrality of the event especially in proton-lead collisions [176], but
1422 also in Pb–Pb collisions [83].

1423 A new detector installed during the long shutdown 1 is the ALICE diffractive
1424 detector (AD) [?]. AD consists of two assemblies, one in each side of the interaction
1425 point, both made of two layers of scintillators. These assemblies are situated about
1426 17 m and 19.5 m away from the interaction points. The pseudorapidity coverage is
1427 $-6.96 < \eta < -4.92$ and $4.78 < \eta < 6.31$. AD greatly enhances ALICE’s capability
1428 for diffractive physics measurements that require a large pseudorapidity gap.

1429 2.3.7 Muon spectrometer

1430 Outside the main magnet, ALICE has a spectrometer dedicated to measuring
1431 muons [211]. In heavy ion physics muons are mainly used to measure the produc-
1432 tion of the heavy quark resonances J/ψ , Ψ' , Υ , Υ' and Υ'' .

1433 The muon spectrometer consists of three parts, the absorber, the muon tracker
1434 and the muon trigger. The absorber is meant to remove the hadronic background
1435 as efficiently as possible. After the absorber there are ten plates of thin cathode
1436 strip tracking stations with high granularity, the muon tracker. After the muon
1437 tracker there is a layer of iron to filter out any remaining particles, other than
1438 muons. The muon trigger is located behind this layer. The trigger consists of four
1439 resistive plate chambers.

1440 2.3.8 Triggers

1441 High energy physics experiments need triggers to select interesting physics. Ex-
1442 periments such as CMS and ATLAS at CERN look for extremely rare events with
1443 up to 40 million events each second. Such amounts can’t be recorded real-time as
1444 many detectors require some time for the readout, up to 1 ms/event in ALICE.
1445 Thus one uses triggers, i.e. a set of very fast hardware based decisions on which
1446 events are to be saved. Additionally one needs some confirmation that an event
1447 has even occurred to tell other detectors that the event needs to be recorded.

1448 For ALICE the target event rates are 1 MHz for pp collisions, 0.1-2 kHz for
1449 Pb–Pb collisions and 200 kHz for the 2013 p–Pb collisions.

1450 At ALICE the main system responsible for the trigger decisions is the AL-
1451 ICE Central Trigger Processor (CTP) [?]. The CTP generates three levels of
1452 hierarchical hardware triggers - Level 0, Level 1 and Level 2, (L0, L1 and L2 re-
1453 spectively) before an event is accepted and transmitted to the Data Acquisition

1454 system (DAQ). Afterwards additional software assessments are performed by the
1455 High Level Trigger (HLT).

1456 Triggers can be roughly put into two classes, minimum bias triggers that make
1457 sure no empty events are recorded, and rare triggers that require specific signatures
1458 in ALICE detectors, such as large energy deposits in EMCal or two muons in the
1459 muon arm acceptance.

1460 Minimum bias trigger

1461 Several of the ALICE detectors are used to make the initial minimum bias trigger
1462 decisions. These include the SPD layers of ITS, V0 and T0. SPD can count the
1463 number of hits in the first two layers of ITS. Minimum bias pp collisions typically
1464 require at least one hit in either SPD or V0A/V0C. Similarly Pb–Pb triggers look
1465 at both V0 and SPD hits. The p–Pb data has been mainly triggered using V0
1466 information.

1467 EMCal trigger

1468 In addition to the minimum bias triggers, the most relevant trigger for this thesis
1469 is the EMCal trigger. Much of the EMCal trigger has been developed at the
1470 University of Jyväskylä. Extensive details of the trigger and the development
1471 work can be found in the thesis of Jiří Král [212]. Personally I have spent time at
1472 CERN helping in the maintenance of the level 0 trigger.

1473 ALICE EMCal provides two levels of trigger signal, L0 and L1, which allows
1474 triggering on either single shower deposits or integrated energy deposits in larger
1475 areas, i.e. jets [213].

1476 As inputs the trigger gets exclusive sets of 2×2 EMCal towers, to limit the
1477 number of channels that need to be processed. The L0 trigger then checks for
1478 energy deposits within a rolling window of 2×2 trigger channels (4×4 towers).
1479 Areas of 4×4 towers most probably will contain only a single shower. (or two
1480 adjacent showers coming from a single decayed π^0) Thus the trigger is called the
1481 single shower trigger.

1482 For L0 the trigger decision is done in Trigger Region Units (TRU) that each
1483 cover 4×42 channels (8×48 towers). The amplitude from the sliding window
1484 is compared to a constant threshold. Additionally a peak finding algorithm is
1485 implemented to define correctly the time of the signal maximum. A single bit OR
1486 decision of all individual TRUs is forwarded to the CTP as the EMCal L0 trigger
1487 decision.

1488 The L0 information is additionally forwarded to the Level 1 trigger, which
1489 recomputes similar 2×2 channel decisions to produce the single shower trigger,
1490 but L1 can perform the calculation also on the borders between trigger units. In

1491 addition the L1 trigger can check for energy deposits inside a larger 16×16 channel
1492 (32×32 towers) window, which is considered to be the jet trigger.

1493 The L1 trigger can compare up to two thresholds for each single shower and
1494 jet trigger. There is a dedicated link in between the V0 detector and EMCAL STU,
1495 which can provide centrality information that is used to compute a dynamical
1496 threshold as a function of the V0 multiplicity.

1497 The trigger subsystem provides both the L0 and L1 decisions to the CTP and
1498 DAQ.

1499 3 Event and track selection

1500 The $\sqrt{s_{\text{NN}}} = 5.02$ TeV p–Pb ($1.3 \cdot 10^8$ events, $\mathcal{L}_{\text{int}} = 62 \text{ nb}^{-1}$) collisions were
1501 recorded in 2013 by the ALICE detector [214]. The details of the performance of
1502 the ALICE detector during LHC Run 1 (2009–2013) are presented in Ref. [215].

1503 3.1 Event selection

1504 This analysis uses both a minimum bias trigger and an EMCal based trigger to
1505 select the analysed events. For the 2013 p–Pb collisions minimum bias events
1506 are required to have signals in both V0A and V0C. The timing difference between
1507 the two stations is also used to reduce the contamination of the data sample from
1508 beam-gas events [215].

1509 EMCal is used to provide the jet trigger used in triggered datasets. EMCal
1510 can be used to trigger on single shower deposits or energy deposits integrated over
1511 a larger area. Latter case is used for jet triggers. The EMCal trigger definition in
1512 the 2013 p–Pb collisions requires an energy deposit of either 10 GeV for the low
1513 threshold trigger or 20 GeV for the high threshold trigger in a 32×32 patch size.

1514 Triggers, V0 and EMCal are discussed in more detail in sections 2.3.6, 2.3.8
1515 and 2.3.5.

1516 3.2 Track reconstruction

1517 The analysis uses charged tracks that are reconstructed with the Inner Tracking
1518 System (ITS) [216] and the Time Projection Chamber (TPC) [217]. These are
1519 discussed in sections 2.3.1 and 2.3.2. A detailed overview of track reconstruction
1520 in ALICE can be found from [215].

1521 The track reconstruction procedure is shown in Fig. 36. The figure shows only
1522 one track, but in reality the reconstruction has to deal with many tracks. The main
1523 reconstruction of tracks starts in TPC. There are 159 tangential pad rows in the
1524 TPC readout chambers. The track reconstruction starts from the outermost layer
1525 and the hits are paired with hits in the next layer inwards, taking into account
1526 a proximity cut. When this track finding procedure hits the innermost pad row
1527 in TPC, this information is used as an initial seed for the track finding in ITS.
1528 Similar procedure of pairing adjacent layers with a proximity cut is repeated in
1529 ITS.

1530 After the reconstruction of tracks in ITS is completed, all the tracks are ex-
1531 trapolated to their point of closest approach to the preliminary interaction vertex.
1532 Then the second track fitting step begins, this time starting from the interaction
1533 point and proceeding outwards. A Kalman filter [218] technique is used to do the
1534 new fit using the hits found in the previous stage. This time the tracks are matched

1535 also to the other detectors in the central barrel beyond TPC. When this step is
1536 complete, a final refit from the outermost TPC pad rows towards the interaction
1537 point is performed. The final track parameters come from this refit.

1538 With the final track parameters the primary vertex can be determined with
1539 better accuracy than with only SPD information. The tracks are extrapolated to
1540 the nominal beam line and a weighted average of the points of closest approach
1541 determines the accurate primary vertex position.

1542 The final step of the track reconstruction is the determination of the secondary
1543 vertices. For this, all the tracks whose distance of closest approach (DCA) to the
1544 primary vertex is larger than a defined minimum value (?? mm in p–Pb) are
1545 selected. For these tracks, points of closest approaches are determined for pairs of
1546 tracks. If the tracks are sufficiently close to each other and show characteristics of
1547 short lived particle decays, these points are identified as secondary vertices.

1548 Combining the information from the ITS and the TPC provides a resolution
1549 ranging from 1 to 10 % for charged particles with momenta from 0.15 to 100 GeV/c.
1550 For tracks without the ITS information, the momentum resolution is comparable
1551 to that of ITS+TPC tracks below transverse momentum $p_T = 10$ GeV/c, but for
1552 higher momenta the resolution reaches 20 % at $p_T = 50$ GeV/c [215, 220].

1553 Track selection

1554 In p–Pb collisions the tracks are selected following the hybrid approach [221]
1555 which ensures a uniform distribution of tracks as a function of azimuthal angle
1556 (φ). The parameters in the approach are summarised in table 3.

1557 The first requirements are on the quality of the track fit in ITS and TPC.
1558 The ITS requirement only removes tracks that are clear outliers. For TPC the
1559 requirement is much more strict. For step 1 it is required that a track has 3 out
1560 of the 6 possible hits in ITS, one of which must be in the SPD. In step 2 this
1561 is replaced by an additional vertex constraint, where the primary vertex itself is
1562 added as a point to the track to improve the momentum resolution.

1563 For the TPC, 70 crossed pad rows out of the maximum 159 is required. This
1564 measures the effective track length inside the TPC. This takes into account the
1565 possibility of having pad rows missing in the middle of the track due to charge in
1566 these clusters being below the threshold for some reason. Additionally it is required
1567 that the ratio between crossed rows and findable clusters is at least 0.8. Findable
1568 clusters are defined as the number of geometrically possible clusters which can be
1569 assigned to a track, taking into account dead zones due to chamber boundaries
1570 and limited η -acceptance. For both steps of the hybrid cut it is required that the
1571 fraction of clusters shared with several tracks is less than 40%.

1572 The remaining cuts are meant to make sure that the measured tracks are really
1573 produced in the primary collision. A track might gain a kink due to a particle

Table 3: Parameters in the hybrid track cut

Track Cut	Step 1	Step 2
$\chi^2 / \text{ITS cluster}$	< 36	< 36
$\chi^2 / \text{ITS cluster}$	< 4	< 4
Hits in ITS	3	0
ITS hit requirements	1 in SPD	No requirement
Vertex constraint	No	Yes
Number of crossed rows in TPC	70	70
TPC crossed rows over findable clusters	> 0.8	> 0.8
Fraction of shared TPC clusters	< 0.4	< 0.4
Kink daughters	Rejected	Rejected
DCA_{xy}	< 3.2 cm	< 3.2 cm
DCA_z	< 2.4 cm	< 2.4 cm
Other		Rejected by step 1

1574 scattering decay. The particle after such a kink, a kink daughter, is rejected in
 1575 the cuts, as it no longer describes the properties of the primary collisions. The
 1576 final cuts are on the distance of closest approach (DCA) of the track to primary
 1577 vertex. To have confidence that the track comes from the primary collision, the
 1578 track must be close enough to the primary vertex. The cuts are different for the
 1579 distance along (DCA_z) and perpendicular to (DCA_{xy}) the beam axis.

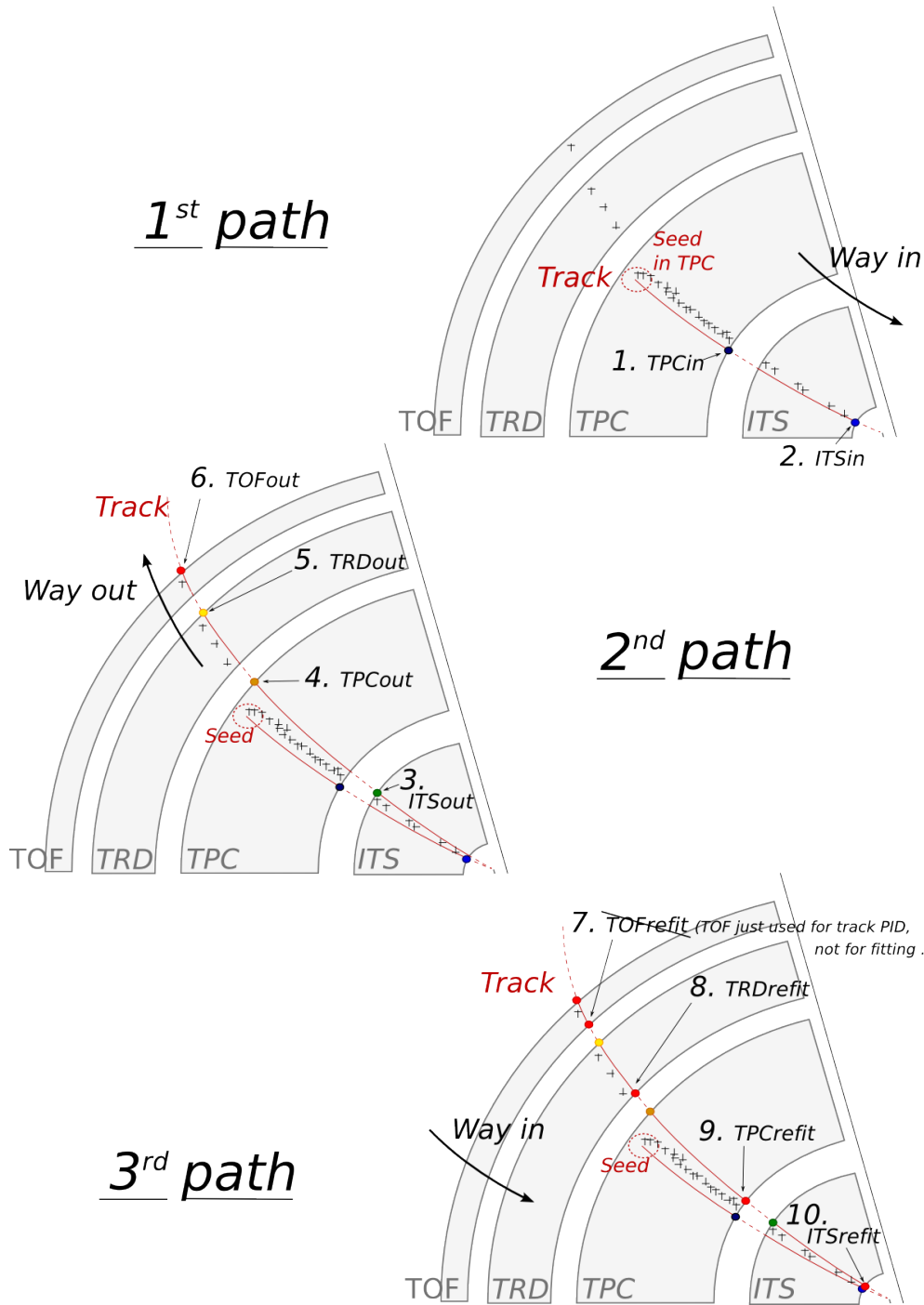


Figure 36: Principles of tracking in the ALICE experiment, showing the three successive paths allowing to build a track and refine its parameters. Numbers ranging from 1 to 10 mention the bits that are activated in case of success during the propagation of the Kalman filter at the considered stage. Figure from [219]

1580 3.3 Cluster selection

1581 Neutral particles used in jet reconstruction are reconstructed by the Electromagnetic
1582 Calorimeter (EMCal) [204]. The EMCal covers an area with a range of
1583 $|\eta| < 0.7$ in pseudorapidity and 100 deg in azimuth. EMCal is complimented with
1584 the Dijet Calorimeter (DCal) [205] and Photon Spectrometer (PHOS) [203] that
1585 are situated opposite of the EMCal in azimuth. PHOS covers 70 degrees in azimuth
1586 and $|\eta| < 0.12$. The DCal is technologically identical to EMCal. The DCal
1587 coverage spans over 67 degrees in azimuth, but in pseudorapidity the mid region
1588 is occupied by the PHOS. In between PHOS and DCal active volumes, there is a
1589 gap of 10 cm. DCal is fully back-to-back with EMCal.

1590 The clusters used in the analysis were obtained from EMCal **by the v2 clusteriser**.
1591 Clusters matched to charged tracks are removed from the analysis as well
1592 as clusters being identified as fake. The parameters used in the clusteriser are
1593 summarised in table 4

1594 The clusteriser searches for a tower with energy deposit greater than a defined
1595 seed energy and merges all surrounding (sharing a side) towers with energy deposit
1596 higher than a defined threshold. In the next step all towers sharing a side with
1597 already included towers are added, again requiring that the energy deposits exceeds
1598 the threshold. The algorithm can identify local minima and halts the clustering
1599 in case that the neighbouring tower energy is higher. Already clustered towers are
1600 removed from the pool, so one tower can only be clustered once.

1601 Highly energetic calorimeter hits should spread into several towers as the elec-
1602 tromagnetic shower evolves. However, some clusters with high energy have their
1603 energy located in a single tower. These are believed to come from a slow neutron
1604 hitting the APD readout of the towers. These are called exotic clusters. The
1605 measure of exoticity is denoted as

$$1 - \frac{E_{\text{cross}}}{E_{\text{max}}}, \quad (48)$$

1606 where E_{max} is the energy in the most energetic tower and E_{cross} is the sum of the
1607 four towers neighbouring the most energetic one. The closer this is to 1, the more
1608 exotic the cluster is and the larger the probability that it is fake. Cut of 0.97 has
1609 been adopted as default for analyses using EMCal, including the one presented in
1610 this thesis. Any clusters above this cut are removed.

1611 A method of matching the cluster position to TPC track extrapolation is used
1612 to suppress charged hadron contribution to hits in EMCal. Tracks identified by the
1613 tracking detectors are extrapolated close to the EMCal surface, where the closest
1614 cluster is found and the track extrapolation is continued until reaching the same
1615 depth as the cluster. The remaining distance in between the extrapolated track
1616 and the cluster is then used to reject hadronic hits.

Table 4: Parameters used in the EMCal clusteriser

Setting	Value
Clusteriser seed	0.2 MeV
Clusteriser cutoff	0.05 MeV
Cells in cluster	> 1
Track matching radius	0.025
Fiducial cut	1 tower
Exotic cut	0.97
Minimal cluster Energy	0.3 GeV

1617 4 Analysis method

1618 4.1 Jet Finding

1619 The analysis uses reconstructed jets as estimates of the original parton. Jet recon-
1620 struction essentially combines nearby tracks into jets.

1621 Collisions between hadrons are never as clean as electron-electron collisions.
1622 Even for a proton-proton collision there are participant partons, that will produce
1623 a soft background in addition to the hard scattering products. Jet reconstruction
1624 must deal with this soft background. The reconstruction is never perfect, one can
1625 have uncorrelated tracks that get included in the jet and some tracks originating
1626 from the parton are missed by the reconstruction. There are several methods to
1627 perform the reconstruction, all of which require some kind of size parameter, which
1628 cuts out jet participants too far from the jet axis. The tracks that are grouped
1629 into a jet are referred to as jet constituents.

1630 In each collision event, the jets are reconstructed using FastJet [222] with the
1631 anti- k_T algorithm [223]. Jets for $R=0.4$ are selected in $|\eta| < 0.25$ to satisfy the
1632 fiducial acceptance of the EMCAL. In jet reconstruction both charged tracks with
1633 $p_T > 0.15 \text{ GeV}/c$ and neutral clusters with $p_T > 0.30 \text{ GeV}/c$ are considered. The
1634 analysis is then performed by analysing the charged jet constituents and results
1635 are presented in terms of the jet transverse momentum $p_{T\text{jet}}$.

1636 4.1.1 Anti k_T algorithm

1637 Jets are reconstructed using the anti- k_T algorithm [223]. The algorithm works by
1638 trying to undo the splittings through combining protojets. First the algorithm
1639 creates a list of protojets. At the beginning the list is populated by converting
1640 each track in the event into a protojet. Then the algorithm proceeds by combining
1641 these protojets. A simplified picture of the process for a limited number of tracks
1642 is shown in Fig. 37

1643 The algorithm calculates distance measures for each individual protojet and
1644 for each possible pair of protojets. For individual protojets this depends only on
1645 the transverse momentum of the track.

$$k_{Ti}^2 = p_{Ti}^{2p} \quad (49)$$

1646 For each pair of protojets the distance measure is calculated as

$$k_{Ti,j}^2 = \min(p_{Ti}^{2p}, p_{Tj}^{2p}) \frac{\Delta R_{i,j}^2}{D^2}, \quad (50)$$

1647 where

$$R_{i,j} = (\phi_i - \phi_j)^2 + (y_i - y_j)^2. \quad (51)$$

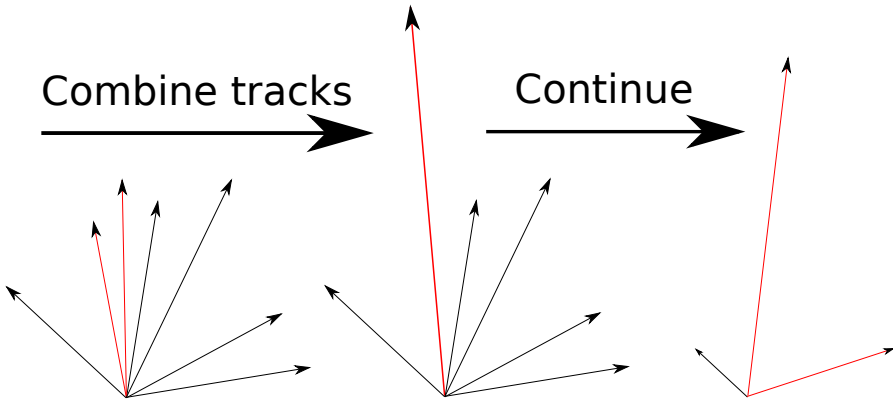


Figure 37: A simple example of the antil- k_T algorithm in progress. The red tracks in the leftmost figure are identified to have the smallest $k_{T,i}$ in the event and are combined into the red track of the middle figure. As this continues the remaining tracks are added to this or other jets. One track was deemed to be isolated enough to be counted as a protojet by itself. Note that the rightmost figure is zoomed out.

1648 If k_{Ti} is the smallest quantity then the protojet is a jet and it is removed from
1649 further consideration. If $k_{Ti,j}$ is the smallest quantity the two protojets i and j are
1650 merged. This is repeated until no protojets are left.

1651 The choice of the power p in the distance measure depends on the algorithm
1652 used

- 1653 • $p = 1$: k_T algorithm
- 1654 • $p = 0$: Cambridge Aachen algorithm
- 1655 • $p = -1$: anti- k_T algorithm

1656 With the choice $p = -1$ in anti- k_T algorithm, the softest splittings are un-
1657 done first. One consequence of the power choice in the anti- k_T algorithm is that
1658 reconstructed jets have a shape close to circular.

1659 4.2 Definition of j_T

1660 The jet fragmentation transverse momentum, \vec{j}_T , is defined as the component of
1661 the constituent particle momentum, \vec{p}_a , transverse to the jet momentum, \vec{p}_{jet} . The
1662 resulting \vec{j}_T is illustrated in Fig. 38. The length of the \vec{j}_T vector is

$$j_T = \frac{|\vec{p}_{jet} \times \vec{p}_{track}|}{|\vec{p}_{jet}|}. \quad (52)$$

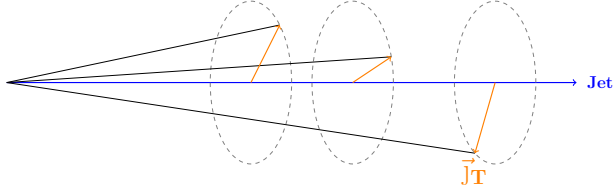


Figure 38: Illustration of \vec{j}_T . The jet fragmentation transverse momentum, \vec{j}_T , is defined as the transverse momentum component of the track momentum, \vec{p}_{track} , with respect to the jet momentum, \vec{p}_{jet} .

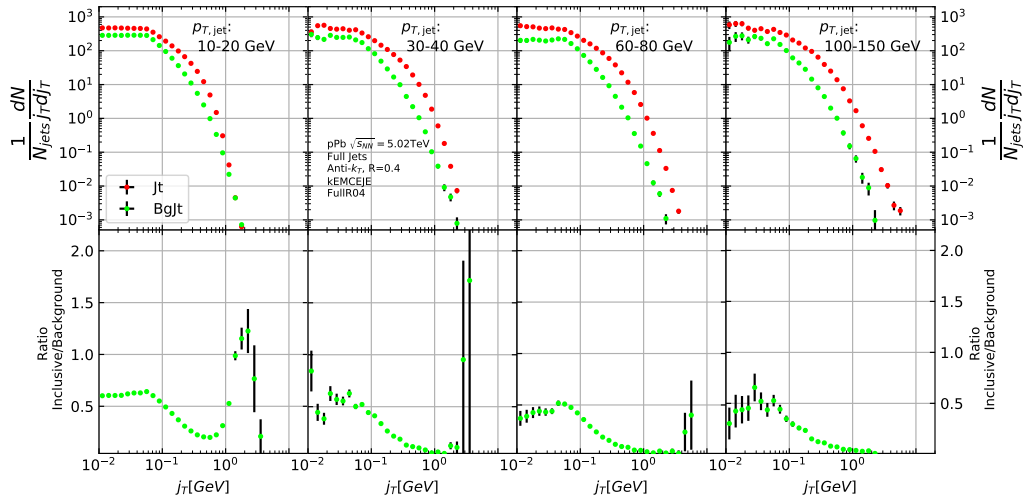


Figure 39: Inclusive j_T with background

1663 It is commonly interpreted as a transverse kick with respect to the initial hard
 1664 parton momentum that is given to a fragmenting particle during the fragmentation
 1665 process, which is a measure of the momentum spread of the jet fragments [?].

1666 The reconstructed jet axis is used for j_T reference. Any charged track within
 1667 a fixed cone with radius R is taken as a jet constituent, as opposed to using the
 1668 constituent list provided by the jet algorithm. Anti- k_T produces jets that are
 1669 very circular in shape. Thus this doesn't change the constituent list considerably.
 1670 Neutral tracks are used only in jet reconstruction.

1671 Results of the raw inclusive j_T distribution in four $p_{\text{T,jet}}$ bins with background
 1672 are shown in figure 39. Background is further discussed in Sec. 4.4

1673 Resulting j_T distributions are shown as

$$\frac{1}{j_T} \frac{dN}{dj_T} \quad (53)$$

1674 distributions. The logic behind this is that j_T is inherently a two-dimensional
1675 observable, comprised of j_{Tx} and j_{Ty} components. So the actual physical observable
1676 would be

$$\frac{d^2N}{dj_{Tx} dj_{Ty}} \quad (54)$$

1677 Changing into polar coordinates with $j_{Tr} = j_T$ and θ gives

$$\frac{d^2N}{j_T dj_T d\theta}, \quad (55)$$

1678 where j_T over the azimuth θ should stay constant and it can be integrated over,
1679 which gives

$$\frac{1}{2\pi} \frac{dN}{j_T dj_T}. \quad (56)$$

1680 4.3 Unfolding detector effects

1681 The raw inclusive j_T distributions are corrected for the detector inefficiency with
1682 an unfolding procedure. The procedure uses response matrices obtained from a
1683 PYTHIA [224] simulation.

1684 Measured distributions are affected by two main factors; Limited acceptance -
1685 The probability to observe a given event is less than one and limited resolution -
1686 Quantity x cannot be determined exactly, but there is a measurement error. True
1687 $f(x)$ and measured $g(y)$ distributions are connected by a convolution integral.
1688 Including statistical fluctuations this becomes

$$\hat{g}(y) = \int_a^b A(y, x) f(x) dx + \epsilon(y), \quad (57)$$

1689 where A is the detector response obtained by (for example) Monte Carlo simula-
1690 tions and $\epsilon(y)$ is the term coming from statistical fluctuations. If x and y are
1691 discrete variables we have

$$\hat{g}_i = \sum_{j=1}^m A_{ij} f_j + \epsilon_i, \quad (58)$$

1692 where i and j give the j_T bins in the true and measured distributions. f_j and
1693 g_i give the counts in these bins. Or in matrix form

$$\hat{g} = Af + \epsilon, \quad (59)$$

1694 where \hat{g} and f are vectors corresponding to the measured and true histograms. If
 1695 the only detector effect is limited acceptance, A is a diagonal matrix, i.e. $A_{ij} =$
 1696 0 for $i \neq j$. We want to deduce the true distribution f , when the measured
 1697 distribution g is known. In a general discrete case the (naive) solution is obtained
 1698 by the inverse matrix

$$\hat{f} = A^{-1}\hat{g} \quad (60)$$

1699 However this usually leads to oscillating solutions and determining the inverse
 1700 matrix can be difficult.

1701 Two common methods to perform this inversion are Bayesian and SVD unfold-
 1702 ing methods. Often the solution requires some additional *a priori* information.
 1703 For example the solution should be smooth in most cases.

1704 4.3.1 Bayesian unfolding

1705 The bayesian (iterative) method is based on the Bayes formula [?].

$$P(C_i|E_j) = \frac{P(E_j|C_i) P_0(C_i)}{\sum_{l=1}^{n_C} P(E_j|C_l) P_0(C_l)}, \quad (61)$$

1706 i.e. the probability of Cause C_i ("truth") given Effect E_j ("observed") is propor-
 1707 tional to the probability of observing E_j given C_i , $P(E_j|C_i)$ (response matrix) and
 1708 the true distribution $P_0(C_i)$.

1709 In the unfolding procedure P_0 is given some starting distribution, either a
 1710 uniform distribution or some guess of the final distribution. Taking into account
 1711 the inefficiency this gives

$$\hat{n}(C_i) = \frac{1}{\epsilon_i} \sum_{j=1}^{n_E} n(E_j) P(C_i|E_j), \quad (62)$$

1712 where

$$P(C_i|E_j) = \frac{P(E_j|C_i) P_0(C_i)}{\sum_{l=1}^{n_C} P(E_j|C_l) P_0(C_l)}, \quad (63)$$

1713 and

$$\hat{n}(C_i) = \frac{1}{\epsilon_i} \sum_{j=1}^{n_E} n(E_j) P(C_i|E_j). \quad (64)$$

1714

1715 First $P(C_i|E_j)$ is calculated with the uniform distribution or best guess of
 1716 the shape of the distribution. This is then used to calculate the new distribution
 1717 $\hat{P}(C_i)$

$$\hat{N}_{true} = \sum_{i=1}^{n_C} \hat{n}(C_i), \quad \hat{P}(C_i) = P(C_i|n(E)) = \frac{\hat{n}(C_i)}{\hat{N}_{true}} \quad (65)$$

1718 P_0 is then replaced with \hat{P} and the procedure is repeated until an acceptable
1719 solution is found.

1720 The bayesian procedure alongside with the SVD unfolding method are imple-
1721 mented in the RooUnfold package [225], which is used to perform the unfolding in
1722 practice. In RooUnfold the number of iterations is given beforehand. In practice
1723 this requires some trial and error. The number of iterations should be as low as
1724 possible, as the errors increase when going further in the iterations, but the number
1725 of iterations must be high enough so that the correct distribution is extracted.

1726 Error propagation in the Bayesian procedure

1727 The measured distribution has some statistical uncertainty, this should be reflected
1728 in the unfolded distribution. Additionally the response matrix may have some
1729 uncertainty if the statistics used in the Monte Carlo simulation were limited.

1730 For errors originating from the measured distribution RooUnfold uses the error
1731 propagation matrix

$$\frac{\partial \hat{n}(C_i)}{\partial n(E_j)} = M_{ij} + \frac{\hat{n}(C_i)}{n_0(C_i)} \frac{\partial n_0(C_i)}{\partial n(E_j)} - \sum_{k=1}^{n_E} \sum_{l=1}^{n_C} \frac{n(E_k) \epsilon_l}{n_0(C_l)} M_{ik} M_{lk} \frac{\partial n_0(C_l)}{\partial n(E_j)}, \quad (66)$$

1732 where $\hat{n}(C_i)$ is the unfolded result from Eq. 64. This depends upon the matrix
1733 $\frac{\partial n_0(C_i)}{\partial n(E_j)}$, which is $\frac{\partial \hat{n}(C_i)}{\partial n(E_j)}$ from the previous iteration. In the first iteration, $\frac{\partial n_0(C_i)}{\partial n(E_j)} = 0$
1734 and $\frac{\partial \hat{n}(C_i)}{\partial n(E_j)} = M_{ij}$.

1735 The error propagation matrix V is used to obtain the covariance matrix on the
1736 unfolded distribution

$$V(\hat{n}(C_k), \hat{n}(C_l)) = \sum_{i,j=1}^{n_E} \frac{\partial \hat{n}(C_k)}{\partial n(E_i)} V(\hat{n}(E_i), \hat{n}(E_j)) \frac{\partial \hat{n}(C_l)}{\partial n(E_j)}, \quad (67)$$

1737 where $V(\hat{n}(E_i), \hat{n}(E_j))$ is the covariance matrix of the measurements. In count-
1738 ing experiments common in particle physics, each bin is independently Poisson
1739 distributed, with

$$V(\hat{n}(E_i), \hat{n}(E_j)) = n(E_i) \delta_{ij} \quad (68)$$

1740 The error propagation matrix for the response matrix is

$$\frac{\partial \hat{n}(C_i)}{\partial P(E_j|C_k)} = \frac{1}{\epsilon_i} \left(\frac{n_0(C_i) n(E_j)}{f_j} - \hat{n}(C_i) \right) \delta_{ik} - \frac{n_0(C_k) n(E_j)}{f_j} M_{ij} + \\ \frac{\hat{n}(C_i)}{n_0(C_i)} \frac{\partial n_0(C_i)}{\partial P(E_j|C_k)} - \frac{\epsilon_i}{n_0(C_i)} \sum_{l=1}^{n_E} \sum_{r=1}^{n_C} n(E_l) M_{il} M_{rl} \frac{\partial n_0(C_r)}{\partial P(E_j|C_k)}, \quad (69)$$

where $\frac{\partial n_0(C_i)}{\partial P(E_j|C_k)}$ is the error propagation matrix from the previous iteration, $\frac{\hat{n}(C_i)}{\partial P(E_j|C_k)}$. For the first iteration, this is zero and the final two terms in Eq. 69 disappear.

The covariance matrix due to these errors is given by

$$V(\hat{n}(C_k), \hat{n}(C_l)) = \sum_{j,s=1}^{n_E} \sum_{i,r=1}^{n_C} \frac{\partial \hat{n}(C_k)}{\partial P(E_j|C_i)} V(P(E_j|C_i), P(E_s|C_r)) \frac{\partial \hat{n}(C_l)}{\partial P(E_s|C_r)}, \quad (70)$$

where $V(P(E_j|C_i), P(E_s|C_r))$ can be taken as multinomial, Poisson or other distribution.

4.3.2 Toy Monte Carlo

remove / move to appendix? A toy Monte Carlo simulation was performed to see the performance of unfolding in an ideal case. The simulations samples jet p_T values from the observed p_T distribution. Starting from this p_T the simulations starts creating tracks with

$$p_{\text{track}} = z_{\text{track}} p_{T\text{jet}} \quad (71)$$

where z_{track} is sampled from the observed z distribution. All tracks below 0.15 GeV are discarded. Sampling is continued until the sum of the track transverse momenta exceeds the jet transverse momentum. Jet is then defined as the sum of the track momenta.

Simultaneously a p_T dependant observation efficiency is applied to the tracks and a separate observed jet is calculated using only the observed tracks. Additionally a set of fake tracks is added to the observed jet. Tracks are always either observed or not at the true momentum. No smearing is added to the observed momentum.

Afterwards the tracks are looped over for j_T calculation. For observed tracks we calculate j_T with respect to both the true jet axis and the observed jet. 2D Response matrix is filled with

$$(j_T^{\text{obs}}, p_{T\text{jet}}^{\text{obs}}, j_T^{\text{true}}, p_{T\text{jet}}^{\text{true}}) \quad (72)$$

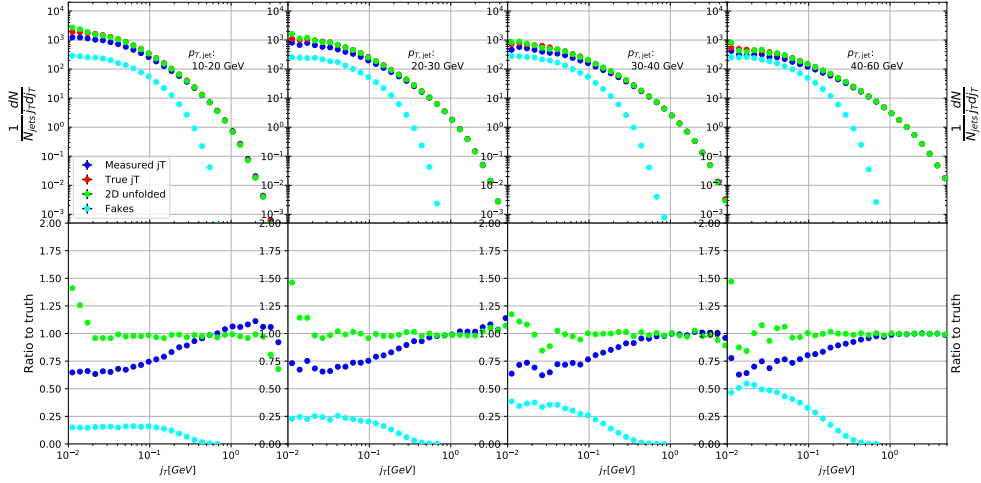


Figure 40: Results from unfolding in Toy Monte Carlo

1764 In practice this is done with a set of 3D histograms, where $p_{T\text{jet},\text{true}}$ determines
 1765 the histogram index and the remaining three values the bin in the 3D histogram.

1766 After creating the response matrices, an identical procedure is carried out to
 1767 the create testing data. Now instead of filling response matrices, 2D histograms
 1768 are filled with $(j_T^{\text{obs}}, p_{T\text{jet}}^{\text{obs}})$ and $(j_T^{\text{true}}, p_{T\text{jet}}^{\text{true}})$

1769 The observed distributions are unfolded using RooUnfold's 2D Bayesian (iter-
 1770 ative) algorithm. Results are shown in figure 40. Aside from some discrepancy at
 1771 very low j_T the true distribution is retrieved well.

1772 4.3.3 Pythia Response matrices

1773 A PYTHIA6 simulation was carried out to determine the response matrices. [Details](#)
 1774 of the simulation

1775 Response matrices are filled through correlation between MC detector and
 1776 particle level jets and tracks.

1777 The ranges of both j_T and $p_{T\text{jet}}$ extend the ranges in end results. These are
 1778 shown in Tab. 5. The ranges are the same in detector and particle level.

1779 When calculating j_T for MC particles the code checks whether a corresponding
 1780 detector level track exists and if that track had a j_T value. Additionally the code
 1781 checks for detector level tracks that don't have corresponding particle level track
 1782 with a j_T value.

1783 There are several possibilities that have to be taken into account:

- 1784 • We find a corresponding track with a j_T value, response matrix is filled
 1785 normally with $(j_T^{\text{obs}}, p_{T\text{jet}}^{\text{obs}}, j_T^{\text{true}}, p_{T\text{jet}}^{\text{true}})$

Table 5: j_T and p_T ranges used in unfolding. The same ranges are used for detector and truth level.

	j_T	$p_{T\text{jet}}$
Min	0.01	5
Max	20	500

- We don't find a corresponding track. Record $(j_T^{\text{true}}, p_{T\text{jet}}^{\text{true}})$ as a miss
- We find a corresponding track, but it didn't have j_T value. Most likely because it was not part of a jet in the detector level set. Similary record $(j_T^{\text{true}}, p_{T\text{jet}}^{\text{true}})$ as a miss
- For detector level tracks that have no correspondence in particle level set the code records $(j_T^{\text{obs}}, p_{T\text{jet}}^{\text{obs}})$ as a fake

In the analysis code the response matrix is made of an array of 3 dimensional histograms, with $(j_T^{\text{obs}}, p_{T\text{jet}}^{\text{obs}}, j_T^{\text{true}})$ as axes. The histogram index gives the $p_{T\text{jet}}^{\text{true}}$ value.

4.3.4 Unfolding algorithm

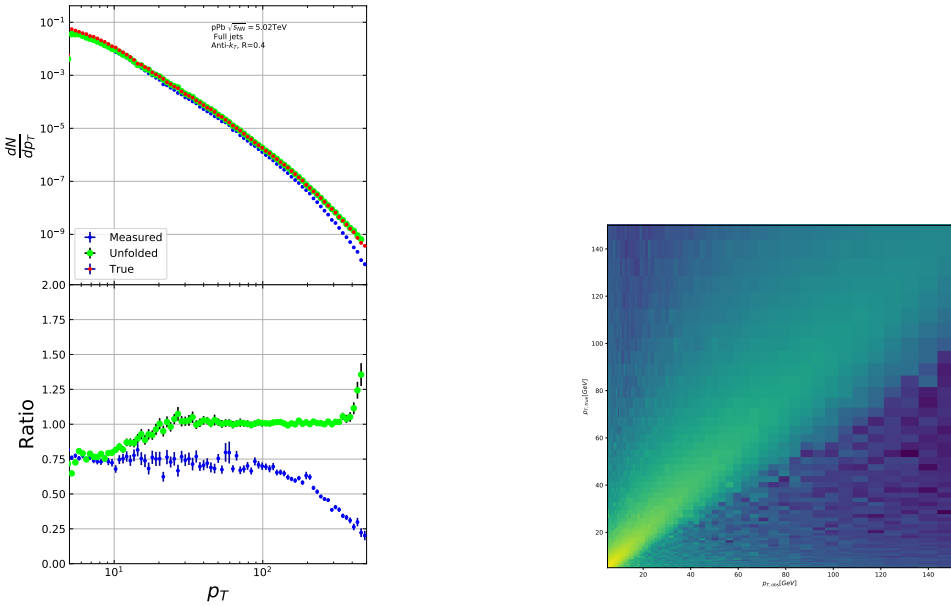
As a primary method unfolding is performed with an iterative (bayesian) algorithm using the RooUnfold [225] package. The number of iterations used is 4. The default ranges of j_T and $p_{T\text{jet}}$ are shown in 5. As a default the true j_T distribution from the PYTHIA simulation is used as the prior.

4.3.5 Unfolding closure test

The PYTHIAset is divided into 2 halves. First is used to fill the response matrices, as well as record missed and fake tracks. Second half is used to test the effectiveness of the unfolding method. Jet p_T distributions are shown in figure 41a and response matrix are shown in figure 41b.

Response matrices within single jet p_T bins are shown in figure 42. Results from the closure test are shown in figure 43. In the lowest jet p_T bins unfolding fails to recover the true distribution. The lowest jet p_T bins are dominated by combinatorial jets and thus the true detector response is likely not retrieved.

Above $30 \text{ GeV} < p_{T\text{jet}} < 40 \text{ GeV}$ the distribution is recovered well in the mid j_T region. At $j_T < 0.1 \text{ GeV}$ there is clear discrepancy. The final results are shown only for $j_T > 0.1 \text{ GeV}$. Additionally there is some discrepancy at very high j_T . This is taken into account in the unfolding systematics. (TODO: Show this)



(a) Unfolded jet p_T distribution in PYTHIA closure test
(b) Jet p_T response matrix from unfolding closure test

Figure 41: Jet p_T in unfolding closure test

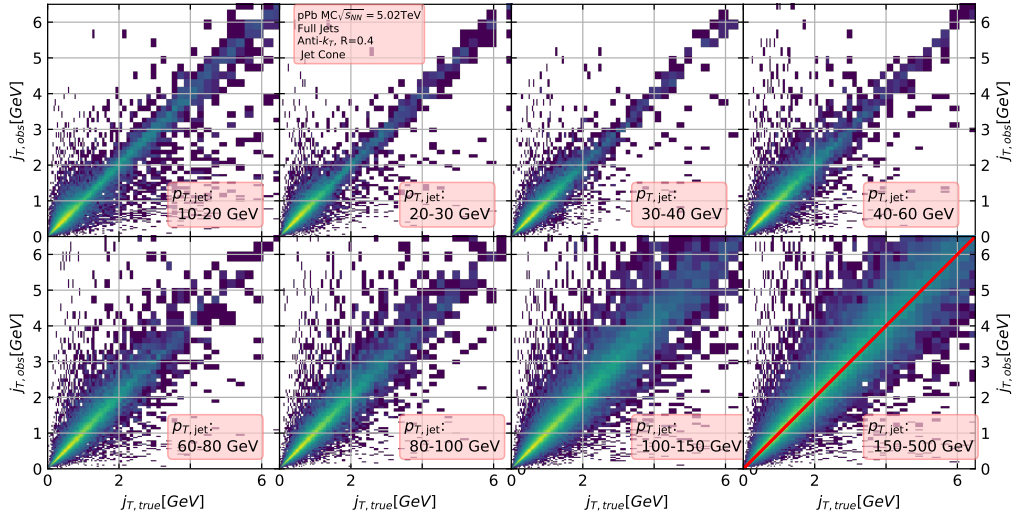


Figure 42: j_T Response matrices in individual $p_{T,jet}$ bins

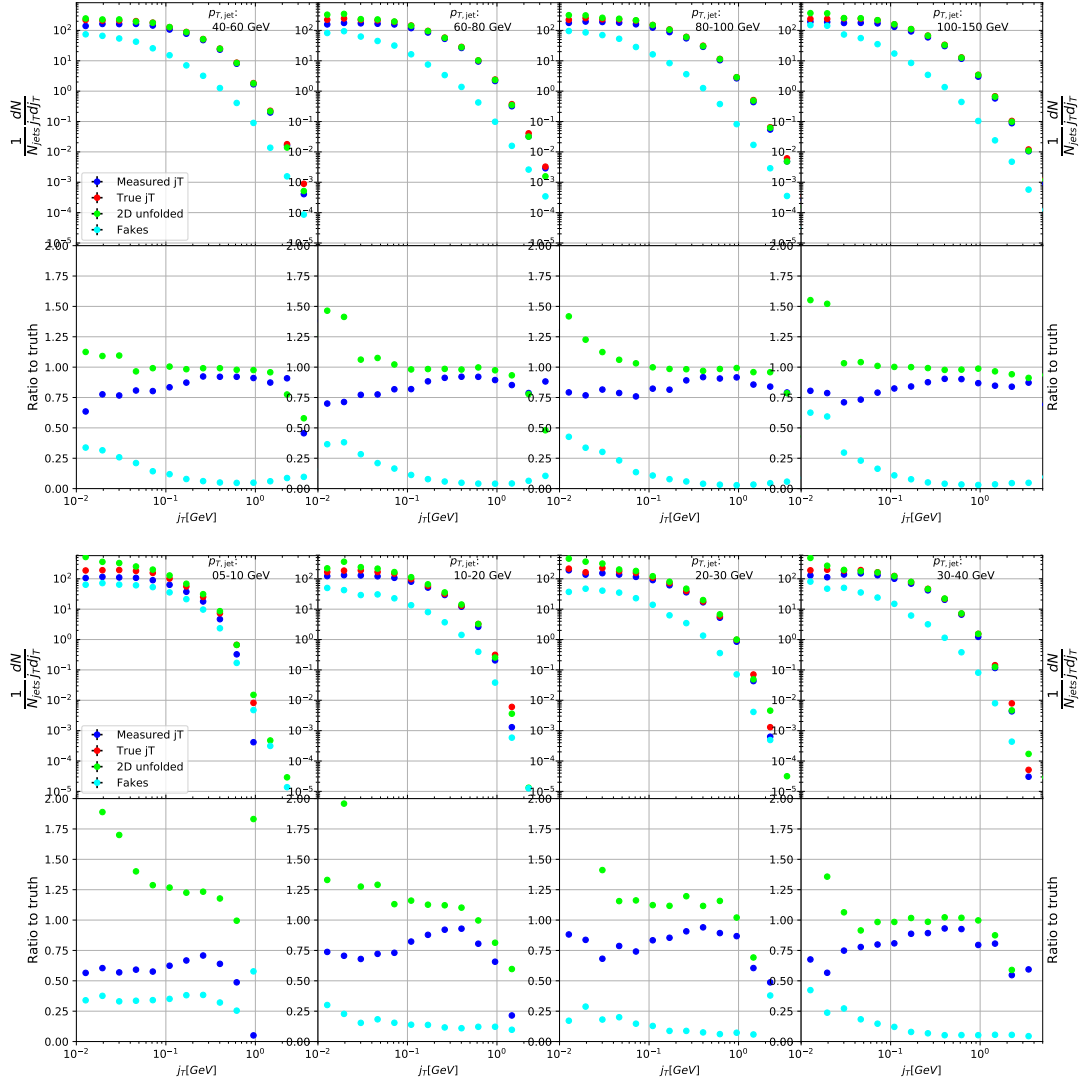


Figure 43: Pythia closure test results. Fake tracks include also tracks that do exist in the true dataset, but for one reason or another were not given j_T values. j_T is only calculated for tracks that are associated with jets

1813 4.4 Background

1814 When calculating j_T distributions for jet constituents there is a contribution from
 1815 the underlying event (UE), i.e. tracks that just happen to be close to the jet axis.
 1816 To find the signal coming from the actual jet we need to subtract the background
 1817 (UE) contribution. On a jet-by-jet basis this is impossible, so one must estimate
 1818 the background contribution in the inclusive distribution. A schematic view of the
 1819 background contribution is shown in Fig. 44.

1820 We have two methods for background estimation. In the first we look at the
 1821 direction perpendicular to the jet. This is assumed to be the region least likely to
 1822 contain jet contributions. In the second method we randomly assign the tracks of
 1823 event new ϕ and η values. The result is thus guaranteed to be uncorrelated.

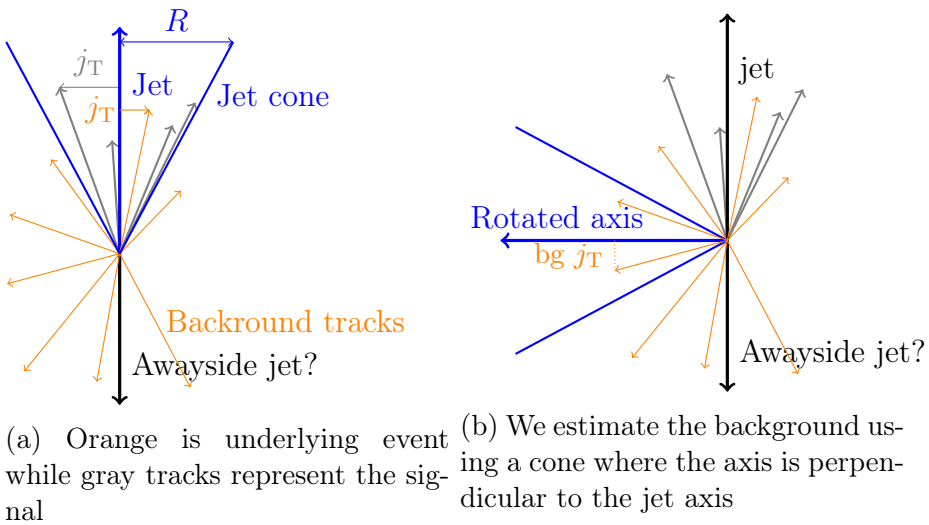


Figure 44: Background estimation

1824 4.4.1 Perpendicular cone background

1825 As a primary method to estimate the background we look at regions of the detector
 1826 where there are no tracks from jets, but only uncorrelated tracks from the under-
 1827 lying event. The underlying event is thus estimated by looking at an imaginary
 1828 jet cone perpendicular to the observed jet axis ($\frac{\pi}{2}$ Rotation in ϕ).

1829 After calculating the j_T values for tracks in the jet, we rotate the jet axis by $\frac{\pi}{2}$
 1830 in positive ϕ direction. We check that there are no other jets closer than $2R$ to the
 1831 rotated axis. Otherwise background calculation is skipped for this jet. Probability
 1832 of this happening is 1-2% depending on the jet p_T bin.

1833 If we don't find other jets in the vicinity we move on to estimate the background.
 1834 We find all tracks within a cone of radius R around the rotated axis and calculate
 1835 j_T of these tracks with respect to the rotated axis. Auto-correlations are discussed
 1836 in Sec. 4.4.3.

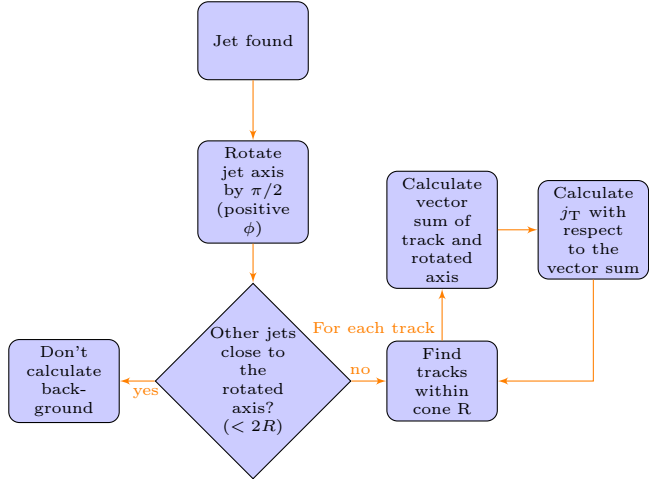


Figure 45: Flowchart representation of the perpendicular cone background procedure

1837 4.4.2 Random background

1838 In the random background method we look at all tracks in the event, except for
 1839 tracks close to jets found by the jet algorithm. We randomly assign new η and ϕ
 1840 values to all tracks using uniform distributions with $|\eta| < 1.0$. p_T values are kept
 1841 the same. To increase statistics there is a possibility to create a number of random
 1842 tracks for each actual track. In the analysis we do this 10 times for each track.
 1843 Again the track p_T value is kept the same.

1844 We create a random jet cone from uniform η and ϕ distributions. Here $|\eta| <$
 1845 0.25. Now we calculate j_T of the random tracks with respect to the random cone
 1846 axis. Auto-correlations are added before calculating j_T (see 4.4.3).

1847 4.4.3 Auto-correlations

1848 Jet axis is simply a vector sum of all its constituents. Thus having an additional
 1849 track in the jet from the underlying event moves the jet axis towards this track.
 1850 Since the axis is now closer to the track, it has a smaller j_T value. Assuming a
 1851 1 GeV background track at the edge of a $R = 0.4$ cone the j_T value would be
 1852 0.4 GeV. If this is added to a 5 GeV jet, the j_T value becomes 0.33 GeV after the

jet axis moves. In a 50 GeV jet it would be 0.39 GeV. This is a region where the inclusive j_T distribution is dominated by background. The distribution is also steeply falling. Overestimating the background can lead to a situation where the background estimation exceeds the inclusive distribution.

To take this effect into account we can't use a fixed axis for background, but it has to behave like a jet would when additional tracks are added. Thus before calculating j_T values we make a vector sum of the track and the axis used for background, which is either the perpendicular cone axis or the random axis depending on the background method. In each case the momentum of this background axis is assumed to be the same as the jet which initiated the background estimation.

In pPb data there is on average about one underlying event track in a $R = 0.4$ cone. If there would be more, one should consider taking the vector sum of all tracks inside the cone. As there is usually only one track and if there are more it's unlikely that more than one has high momentum, taking the vector sum track-by-track should be enough.

4.4.4 Comparing background methods

Comparison between perpendicular cone and random background in figure 46. The advantage of the random background method is the added amount of statistics as the procedure can be repeated several times for each event. However, it seems that, especially in the highest $p_{T\text{jet}}$ bins there is some jet contribution left at the high end. Naturally there is no correlation between the tracks and the background axis, but if some high momentum tracks originating from jets were not subtracted and happen to hit the edge of the background cone, they can increase the high j_T yield in the background estimation.

One should note that the results from perpendicular cone background show no observable change between $p_{T\text{jet}}$ bins. It is a good indication that the background is actually dominated by the underlying event over the entire j_T region.

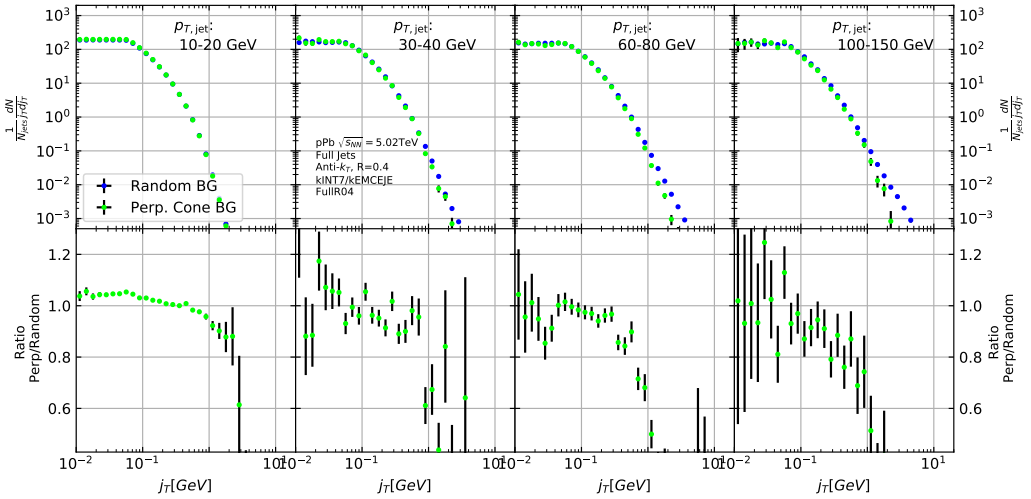


Figure 46: j_T background with two different methods

1880 4.5 Fitting

1881 After unfolding and background subtraction the resulting signal distributions are
 1882 fitted with a 2 component function shown in Eq. 73. Gaussian distribution is used
 1883 for low j_T and an inverse gamma function is used for high j_T . The Gaussian is
 1884 taken to have the center at $j_T = 0$. In total this gives 5 parameters. The fitting
 1885 procedure was inspired by the dihadron j_T analysis by ALICE [226]. The complete
 1886 fitting function is

$$\frac{1}{N_{\text{jets}} j_T d j_T} \frac{dN}{d j_T} = \frac{B_2}{B_1 \sqrt{2\pi}} e^{-\frac{j_T^2}{2B_1^2}} + \frac{B_3 B_5^{B_4}}{\Gamma(B_4)} e^{-\frac{B_5}{j_T}}. \quad (73)$$

1887 To achieve stable results the fitting is performed in two steps. First both
 1888 components are fitted separately. Gaussian component is fitted to the low end of
 1889 j_T . Inverse gamma component is fitted to j_T above 1 GeV/c. After getting the
 1890 results from the individual fits they are combined into a single function with initial
 1891 values from the individual results and an additional fit is performed.

1892 After getting the fit function $\sqrt{\langle j_T^2 \rangle}$ (RMS) and yield values are extracted
 1893 separately from each component. The narrow component RMS is

$$\sqrt{\langle j_T^2 \rangle} = \sqrt{2} B_1, \quad (74)$$

1894 and the wide component RMS value is calculated as

$$\sqrt{\langle j_T^2 \rangle} = \frac{B_5}{\sqrt{(B_4 - 2)(B_4 - 3)}}, \quad (75)$$

₁₈₉₅ where it is required that $B_4 > 3$.

₁₈₉₆ The statistical errors can be calculated with the general error propagation
₁₈₉₇ formulas. As a result one gets errors for the narrow component RMS

$$\delta \sqrt{\langle j_T^2 \rangle} = \sqrt{2} \delta B_1 \quad (76)$$

₁₈₉₈ and for the wide component RMS

$$\delta \sqrt{\langle j_T^2 \rangle} = \sqrt{\left(\frac{(5 - 2B_4) B_5 \delta B_4}{(2(B_4 - 2)(B_4 - 3))^{\frac{3}{2}}} \right)^2 + \left(\frac{\delta B_5}{\sqrt{(B_4 - 2)(B_4 - 3)}} \right)^2} \quad (77)$$

1899 5 Systematic errors

1900 **Extend Systematics** The main systematic uncertainties in this analysis come from
1901 the background estimation, the unfolding procedure and uncertainty in the track-
1902 ing efficiency.

1903 The systematics in background estimation were studied using an alternative
1904 method to extract the background, the random background method.

1905 The systematic uncertainty that arises from the unfolding procedure is esti-
1906 mated by performing the unfolding with two separate methods. Data corrected
1907 by the iterative unfolding method are used as the results and the SVD unfolding
1908 method is employed to estimate the uncertainty. In a PYTHIA closure test the
1909 true distribution was in general found to be between the unfolded distributions
1910 from the iterative and SVD method. The difference between the methods when
1911 unfolding data should give a reasonable estimate of the unfolding uncertainty. The
1912 resulting uncertainty is below 8% for both wide and narrow component RMS.

1913 5.1 Background

1914 The uncertainty coming from background estimation is estimated by subtracting
1915 the background separately for the perpendicular cone and random background
1916 methods. Comparisons of the resulting signal distributions are shown in Fig. 47.

1917 Fits are then performed on both perpendicular cone and random background
1918 signals. Difference between them is taken as the systematic error. The fits for
1919 individual bins from the random background method are shown in figure 48. Re-
1920 sulting differences between the methods for different components are shown in
1921 figure 49. The dotted lines are put at $\pm 5\%$ for the narrow component and at
1922 $\pm 8\%$ for the wide component. These are taken as systematic estimates for the
1923 entire $p_{T\text{jet}}$ range.

1924 5.2 Unfolding

1925 Unfolding is the second major source of systematic uncertainty. To estimate the
1926 uncertainty related to the unfolding procedure several checks are performed. The
1927 main systematic uncertainty estimation comes from comparing results performed
1928 using both SVD and Bayesian unfolding. Difference between the methods is taken
1929 as the systematic error. Since SVD unfolding does not have a 2 dimensional
1930 options, the unfolding is done bin by bin. The resulting distributions after SVD
1931 unfolding and background subtraction with the perpendicular cone method are
1932 shown in fig 50.

1933 As in the background systematic estimation, fits are performed for both cases
1934 separately. Resulting differences between the methods for different components

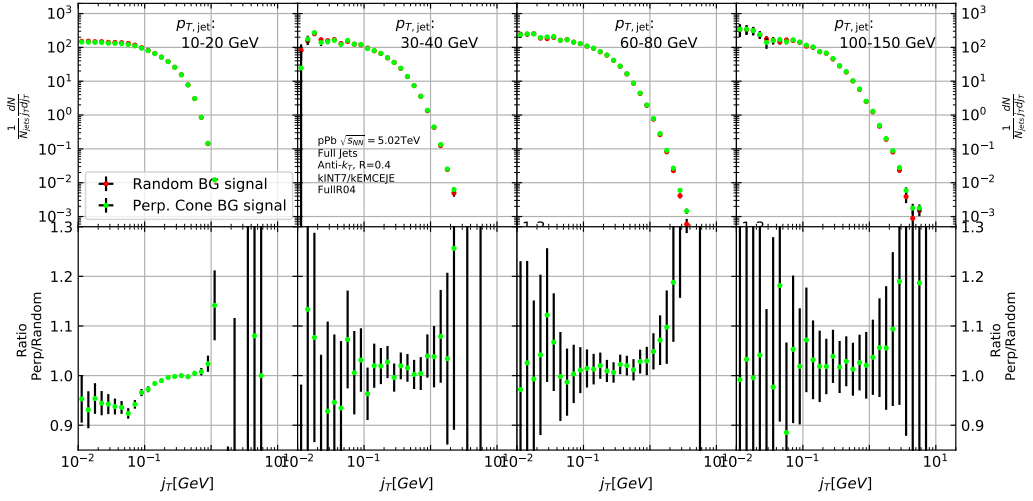


Figure 47: Comparison of the effect of background method on j_T signal.

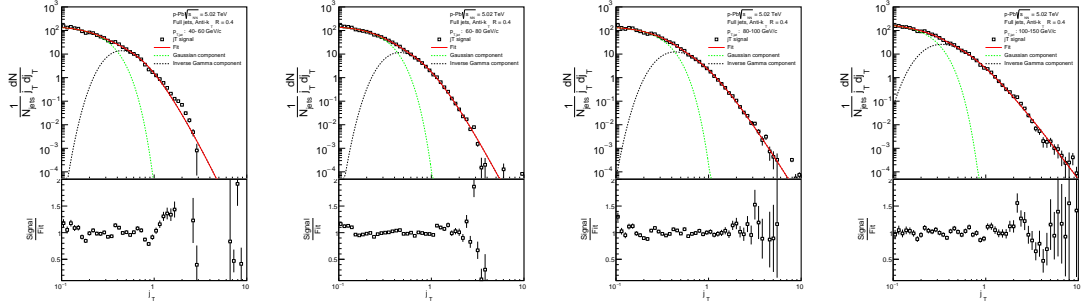


Figure 48: j_T signal with random background subtraction fits in different jet p_T bins

are shown in figure 51. The dotted lines are at $\pm 8\%$ for both components. These are taken to be the systematic uncertainty related to unfolding.

Several other systematic checks were performed with the Bayesian unfolding procedure. They are described in the following sections. As these are small compared to the main uncertainty they are not included separately.

5.2.1 Effect of number of iterations

The iterative unfolding algorithm permits the change of number of iterations. The unfolding procedure was carried out using different numbers of iterations. The results from these different cases are shown in Fig. 52. The results are compared to the default unfolding algorithm with 4 iterations. The difference in results

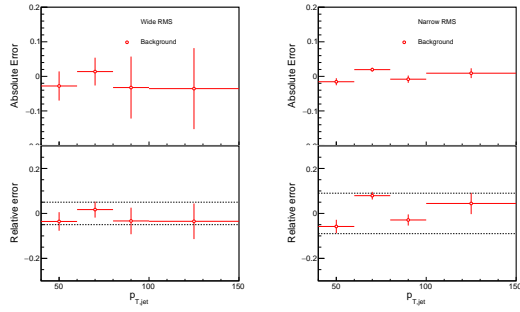


Figure 49: Differences between perpendicular cone and random background subtraction in the resulting RMS values.

Figure 50: Resulting signal distributions from SVD unfolding with the perpendicular cone background methods. These are compared to the results from the Bayesian algorithm to estimate the systematic uncertainty.

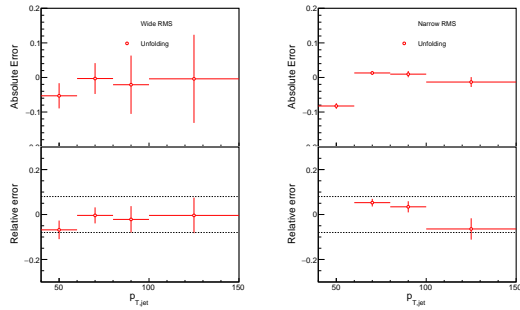


Figure 51: Differences between Bayesian and SVD unfolding in the resulting RMS values

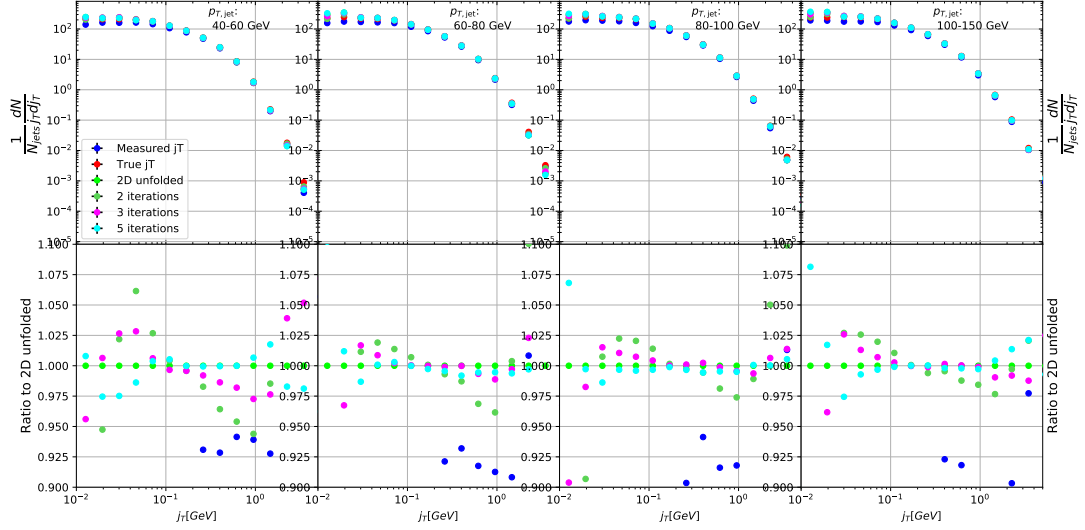


Figure 52: Unfolding with different number of iterations

Figure 53: Effect of changing prior from true distribution in PYTHIA to the unfolded distribution. [Missing figure](#)

1945 between the different cases is mostly less than 2.5%.

1946 5.2.2 Effect of different prior

1947 The iterative algorithm requires a prior estimate of the shape of the distribution.
 1948 As a default prior the truth (particle level) distribution is used. To test the effect
 1949 of changing the prior we instead use the unfolded j_T distribution as prior. The
 1950 results are compared to the unfolding algorithm with the default prior. This is
 1951 shown in Fig. 53 The difference in results between the different cases is mostly less
 1952 than 2.5%.

1953 5.2.3 Effect of p_T truncation

1954 As an additional check the unfolding is carried out with different $p_{T\text{jet}}$ truncation
 1955 values. By default the full range of $p_{T\text{jet}} > 5\text{GeV}$ is used. We test the unfolding
 1956 by only using the response matrix for $p_{T\text{jet}} > 10\text{GeV}$. The results of this test are
 1957 shown in Fig. 54. The effects are strongest in the lower $p_{T\text{jet}}$ bins. Also in this
 1958 case the difference is less than 2.5 % in all $p_{T\text{jet}}$ bins.

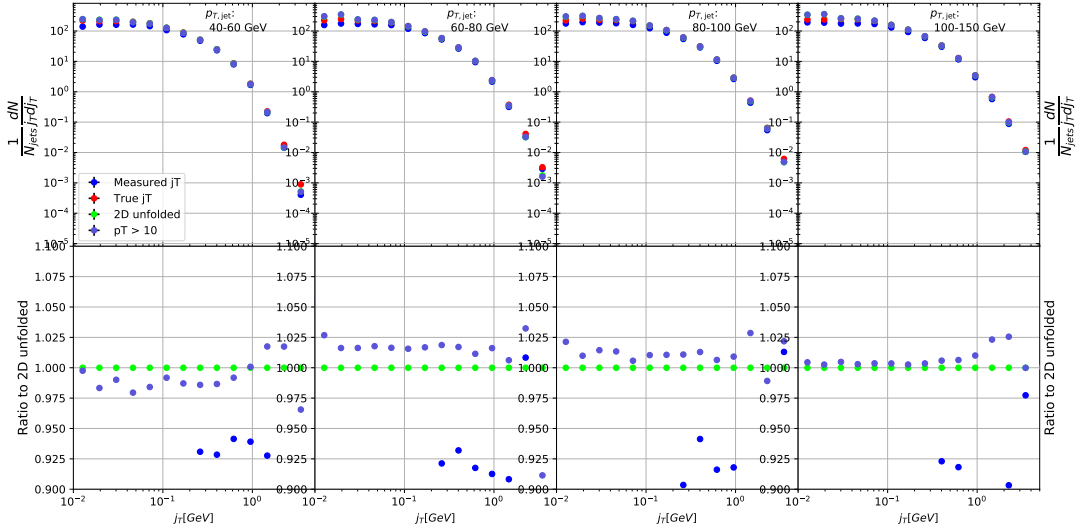


Figure 54: Effect of changing minimum jet p_T used in unfolding from 5 to 10 GeV

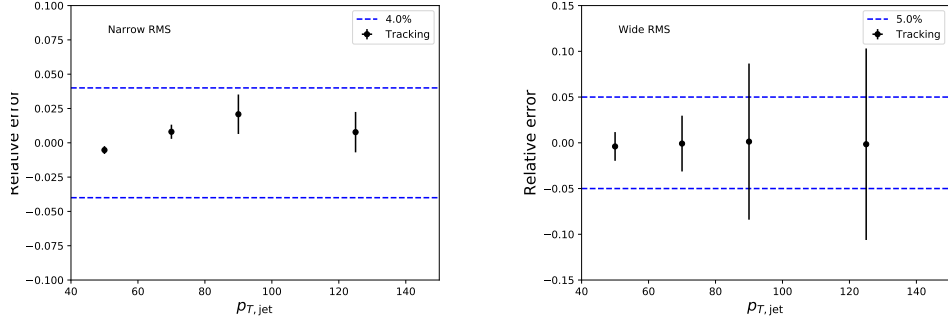


Figure 55: Relative systematic errors resulting from tracking efficiency uncertainty.

1959 5.3 Tracking

1960 Systematic effects originating from uncertainty in the tracking efficiency are es-
 1961 timated through a PYTHIA simulation, where an artificial inefficiency of 3% is
 1962 introduced i.e. 3 % of tracks are randomly removed from each event. The effect
 1963 of this artificial inefficiency is shown in Fig. 55. The systematic uncertainties as-
 1964 signed to tracking efficiency are 4 % for the narrow component and 5 % for the
 1965 wide component.

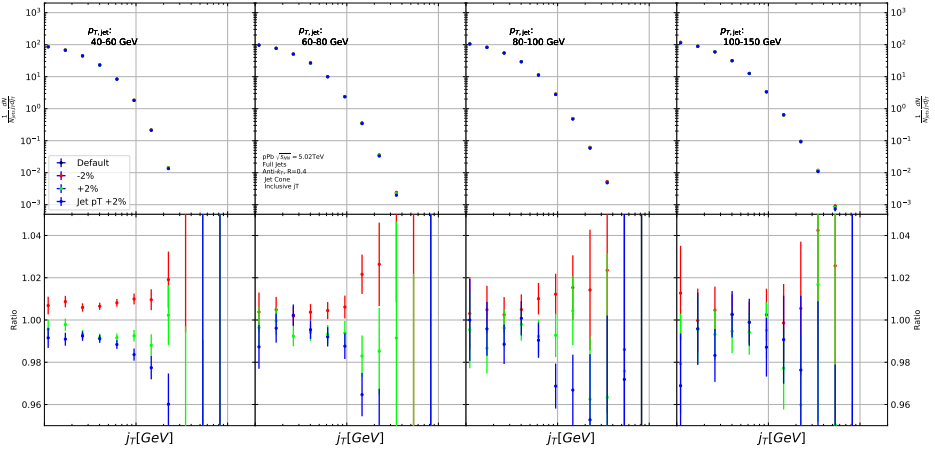


Figure 56: Results from PYTHIA simulations with Cluster energies scaled up and down by 2 %. Additionally jet momenta were scaled by 2 % when determining the jet p_T bin.

1966 5.4 EMCAL clusters

1967 The analysis uses EMCAL clusters only in the reconstruction of jets. Thus the only
 1968 way uncertainty in EMCAL performance can affect the results is through modifica-
 1969 tion of jet momentum or axis.

1970 Uncertainty related to the EMCAL energy scale was estimated by scaling cluster
 1971 energies up and down by 2 % in a PYTHIA particle level simulation. Similarly
 1972 the jet momentum was scaled by $\pm 2\%$ when determining the jet p_T bin. In the
 1973 analysis EMCAL is used only in jet reconstruction, not for calculating j_T . The only
 1974 ways EMCAL uncertainty can affect the analysis are changes in jet energy and jet
 1975 axis. Jet axis shouldn't significantly change, so the main contribution should be
 1976 changes in jet p_T bin.

1977 The resulting differences in the inclusive j_T distributions are shown in Fig. 56.
 1978 Qualitatively the effect of scaling cluster energies is the same as scaling the jet
 1979 energies.

1980 Like in the previous cases fits are performed for the unscaled case and for cases
 1981 with $\pm 2\%$ scaling. The resulting systematic uncertainties are shown in Fig. 57.
 1982 The uncertainty is taken to be 1% for both components.

1983 5.5 Summary/Combining systematics

1984 The different source of the systematic uncertainty are considered as uncorrelated
 1985 and the values of each source are summed in quadrature.

1986 Resulting systematic errors are shown in table 6. The different source of the

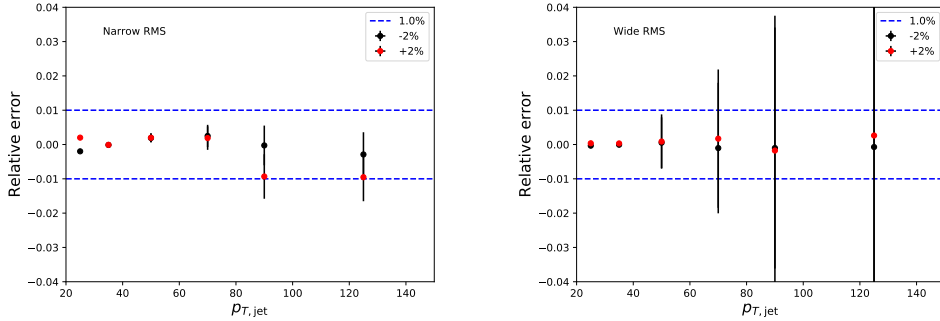


Figure 57: Relative systematic errors resulting from cluster energy uncertainty.

¹⁹⁸⁷ systematic uncertainty are considered to be uncorrelated and are thus combined
¹⁹⁸⁸ bin-by-bin in quadrature to get the total systematic errors. The resulting uncer-
¹⁹⁸⁹ tainty is approximately 9 % for the wide component RMS and 12 % for the narrow
component RMS.

Table 6: Summary of systematic errors

Systematic	Wide RMS	Narrow RMS
Background	5 %	9 %
Unfolding	8 %	8 %
Tracking	4 %	5 %
EMCal	1 %	1 %
Total	10 %	13%

¹⁹⁹⁰

¹⁹⁹¹ 5.6 Additional checks

¹⁹⁹² 5.6.1 Comparison between A and C side

¹⁹⁹³ In 2013 there were issues with tracking. To rule out effects on j_T distributions
¹⁹⁹⁴ a study was performed comparing j_T distributions between A and C side. (In
¹⁹⁹⁵ the p–Pb configuration the proton beam is travelling from A to C) No systematic
¹⁹⁹⁶ differences were observed. Figure 58 shows the comparison between inclusive dis-
¹⁹⁹⁷ tributions between the different sides, both for minimum bias and EMCal triggered
¹⁹⁹⁸ datasets.

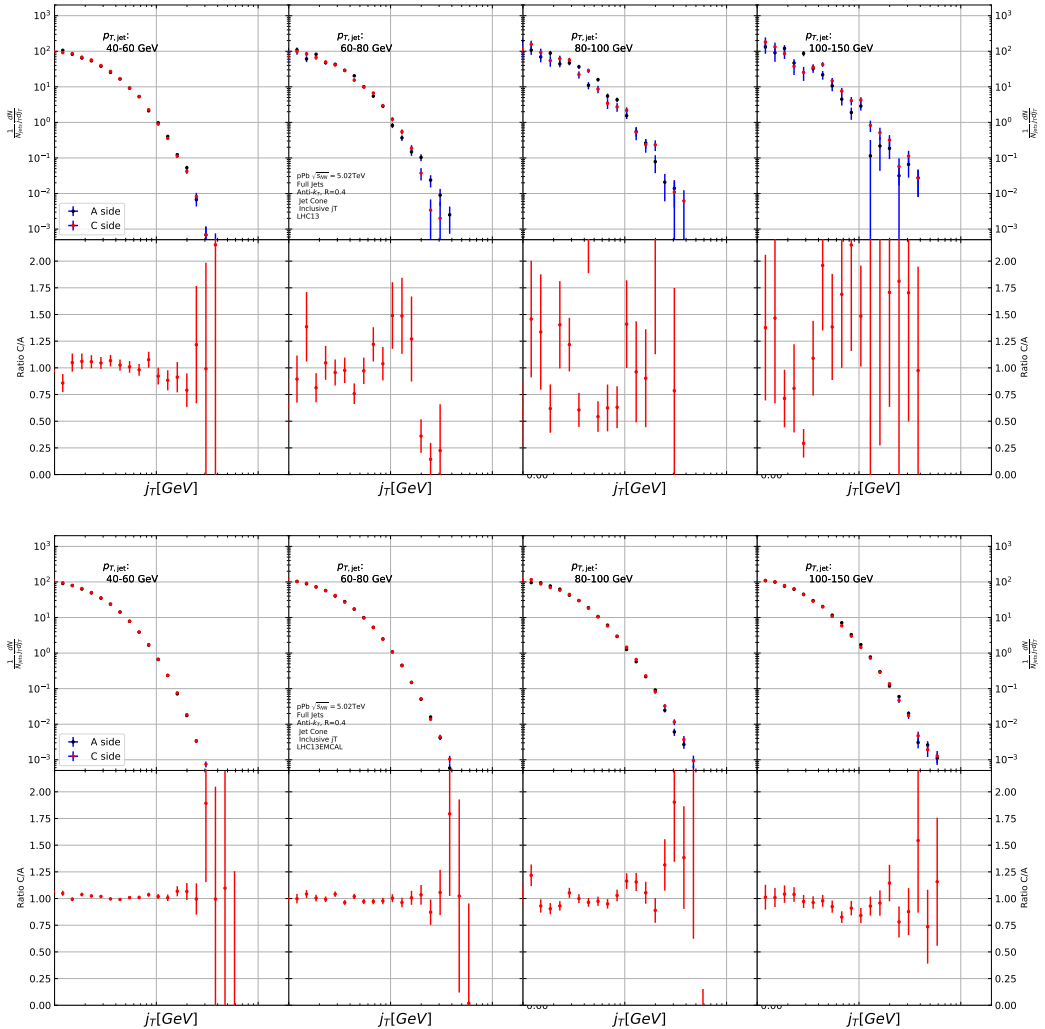


Figure 58: Comparison of inclusive j_T distributions between A and C side for minimum bias and EMCAL triggered data.

1999 6 Results

2000 In this section I present the final results for j_T signals. After unfolding and sub-
 2001 tracting the background contribution we get the final j_T distributions. Figure 70
 2002 shows j_T distributions for two different $p_{T,jet}$ bins with $60 \text{ GeV} < p_{T,jet} < 80 \text{ GeV}$
 2003 and $100 \text{ GeV} < p_{T,jet} < 150 \text{ GeV}$. Additional $p_{T,jet}$ bins are shown in appendix A.
 2004 It is clear that the distributions get wider with increasing $p_{T,jet}$. In part this is
 2005 explained by kinematics; In a jet cone the cone size sets limits on the possible j_T
 2006 values. For a given $p_{T,track}$ the maximum j_T value is approximately

$$j_{T,\max} \approx R \cdot p_{T,track}, \quad (78)$$

2007 using the small angle approximation.

2008 We fit the distribution using the two component fit function presented in
 2009 Sec. 4.5. These are also shown in Fig. 70. Aside from statistical fluctuations
 2010 the fits describe the data well. It should be noted that fitting a Gaussian alone
 2011 would produce the same result as the Gaussian component in the combined fit
 2012 function.

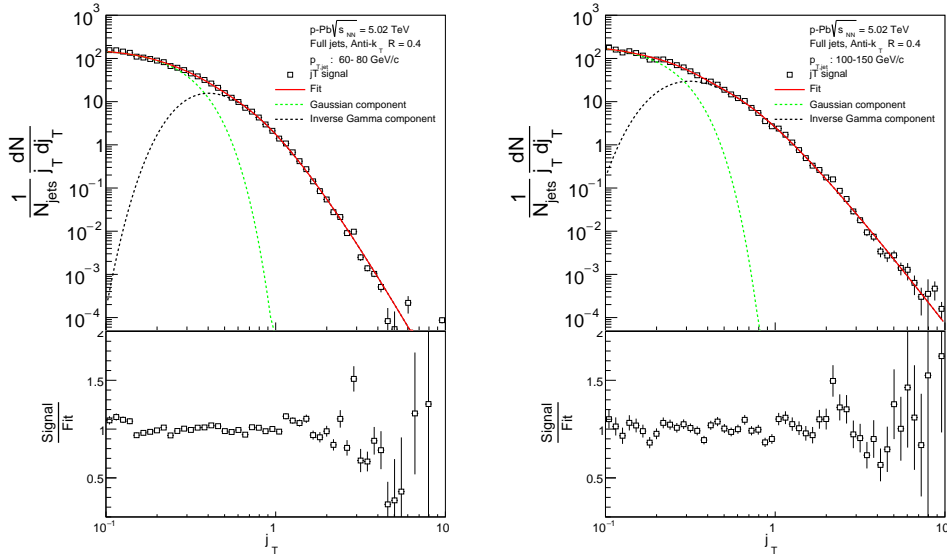
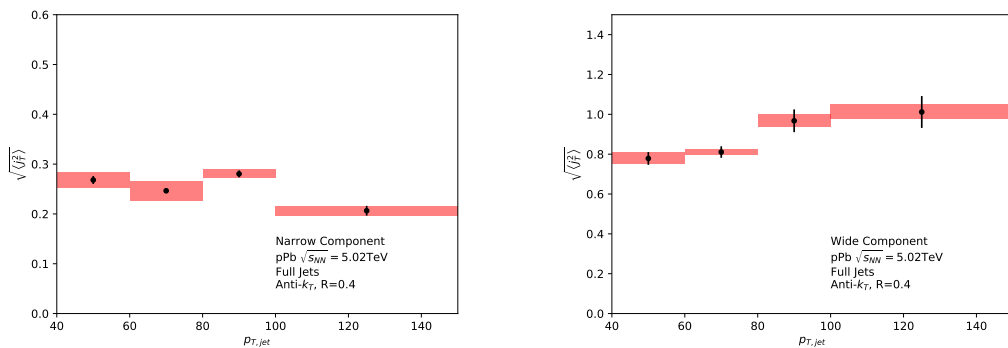


Figure 59: j_T signal distributions fitted with the two component model in different jet p_T bins

2013 To characterise the widening of the j_T distribution we can then extract the
 2014 RMS values of the fits. Resulting RMS values with systematic errors are shown
 2015 separately for the two components in Fig. 60. Here it is seen that the width of

2016 the narrow component shows no or only a weak dependence on the transverse
 2017 momentum of the jet, $p_{T,jet}$. The RMS value of the wide component on the other
 2018 hand increases with increasing $p_{T,jet}$.

2019 Figure 61 shows RMS values for both components combined and overlaid with
 2020 PYTHIAand Hewig simulations. As seen in the figure all the PYTHIAmodels re-
 2021 produce the data well, both the wide and narrow component. Herwig, on the
 2022 other hand, seems to produce significantly wider j_T distributions and this differ-
 2023 ence seems to get larger with increasing $p_{T,jet}$. For the narrow component Herwig
 gives a good representation of the data.



2024 Figure 60: RMS values extracted from the fits for the Gaussian (narrow) and inverse gamma (wide) components. Wide component RMS increases with increasing $p_{T,jet}$ while the narrow component RMS stays constant.

2025

2025 6.1 High multiplicity

2026 The analysis was repeated taking only events with high multiplicity. Three dif-
 2027 ferent multiplicity percentile cuts were used; 10 %, 1 % and 0.1 %. We used
 2028 ZDC(TODO) as a centrality estimator. As argued in section 1.5.3 the zero-degree
 2029 energy deposit should provide a centrality estimator with minimal bias from jet
 2030 production, as it should be measure of the number of spectator nucleons. Result-
 2031 ing j_T signal distributions are shown Fig. 62. As the statistics are limited in the
 2032 high multiplicity runs, it was hard to achieve stable fits to the distributions. Thus
 2033 the RMS values are not shown.

2034 From the figure one can observe no systematic modification when tighter mul-
 2035 tiplicity cuts are introduced. There is a hint of a dip at $j_T \approx 2$, but it is well
 2036 within statistical error bars. This is also the region where the signal is most sen-
 2037 sitive to background subtraction. Higher multiplicity events will naturally have a
 2038 higher background contribution. Background estimation is done separately for the

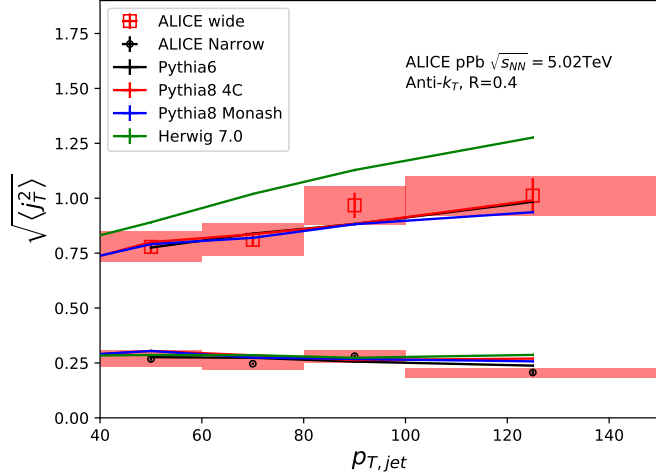


Figure 61: RMS values extracted from the fits are compared to Monte Carlo models. PYTHIA reproduces the data well for both the narrow and wide components. Herwig produces wider distributions.

2039 multiplicity bins. Thus it is not expected that different backgrounds would cause
2040 a difference, but this possibility can't be ruled out.

2041 The observation is in line with previous results. As described in Sec. 1.5 no
2042 conclusive evidence of jet modification in high multiplicity p–Pb collisions has been
2043 observed. Most jet observables show no difference between pp and p–Pb collisions.

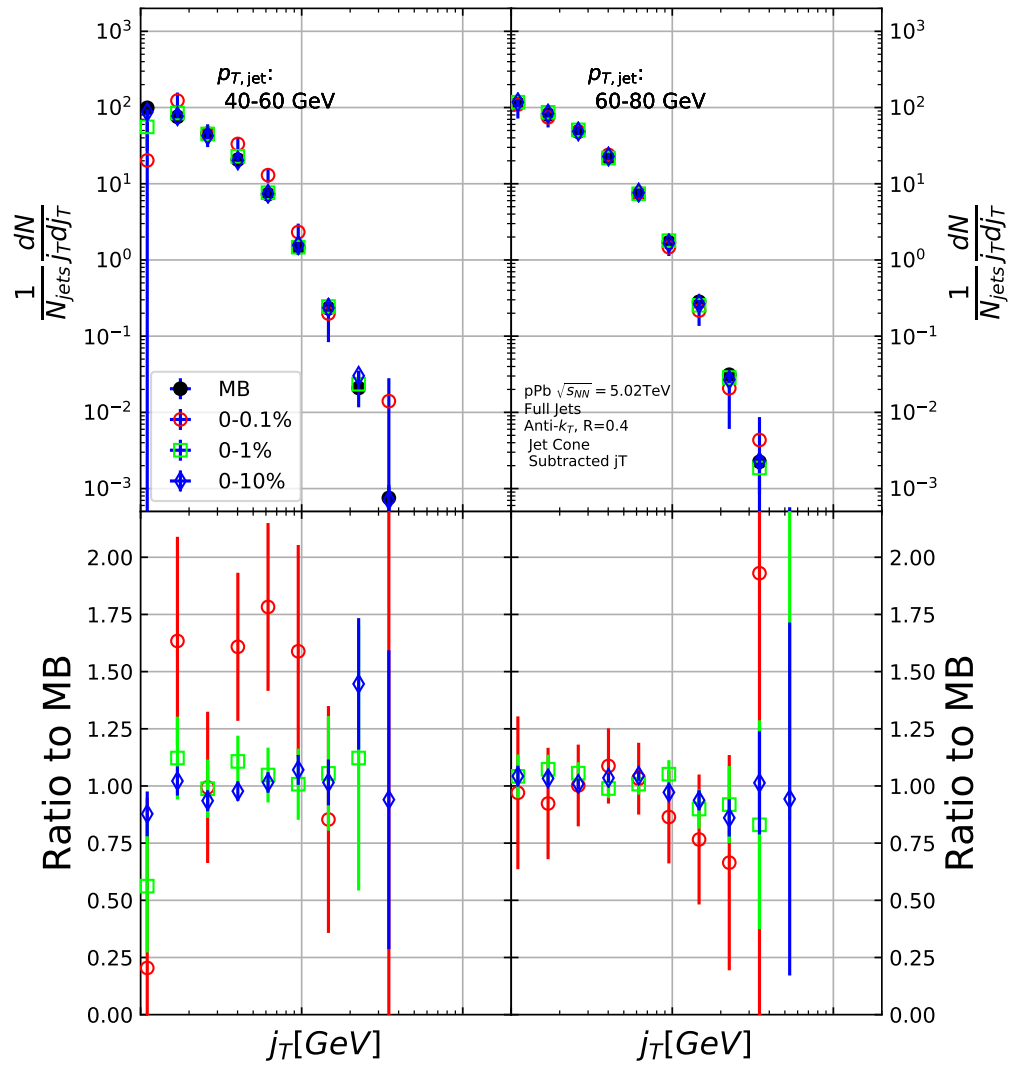


Figure 62: j_T distributions for high multiplicity p–Pb events. No systematic change between the multiplicity percentiles can be observed. [Replace figure with ZDC results](#)

2044 7 Discussion

2045 7.1 Comparing dihadron and jet j_T results

2046 The jet fragmentation transverse momentum j_T has been studied previously at
 2047 ALICE using dihadron correlations [226]. The study took the leading hadron in
 2048 each event and calculated j_T for any near-side tracks with respect to the leading
 2049 hadron. Thus there is no kinematical limit to j_T from the jet cone. In the analysis
 2050 the background shape is estimated using pairs with large $\Delta\eta$. The normalisation of
 2051 the background is done when fitting the j_T distribution. The inclusive distribution
 2052 is fitted with a three component function, where one of the components is the
 2053 background contribution. After subtracting the background, what remains is the
 2054 signal distribution characterised by the two components. The resulting signal
 2055 distribution from the analysis is shown in Fig. 63. The analysis was the first to
 2056 introduce this factorisation of j_T into components.

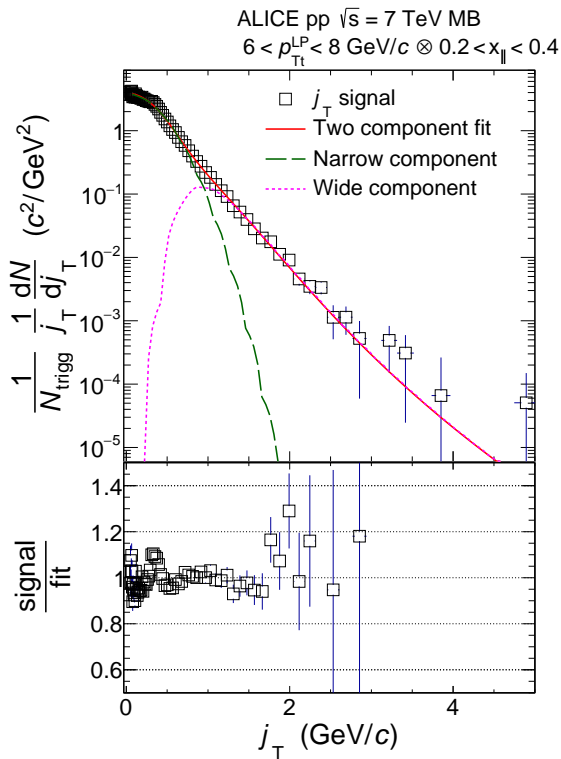


Figure 63: Measured j_T signal distribution using dihadron correlations. The distribution is fitted

2057 The RMS results from the fitting in both pp and p–Pb collisions are shown in
 2058 Fig. 64. Qualitatively the results are similar to jet j_T results. The RMS value of

the wide component has an increasing trend with respect to $p_{\text{T}}/p_{\text{Tjet}}$, while the RMS value of the narrow component stays constant. Both components are well described by PYTHIA simulations. As seen in the figures there is no difference between pp and p–Pb results in the dihadron analysis.

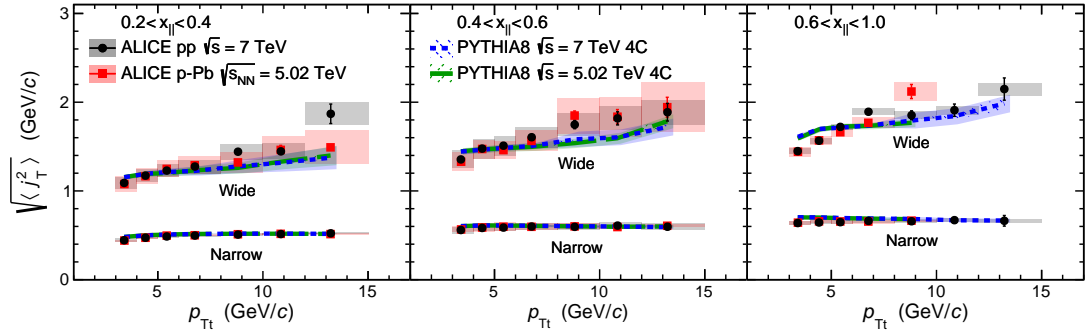


Figure 64: RMS values of the narrow and wide j_{T} components in the dihadron correlation analysis. Results from pp collisions at $\sqrt{s} = 7 \text{ TeV}$ (circular symbols) and from p–Pb collisions at $\sqrt{s_{\text{NN}}} = 5.02 \text{ TeV}$ (square symbols) are compared to PYTHIA 8 tune 4C simulations at $\sqrt{s} = 7 \text{ TeV}$ (short dashed line) and at $\sqrt{s} = 5.02 \text{ TeV}$ (long dashed line). Different panels correspond to different x_{\parallel} bins with $0.2 < x_{\parallel} < 0.4$ on the left, $0.4 < x_{\parallel} < 0.6$ in the middle, and $0.6 < x_{\parallel} < 1.0$ on the right. The statistical errors are represented by bars and the systematic errors by boxes. [226]

Comparison to RMS values in dihadron analysis [226] is shown in figure 65. For comparison the dihadron trigger p_{T} bins are converted to jet p_{T} bins and vice versa. Bin-by-bin comparison is still not possible, but general features can be identified.

The trends are similar in dihadron and jet j_{T} results. Wide component RMS values tend to increase with increasing $p_{\text{T,trigger}}/p_{\text{Tjet}}$. Narrow component RMS increases slightly in dihadron analysis but not in jet j_{T} . In the dihadron analysis this changes slightly between x_{\parallel} bins; In larger x_{\parallel} bins the narrow component RMS is closer to constant.

The most striking difference is that dihadron j_{T} gives wider distributions with larger RMS values. In jet analysis the cone size limits width and thus the RMS values. The effect of this limitation can be studied by changing the cone size as is described in section 7.1.1.

Additionally the leading track is an imperfect estimate of the jet/original parton. Because the leading track in general is at an angle compared to the jet axis, the resulting j_{T} values are different. In practice the jet axis found by the jet finding algorithm tends to minimize the average j_{T} of jet constituents. Thus the yield

2080 at high j_T is limited and the RMS values are smaller. The effect of having the
 2081 leading hadron as reference instead of the jet axis is discussed in section 7.1.2

2082 Lastly the results from the dihadron analysis are done in $p_{T\text{trigger}}$ bins. This
 2083 favours hard jets, i.e. jets where the leading hadron carries a large momentum
 2084 fraction and the jet multiplicity is small. In $p_{T\text{jet}}$ bins jets are more likely to be
 2085 soft, i.e. they have a small leading momentum fraction and high multiplicity jets.

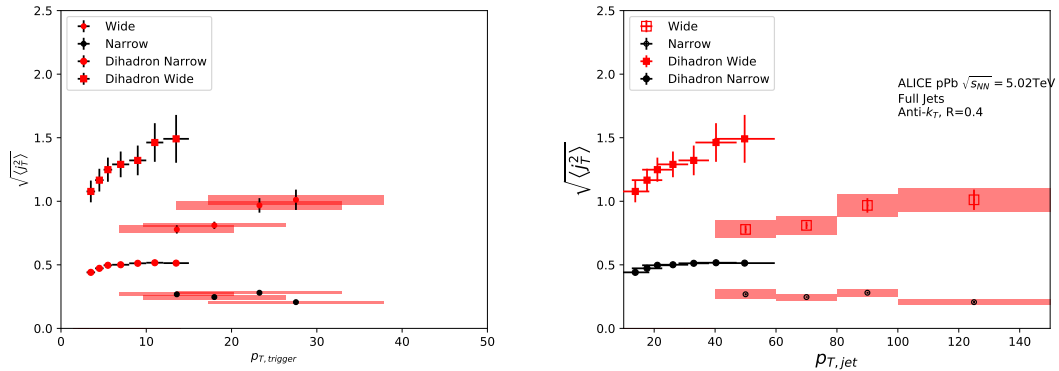


Figure 65: Jet j_T results are compared to results obtained in the dihadron analysis. Dihadron trigger p_T bins are converted to jet p_T bins using observed mean $p_{T\text{jet}}$ values in $p_{T\text{trigger}}$ bins. Dihadron results are for $0.2 < x_{||} < 0.4$

2086 7.1.1 Different R parameters

2087 The size of the jet cone gives a limit for j_T . For a track with a fixed momentum
 2088 p this is a hard limit. This is conveniently seen as $j_{T,\text{max}}$ can be given in terms of
 2089 cone size R and momentum p . In the small angle approximation limit

$$j_{T,\text{max}} \approx p \cdot R. \quad (79)$$

2090 Thus for tracks with $p_{T,\text{track}} < p_{T0}$, must be $j_T < p_{T0} \cdot R$. This illustrated in Fig. 66
 2091

2092 We studied the effect of cone sizes on j_T distribution in a PYTHIA simulation.
 2093 Results of the individual distributions values from this simulation are shown in
 2094 Fig. 67. The increase of high j_T with increasing cone size, R is clearly seen in the
 2095 individual j_T distributions. At low j_T there is no systematic change.

2096 When looking at the RMS values from wide component we see an increase
 2097 or decrease of about 10% when going from $R = 0.4$ to $R = 0.5$ or $R = 0.3$,
 2098 respectively. This is seen in Fig. 68. The message from narrow component RMS
 2099 values is less clear. At low jet p_T the behaviour is similar, but at high p_T the order
 2100 is reversed.

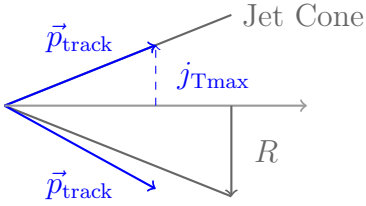


Figure 66: j_T has maximum value defined by the cone size and track momentum \vec{p}_{track}

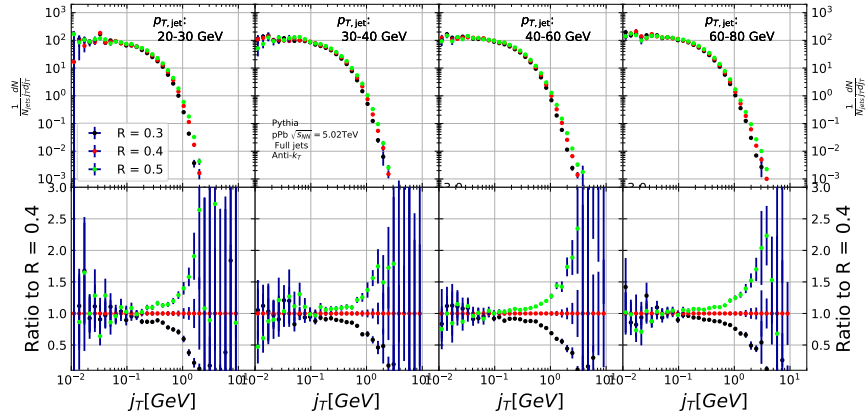


Figure 67: Effect of changing cone size on j_T distributions. The change is done both for the R parameter in the anti- k_T algorithm, and for the size of the cone where j_T is calculated.

2101 7.1.2 Leading tracks versus jet

2102 In comparison to the leading hadron the jet axis from jet reconstruction should
 2103 provide a better estimate of the original parton. Because the leading track in
 2104 general is at an angle compared to the jet axis, the resulting j_T values are different.
 2105 In practice the jet axis found by the jet finding algorithm tends to minimise the
 2106 average j_T of jet constituents, as at least the hardest constituents should be close to
 2107 the jet axis. Thus the yield at high j_T is limited and the RMS values are smaller.
 2108 On the other hand, when using the leading hadron as reference, it is naturally
 2109 missing from the set of tracks for which j_T is calculated. This causes a decrease
 2110 in the yield at low j_T .

2111 We performed a PYTHIA study where j_T was calculated with respect to the
 2112 leading track momentum, instead of the jet axis. The results are shown in Fig. 69.
 2113 The resulting j_T distributions are significantly wider than j_T distributions from
 2114 using the jet axis as reference. The effect seems to be larger than the effect seen

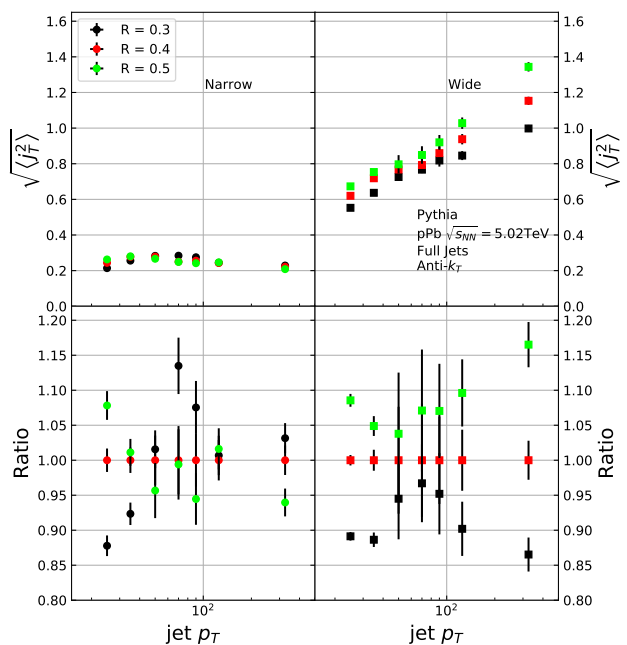


Figure 68: Effect of changing R parameter in jet finding on narrow and wide component RMS values. Wide component RMS values increase with increasing cone size.

₂₁₁₅ in comparing different R values.

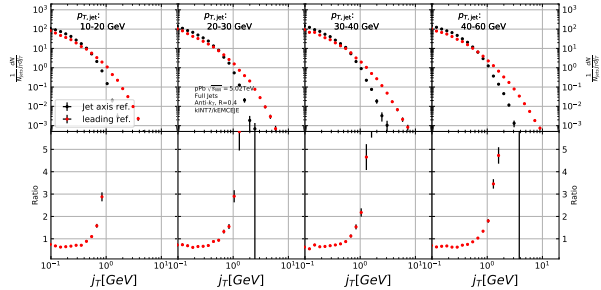


Figure 69: Results of calculating j_T with respect to the leading hadron, instead of the jet axis. The assumption is that because the leading hadron is an imperfect estimate of the jet axis, low j_T tracks should on average be shifted to higher j_T .

2116 8 Summary

2117 In this thesis I have studied the jet fragmentation transverse momentum in
2118 $\sqrt{s_{NN}} = 5.02$ TeV p–Pb collisions. The analysis was performed using jets
2119 reconstructed with the anti- k_T algorithm. The resulting j_T distributions were
2120 fitted with a two component function, which enabled separating two distinct
2121 components. Width of the narrow component was found to depend only weakly, if
2122 at all, on jet p_T . The narrow component has been associated with hadronisation.
2123 This is consistent with the assumption that hadronisation is universal, i.e. it
2124 doesn't depend on the hard scattering.

2125 The width of the wide component was found to increase for increasing $p_{T,jet}$.
2126 This is in part explained by the changing kinematical limits when going to higher
2127 $p_{T,jet}$ which allows higher $p_{T,track}$. Additionally the larger phase space allows
2128 stronger parton splitting.

2129 Both the narrow and wide component RMS values were well described by
2130 PYTHIA , but Herwig gave larger RMS values for the wide component than data.
2131 PYTHIA and Herwig have different algorithms for the showering. In the narrow
2132 component there was no difference between the models. Both describe the data
2133 well. This component was associated with hadronisation. At least in this con-
2134 text the different hadronisation algorithms of PYTHIA(string model) and Herwig
2135 (cluster model) give similar results.

2136 Similar analysis has been performed with dihadron correlations [226]. Although
2137 a direct comparison between the results is not possible, they are qualitatively com-
2138 patible with each other. The difference is understood to come from the different j_T
2139 reference, the cone size limitation in jet j_T analysis and the kinematical bias that
2140 comes from different binning. The dihadron analysis saw no difference between
2141 results in pp and p–Pb datasets and concluded that there were no cold nuclear
2142 matter effects. The same is expected to be true for the jet j_T . This is further
2143 supported by the agreement between PYTHIA and data as PYTHIA results are for
2144 pp collisions.

2145 To study possible QGP effects in high multiplicity p–Pb collisions the analysis
2146 was repeated using different multiplicity cuts. No effect was seen in any of the
2147 multiplicity cuts. However, with the statistics available, the effect should be quite
2148 large ($\gtrapprox 20\%$) to be visible. No other jet observables have shown conclusive
2149 evidence of modification in high multiplicity p–Pb events.

2150 Naturally the next step would be extending the analysis to Pb–Pb data. Jet
2151 analysis in a heavy-ion collision with significant contributions from the underlying
2152 event has proved challenging [5]. However, experimental methods have improved in
2153 recent years. For the j_T analysis presented in this thesis the main challenge would
2154 be the background subtraction method. Because of anisotropic flow in heavy ion
2155 collisions the background inside the jet cone and a cone perpendicular to it would

2156 be different. It's unclear if the perpendicular cone method can be modified or if a
2157 completely new approach is required.

2158 It has been shown that in Pb–Pb collisions jets become softer and wider because
2159 of medium-induced radiation [5]. On the other hand, the hot medium suppresses
2160 gluon jets more than quark jets. This has the opposite effect, narrowing jets, as
2161 gluon jets are naturally wider than quark jets [227]. How these different different
2162 effects combine in j_T needs to be studied.

₂₁₆₃ Appendices

₂₁₆₄ A Additional graphs

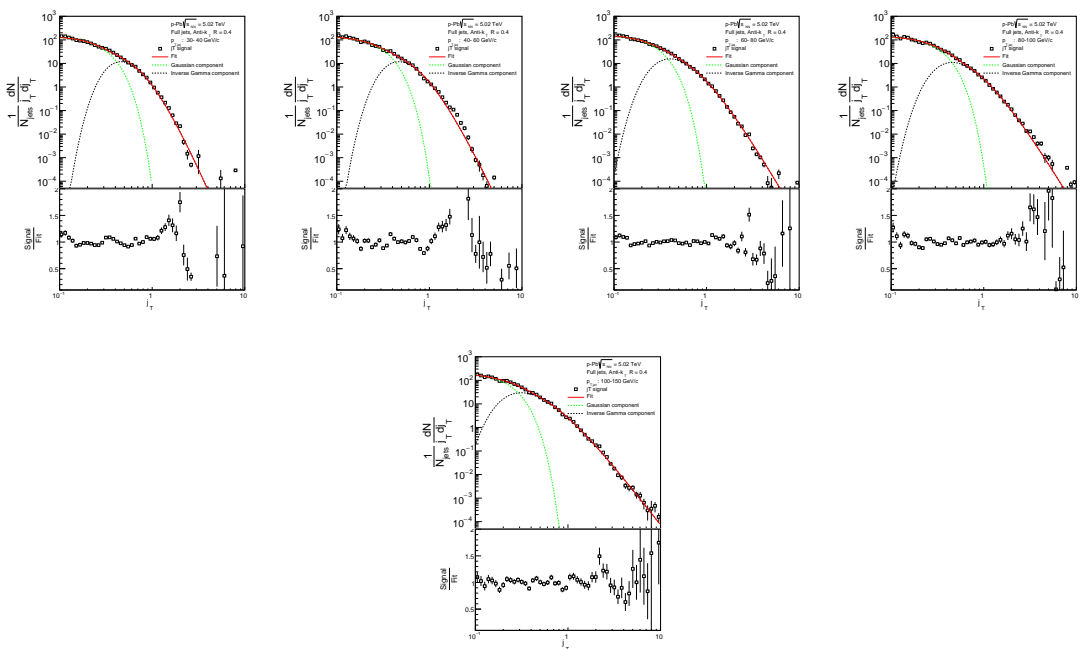


Figure 70: j_T signal fits in different jet p_T bins

²¹⁶⁵ References

- ²¹⁶⁶ [1] D. J. Gross and F. Wilczek, Physical Review D **8**, 3633 (1973).
- ²¹⁶⁷ [2] Particle Data Group, M. Tanabashi *et al.*, Phys. Rev. **D98**, 030001 (2018).
- ²¹⁶⁸ [3] E. Shuryak, Phys. Reps. **61**, 71 (1980).
- ²¹⁶⁹ [4] D. H. Perkins, *Introduction to high energy physics* (, 1982).
- ²¹⁷⁰ [5] M. Connors, C. Nattrass, R. Reed, and S. Salur, Rev. Mod. Phys. **90**, 025005 (2018), 1705.01974.
- ²¹⁷² [6] J. L. Nagle and W. A. Zajc, Ann. Rev. Nucl. Part. Sci. **68**, 211 (2018), 1801.03477.
- ²¹⁷⁴ [7] E. S., Monatshefte für Mathematik und Physik **26**, A38 (1915).
- ²¹⁷⁵ [8] P. A. M. Dirac and N. H. D. Bohr, Proceedings of the Royal Society of London. Series A, Containing Papers of a Mathematical and Physical Character **114**, 243 (1927), <https://royalsocietypublishing.org/doi/pdf/10.1098/rspa.1927.0039>.
- ²¹⁷⁹ [9] S. Tomonaga, Prog. Theor. Phys. **1**, 27 (1946).
- ²¹⁸⁰ [10] J. S. Schwinger, Phys. Rev. **75**, 651 (1948), [,59(1948)].
- ²¹⁸¹ [11] J. S. Schwinger, Phys. Rev. **74**, 1439 (1948), [,36(1948)].
- ²¹⁸² [12] R. P. Feynman, Phys. Rev. **74**, 1430 (1948).
- ²¹⁸³ [13] M. L. Krauss, *The Greatest Story Ever Told—So Far: Why Are We Here?* (, 2017).
- ²¹⁸⁵ [14] S. L. Glashow, J. Iliopoulos, and L. Maiani, Phys. Rev. **D2**, 1285 (1970).
- ²¹⁸⁶ [15] A. Salam and J. C. Ward, Phys. Lett. **13**, 168 (1964).
- ²¹⁸⁷ [16] S. Weinberg, Phys. Rev. Lett. **19**, 1264 (1967).
- ²¹⁸⁸ [17] G. P. S. Occhialini and C. F. Powell, (1987), [Nature159,186(1947)].
- ²¹⁸⁹ [18] C. M. G. Lattes, G. P. S. Occhialini, and C. F. Powell, Nature **160**, 453 (1947), [,99(1947)].
- ²¹⁹¹ [19] R. Bjorklund, W. Crandall, B. J. Moyer, and H. York, Phys. Review **77**, 213 (1950).

- 2193 [20] O. Chamberlain, E. Segré, C. Wiegand, and T. Ypsilantis, Phys. Rev. **100**,
2194 947 (1955).
- 2195 [21] B. Cork, G. R. Lambertson, O. Piccioni, and W. A. Wenzel, Phys. Rev.
2196 **104**, 1193 (1957).
- 2197 [22] L. W. Alvarez *et al.*, Phys. Rev. Lett. **2**, 215 (1959).
- 2198 [23] R. Armenteros, K. Barker, C. Butler, A. Cachon, and C. York, The London,
2199 Edinburgh, and Dublin Philosophical Magazine and Journal of Science **43**,
2200 597 (1952), <https://doi.org/10.1080/14786440608520216>.
- 2201 [24] A. Bonetti, R. L. Setti, M. Panetti, and G. Tomasini, Il Nuovo Cimento
2202 (1943-1954) **10**, 1736 (1953).
- 2203 [25] R. Plano, N. Samios, M. Schwartz, and J. Steinberger, Il Nuovo Cimento
2204 (1955-1965) **5**, 216 (1957).
- 2205 [26] W. B. Fowler, R. P. Shutt, A. M. Thorndike, and W. L. Whittemore, Phys.
2206 Rev. **91**, 1287 (1953).
- 2207 [27] W. Heisenberg, Zeitschrift für Physik **77**, 1 (1932).
- 2208 [28] M. Gell-Mann, Phys. Rev. **125**, 1067 (1962).
- 2209 [29] V. E. Barnes *et al.*, Phys. Lett. **12**, 134 (1964).
- 2210 [30] M. Gell-Mann, Phys. Lett. **8**, 214 (1964).
- 2211 [31] G. Zweig, An SU(3) model for strong interaction symmetry and its break-
2212 ing. Version 2, in *DEVELOPMENTS IN THE QUARK THEORY OF*
2213 *HADRONS. VOL. 1. 1964 - 1978*, edited by D. Lichtenberg and S. P. Rosen,
2214 pp. 22–101, 1964.
- 2215 [32] O. Greenberg, Phys. Rev. Lett. **13**, 598 (1964).
- 2216 [33] H. Fritzsch and M. Gell-Mann, eConf **C720906V2**, 135 (1972), hep-
2217 ph/0208010.
- 2218 [34] Crystal Ball Collaboration, D. Williams *et al.*, Phys. Rev. **D38**, 1365 (1988).
- 2219 [35] W. Krolikowski, Nuovo Cim. **A27**, 194 (1975).
- 2220 [36] M. Breidenbach *et al.*, Phys. Rev. Lett. **23**, 935 (1969).
- 2221 [37] The nobel prize in physics 1990, <https://www.nobelprize.org/prizes/physics/1990/summary/>,
2222 Accessed: Mon. 8 Apr 2019.

- ²²²³ [38] J. D. Bjorken, Phys. Rev. **179**, 1547 (1969).
- ²²²⁴ [39] J. D. Bjorken and E. A. Paschos, Phys. Rev. **185**, 1975 (1969).
- ²²²⁵ [40] R. P. Feynman, Phys. Rev. Lett. **23**, 1415 (1969), [,494(1969)].
- ²²²⁶ [41] D. J. Gross and F. Wilczek, Physical Review Letters **30**, 1343 (1973).
- ²²²⁷ [42] H. D. Politzer, Physical Review Letters **30**, 1346 (1973).
- ²²²⁸ [43] D. J. Gross and F. Wilczek, Physical Review D **9**, 980 (1974).
- ²²²⁹ [44] H. Georgi and H. D. Politzer, Physical Review D **9**, 416 (1974).
- ²²³⁰ [45] The nobel prize in physics 2004, <https://www.nobelprize.org/prizes/physics/2004/summary/>,
²²³¹ Accessed: Mon. 8 Apr 2019.
- ²²³² [46] H. Fritzsch, M. Gell-Mann, and H. Leutwyler, Physics Letters B **47**, 365
²²³³ (1973).
- ²²³⁴ [47] SLAC-SP-017, J. E. Augustin *et al.*, Phys. Rev. Lett. **33**, 1406 (1974), [Adv.
²²³⁵ Exp. Phys.5,141(1976)].
- ²²³⁶ [48] E598, J. J. Aubert *et al.*, Phys. Rev. Lett. **33**, 1404 (1974).
- ²²³⁷ [49] C. Bacci *et al.*, Phys. Rev. Lett. **33**, 1408 (1974), [Erratum: Phys. Rev.
²²³⁸ Lett.33,1649(1974)].
- ²²³⁹ [50] J. D. Bjorken and S. L. Glashow, Phys. Lett. **11**, 255 (1964).
- ²²⁴⁰ [51] I. Flegel and P. Söding, CERN courier (2004).
- ²²⁴¹ [52] R. Brandelik *et al.*, Physics Letters B **86**, 243 (1979).
- ²²⁴² [53] J. K. L. MacDonald, Phys. Rev. **43**, 830 (1933).
- ²²⁴³ [54] C. Berger *et al.*, Physics Letters B **86**, 418 (1979).
- ²²⁴⁴ [55] M. Kobayashi and T. Maskawa, Prog. Theor. Phys. **49**, 652 (1973).
- ²²⁴⁵ [56] The nobel prize in physics 2008, <https://www.nobelprize.org/prizes/physics/2008/summary/>,
²²⁴⁶ Accessed: Mon. 8 Apr 2019.
- ²²⁴⁷ [57] S. W. Herb *et al.*, Phys. Rev. Lett. **39**, 252 (1977).
- ²²⁴⁸ [58] CDF, F. Abe *et al.*, Phys. Rev. Lett. **74**, 2626 (1995), hep-ex/9503002.

- 2249 [59] D0, S. Abachi *et al.*, Phys. Rev. Lett. **74**, 2422 (1995), hep-ex/9411001.
- 2250 [60] J. Collins and M. Perry, Phys. rev. Lett. **34**, 1353 (1975).
- 2251 [61] K. Rajagopal, SLAC Beam Line **31-2**, 9 (2001).
- 2252 [62] P. Kovtun, D. Son, and A. Starinets, Phys.Rev.Lett. **94**, 111601 (2005), hep-th/0405231.
- 2254 [63] R. A. Lacey *et al.*, Phys. Rev. Lett. **98**, 092301 (2007).
- 2255 [64] E. Lofgren, *ACCELERATOR DIVISION ANNUAL REPORTS, 1 JULY 1972 12/31/1974* (, 1975).
- 2257 [65] D. S. Barton, Heavy ion program at bnl: Ags, rhic, in *Proc. 1987 Particle Accelerator Conference, Washington, D.C., March, 1987*, 1987.
- 2259 [66] I. Vitev and M. Gyulassy, Phys.Rev.Lett. **89**, 252301 (2002), hep-ph/0209161.
- 2261 [67] A. Kovalenko *et al.*, Status of the nuclotron, in *Proceedings of EPAC Vol. 94*, pp. 161–164, 1994.
- 2263 [68] New state of matter created at cern, <https://home.cern/news/press-release/cern/new-state-matter-created-cern>, Accessed: Sat. 6 Apr 2019.
- 2265 [69] NA61/SHINE, K. Grebieszkow, PoS **CPOD2013**, 004 (2013).
- 2266 [70] PHENIX Collaboration, K. Adcox *et al.*, Nucl.Phys. **A757**, 184 (2005), nucl-ex/0410003.
- 2268 [71] STAR Collaboration, J. Adams *et al.*, Nucl.Phys. **A757**, 102 (2005), nucl-ex/0501009.
- 2270 [72] BRAHMS Collaboration, I. Arsene *et al.*, Nucl.Phys. **A757**, 1 (2005), nucl-ex/0410020.
- 2272 [73] B. Back *et al.*, Nucl.Phys. **A757**, 28 (2005), nucl-ex/0410022.
- 2273 [74] LHCb, E. Maurice, Fixed-target physics at LHCb, in *5th Large Hadron Collider Physics Conference (LHCP 2017) Shanghai, China, May 15-20, 2017*, 2017, 1708.05184.
- 2276 [75] S. A. Voloshin, A. M. Poskanzer, and R. Snellings, (2008), 0809.2949.
- 2277 [76] S. A. Voloshin, A. M. Poskanzer, A. Tang, and G. Wang, Phys.Lett. **B659**, 537 (2008), 0708.0800.

- 2279 [77] H. Holopainen, H. Niemi, and K. J. Eskola, Phys.Rev. **C83**, 034901 (2011),
2280 1007.0368.
- 2281 [78] ALICE Collaboration, Phys. Rev. C **88**, 044909 (2013).
- 2282 [79] M. L. Miller, K. Reygers, S. J. Sanders, and P. Steinberg,
2283 Ann.Rev.Nucl.Part.Sci. **57**, 205 (2007), nucl-ex/0701025.
- 2284 [80] R. Glauber, Lectures in theoretical physics, 1959.
- 2285 [81] A. Białłas, M. Bleszyński, and W. Czyż, Nuclear Physics B **111**, 461 (1976).
- 2286 [82] PHENIX Collaboration, S. Afanasiev *et al.*, Phys.Rev. **C80**, 054907 (2009),
2287 0903.4886.
- 2288 [83] ALICE, B. Abelev *et al.*, Phys. Rev. **C88**, 044909 (2013), 1301.4361.
- 2289 [84] D. Kharzeev, E. Levin, and M. Nardi, Nucl. Phys. **A747**, 609 (2005), hep-
2290 ph/0408050.
- 2291 [85] W.-T. Deng, X.-N. Wang, and R. Xu, Phys. Rev. **C83**, 014915 (2011),
2292 1008.1841.
- 2293 [86] P. Romatschke, Int.J.Mod.Phys. **E19**, 1 (2010), 0902.3663.
- 2294 [87] K. A. *et al.* [ALICE Collaboration], Phys. Rev. Lett **106** (2011), 032301.
- 2295 [88] J.-Y. Ollitrault, Phys. Rev. D **46**, 229 (1992).
- 2296 [89] J.-Y. Ollitrault, Phys.Rev. D **48**, 1132 (1993), hep-ph/9303247.
- 2297 [90] U. Heinz and P. Kolb, Nucl. Phys. **A702**, 269 (2002).
- 2298 [91] A. Mocsy and P. Sorensen, (2010), 1008.3381.
- 2299 [92] A. P. Mishra, R. K. Mohapatra, P. Saumia, and A. M. Srivastava, Phys.Rev.
2300 **C77**, 064902 (2008), 0711.1323.
- 2301 [93] T. Abbott *et al.*, Phys. Rev. Lett. **70**, 1393 (1993).
- 2302 [94] S. Voloshin and Y. Zhang, Z.Phys. **C70**, 665 (1996), hep-ph/9407282.
- 2303 [95] K. A. *et al.* [ALICE Collaboration], Phys. Rev. Lett. **107** (2011), 032301.
- 2304 [96] K. Aamodt *et al.*, Physics Letters B **708**, 249 (2012).
- 2305 [97] B. Schenke, S. Jeon, and C. Gale, Phys.Lett. **B702**, 59 (2011), 1102.0575.

- ²³⁰⁶ [98] L. LD, Izv. Akad. Nauk Ser. Fiz. **17**, 51 (1953).
- ²³⁰⁷ [99] J. D. Bjorken, Phys. Rev. D **27**, 140 (1983).
- ²³⁰⁸ [100] G. Baym, B. L. Friman, J. P. Blaizot, M. Soyeur, and W. Czyz, Nucl. Phys. **A407**, 541 (1983).
- ²³¹⁰ [101] H. von Gersdorff, L. McLerran, M. Kataja, and P. V. Ruuskanen, Phys. Rev. D **34**, 794 (1986).
- ²³¹² [102] V. N. Gribov and L. N. Lipatov, Sov. J. Nucl. Phys. **15**, 438 (1972), [Yad. Fiz. 15, 781(1972)].
- ²³¹⁴ [103] G. Altarelli and G. Parisi, Nucl. Phys. **B126**, 298 (1977).
- ²³¹⁵ [104] Y. L. Dokshitzer, Sov. Phys. JETP **46**, 641 (1977), [Zh. Eksp. Teor. Fiz. 73, 1216(1977)].
- ²³¹⁷ [105] T. Sjöstrand and P. Z. Skands, Eur. Phys. J. **C39**, 129 (2005), hep-ph/0408302.
- ²³¹⁹ [106] A. Buckley *et al.*, Phys. Rept. **504**, 145 (2011), 1101.2599.
- ²³²⁰ [107] Y. I. Azimov, Y. L. Dokshitzer, V. A. Khoze, and S. I. Trovan, Zeitschrift für Physik C Particles and Fields **27**, 65 (1985).
- ²³²² [108] B. Andersson, G. Gustafson, G. Ingelman, and T. Sjöstrand, Physics Reports **97**, 31 (1983).
- ²³²⁴ [109] M. Bahr *et al.*, Eur. Phys. J. **C58**, 639 (2008), 0803.0883.
- ²³²⁵ [110] ALICE Collaboration, K. Aamodt *et al.*, Phys.Lett. **B696**, 30 (2011), 1012.1004.
- ²³²⁷ [111] WA98 Collaboration, M. Aggarwal *et al.*, Eur.Phys.J. **C23**, 225 (2002), nucl-ex/0108006.
- ²³²⁹ [112] D. G. d'Enterria, Phys.Lett. **B596**, 32 (2004), nucl-ex/0403055.
- ²³³⁰ [113] PHENIX Collaboration, A. Adare *et al.*, Phys.Rev.Lett. **101**, 232301 (2008), 0801.4020.
- ²³³² [114] STAR Collaboration, J. Adams *et al.*, Phys.Rev.Lett. **91**, 172302 (2003), nucl-ex/0305015.
- ²³³⁴ [115] A. Dainese, C. Loizides, and G. Paic, Eur.Phys.J. **C38**, 461 (2005), hep-ph/0406201.

- ²³³⁶ [116] I. Vitev, J.Phys. **G30**, S791 (2004), hep-ph/0403089.
- ²³³⁷ [117] C. A. Salgado and U. A. Wiedemann, Phys.Rev. **D68**, 014008 (2003), hep-ph/0302184.
- ²³³⁹ [118] N. Armesto, A. Dainese, C. A. Salgado, and U. A. Wiedemann, Phys.Rev. **D71**, 054027 (2005), hep-ph/0501225.
- ²³⁴¹ [119] T. Renk, H. Holopainen, R. Paatelainen, and K. J. Eskola, Phys.Rev. **C84**, 014906 (2011), 1103.5308.
- ²³⁴³ [120] CMS Collaboration, S. Chatrchyan *et al.*, Eur.Phys.J. **C72**, 1945 (2012), 1202.2554.
- ²³⁴⁵ [121] PHENIX, S. S. Adler *et al.*, Phys. Rev. **C76**, 034904 (2007), nucl-ex/0611007.
- ²³⁴⁷ [122] PHENIX, A. Adare *et al.*, Phys. Rev. **C88**, 064910 (2013), 1309.4437.
- ²³⁴⁸ [123] ALICE, B. Abelev *et al.*, Phys. Lett. **B719**, 18 (2013), 1205.5761.
- ²³⁴⁹ [124] CMS, S. Chatrchyan *et al.*, Phys. Rev. Lett. **109**, 022301 (2012), 1204.1850.
- ²³⁵⁰ [125] W. H. H. Bethe and, Proc.Roy.Soc.Lond. **A146** (1934).
- ²³⁵¹ [126] L. D. Landau and I. Pomeranchuk, Dokl. Akad. Nauk Ser. Fiz. **92**, 535 (1953).
- ²³⁵³ [127] A. B. Migdal, Phys. Rev. **103**, 1811 (1956).
- ²³⁵⁴ [128] P. Bosted *et al.*, Quantum-mechanical suppression of bremsstrahlung*, 1993.
- ²³⁵⁵ [129] R. Baier, Y. L. Dokshitzer, A. H. Mueller, S. Peigne, and D. Schiff, Nucl. Phys. **B484**, 265 (1997), hep-ph/9608322.
- ²³⁵⁷ [130] A. Majumder and M. Van Leeuwen, Prog.Part.Nucl.Phys. **A66**, 41 (2011), 1002.2206.
- ²³⁵⁹ [131] F. Dominguez, C. Marquet, A. Mueller, B. Wu, and B.-W. Xiao, Nucl.Phys. **A811**, 197 (2008), 0803.3234.
- ²³⁶¹ [132] M. Gyulassy, P. Levai, and I. Vitev, Nucl.Phys. **B571**, 197 (2000), hep-ph/9907461.
- ²³⁶³ [133] U. A. Wiedemann, Nucl.Phys. **B588**, 303 (2000), hep-ph/0005129.

- ²³⁶⁴ [134] P. B. Arnold, G. D. Moore, and L. G. Yaffe, JHEP **0112**, 009 (2001), hep-ph/0111107.
- ²³⁶⁵
- ²³⁶⁶ [135] X.-N. Wang and X.-f. Guo, Nucl.Phys. **A696**, 788 (2001), hep-ph/0102230.
- ²³⁶⁷ [136] T. Sjostrand, S. Mrenna, and P. Z. Skands, Comput.Phys.Commun. **178**, 852 (2008), 0710.3820.
- ²³⁶⁸
- ²³⁶⁹ [137] I. Lokhtin and A. Snigirev, Eur.Phys.J. **C45**, 211 (2006), hep-ph/0506189.
- ²³⁷⁰ [138] N. Armesto, L. Cunqueiro, and C. A. Salgado, Nucl.Phys. **A830**, 271C (2009), 0907.4706.
- ²³⁷¹
- ²³⁷² [139] K. Zapp, G. Ingelman, J. Rathsman, J. Stachel, and U. A. Wiedemann, Eur.Phys.J. **C60**, 617 (2009), 0804.3568.
- ²³⁷³
- ²³⁷⁴ [140] T. Renk, Phys.Rev. **C79**, 054906 (2009), 0901.2818.
- ²³⁷⁵ [141] ALICE, J. Adam *et al.*, Phys. Lett. **B746**, 1 (2015), 1502.01689.
- ²³⁷⁶ [142] ATLAS, G. Aad *et al.*, Phys. Rev. Lett. **114**, 072302 (2015), 1411.2357.
- ²³⁷⁷ [143] CMS, V. Khachatryan *et al.*, Phys. Rev. **C96**, 015202 (2017), 1609.05383.
- ²³⁷⁸ [144] STAR, L. Adamczyk *et al.*, Phys. Rev. Lett. **112**, 122301 (2014), 1302.6184.
- ²³⁷⁹ [145] CMS, V. Khachatryan *et al.*, JHEP **02**, 156 (2016), 1601.00079.
- ²³⁸⁰ [146] A. Kurkela and U. A. Wiedemann, Phys. Lett. **B740**, 172 (2015), 1407.0293.
- ²³⁸¹ [147] JETSCAPE, Y. Tachibana *et al.*, Jet substructure modification in a QGP from a multi-scale description of jet evolution with JETSCAPE, 2018, 1812.06366.
- ²³⁸²
- ²³⁸³
- ²³⁸⁴ [148] P. Aurenche and B. G. Zakharov, Eur. Phys. J. **C71**, 1829 (2011), 1109.6819.
- ²³⁸⁵ [149] A. Beraudo, J. G. Milhano, and U. A. Wiedemann, Phys. Rev. **C85**, 031901 (2012), 1109.5025.
- ²³⁸⁶
- ²³⁸⁷ [150] A. Beraudo, J. G. Milhano, and U. A. Wiedemann, JHEP **07**, 144 (2012), 1204.4342.
- ²³⁸⁸
- ²³⁸⁹ [151] J. Casalderrey-Solana, Y. Mehtar-Tani, C. A. Salgado, and K. Tywoniuk, Phys. Lett. **B725**, 357 (2013), 1210.7765.
- ²³⁹⁰
- ²³⁹¹ [152] F. D'Eramo, M. Lekaveckas, H. Liu, and K. Rajagopal, JHEP **05**, 031 (2013), 1211.1922.
- ²³⁹²

- ²³⁹³ [153] A. Ayala, I. Dominguez, J. Jalilian-Marian, and M. E. Tejeda-Yeomans, Phys. Rev. **C94**, 024913 (2016), 1603.09296.
- ²³⁹⁵ [154] CMS, S. Chatrchyan *et al.*, Phys. Rev. **C84**, 024906 (2011), 1102.1957.
- ²³⁹⁶ [155] E735, T. Alexopoulos *et al.*, Phys. Rev. **D48**, 984 (1993).
- ²³⁹⁷ [156] MiniMax, T. C. Brooks *et al.*, Phys. Rev. **D61**, 032003 (2000), hep-ex/9906026.
- ²³⁹⁹ [157] C. Shen, Z. Qiu, and U. Heinz, Phys. Rev. **C92**, 014901 (2015), 1502.04636.
- ²⁴⁰⁰ [158] PHENIX, A. Adare *et al.*, Phys. Rev. **C94**, 064901 (2016), 1509.07758.
- ²⁴⁰¹ [159] CMS, V. Khachatryan *et al.*, JHEP **09**, 091 (2010), 1009.4122.
- ²⁴⁰² [160] C. A. Salgado and J. P. Wessels, Ann. Rev. Nucl. Part. Sci. **66**, 449 (2016).
- ²⁴⁰³ [161] ATLAS, G. Aad *et al.*, Phys. Rev. Lett. **116**, 172301 (2016), 1509.04776.
- ²⁴⁰⁴ [162] ALICE, S. Acharya *et al.*, JHEP **09**, 032 (2017), 1707.05690.
- ²⁴⁰⁵ [163] C. Aidala *et al.*, Phys. Rev. **C95**, 034910 (2017), 1609.02894.
- ²⁴⁰⁶ [164] C. Shen, J.-F. Paquet, G. S. Denicol, S. Jeon, and C. Gale, Phys. Rev. **C95**, 014906 (2017), 1609.02590.
- ²⁴⁰⁸ [165] H. Niemi and G. S. Denicol, (2014), 1404.7327.
- ²⁴⁰⁹ [166] PHENIX, C. Aidala *et al.*, Nature Phys. **15**, 214 (2019), 1805.02973.
- ²⁴¹⁰ [167] PHENIX, S. S. Adler *et al.*, Phys. Rev. Lett. **91**, 072303 (2003), nucl-ex/0306021.
- ²⁴¹² [168] STAR, J. Adams *et al.*, Phys. Rev. Lett. **91**, 072304 (2003), nucl-ex/0306024.
- ²⁴¹³ [169] BRAHMS, I. Arsene *et al.*, Phys. Rev. Lett. **91**, 072305 (2003), nucl-ex/0307003.
- ²⁴¹⁵ [170] PHOBOS, B. B. Back *et al.*, Phys. Rev. Lett. **91**, 072302 (2003), nucl-ex/0306025.
- ²⁴¹⁷ [171] CMS, V. Khachatryan *et al.*, JHEP **04**, 039 (2017), 1611.01664.
- ²⁴¹⁸ [172] ATLAS, G. Aad *et al.*, Phys. Rev. **C90**, 044906 (2014), 1409.1792.
- ²⁴¹⁹ [173] X. Zhang and J. Liao, (2013), 1311.5463.

- ²⁴²⁰ [174] C. Park, C. Shen, S. Jeon, and C. Gale, Nucl. Part. Phys. Proc. **289-290**,
²⁴²¹ 289 (2017), 1612.06754.
- ²⁴²² [175] K. Tywoniuk, Nucl. Phys. **A926**, 85 (2014).
- ²⁴²³ [176] ALICE, J. Adam *et al.*, Phys. Rev. **C91**, 064905 (2015), 1412.6828.
- ²⁴²⁴ [177] F. Sikler, (2003), hep-ph/0304065.
- ²⁴²⁵ [178] 2019.
- ²⁴²⁶ [179] P. M. Watkins, Contemp. Phys. **27**, 291 (1986).
- ²⁴²⁷ [180] Cern experiments, 2019.
- ²⁴²⁸ [181] O. S. Brüning *et al.*, *LHC Design Report*CERN Yellow Reports: Monographs
²⁴²⁹ (CERN, Geneva, 2004).
- ²⁴³⁰ [182] ATLAS, G. Aad *et al.*, Phys. Lett. **B716**, 1 (2012), 1207.7214.
- ²⁴³¹ [183] CMS, S. Chatrchyan *et al.*, Phys. Lett. **B716**, 30 (2012), 1207.7235.
- ²⁴³² [184] LHCb, A. A. Alves, Jr. *et al.*, JINST **3**, S08005 (2008).
- ²⁴³³ [185] LHCf, O. Adriani *et al.*, JINST **3**, S08006 (2008).
- ²⁴³⁴ [186] TOTEM, G. Anelli *et al.*, JINST **3**, S08007 (2008).
- ²⁴³⁵ [187] MoEDAL, B. Acharya *et al.*, JHEP **08**, 067 (2016), 1604.06645.
- ²⁴³⁶ [188] T. ALICE Collaboration *et al.*, Journal of Instrumentation **3**, S08002 (2008).
- ²⁴³⁷ [189] ALICE, K. Aamodt *et al.*, Phys. Rev. Lett. **105**, 252301 (2010), 1011.3916.
- ²⁴³⁸ [190] ALICE, G. Dellacasa *et al.*, (2000).
- ²⁴³⁹ [191] ALICE, G. Dellacasa *et al.*, (1999).
- ²⁴⁴⁰ [192] ALICE, I. Belikov, EPJ Web Conf. **125**, 01004 (2016), 1607.01171.
- ²⁴⁴¹ [193] ALICE Collaboration, B. Abelev *et al.*, CERN Report No. CERN-LHCC-
²⁴⁴² 2012-012. LHCC-I-022. ALICE-UG-002, 2012 (unpublished).
- ²⁴⁴³ [194] Report No. CERN-LHCC-2015-001. ALICE-TDR-018, 2015 (unpublished).
- ²⁴⁴⁴ [195] The ALICE Collaboration, Report No. CERN-LHCC-2013-020. ALICE-
²⁴⁴⁵ TDR-016, 2013 (unpublished).

- ²⁴⁴⁶ [196] M. Vargyas, *Jet shape modification in Pb-Pb collisions at $\sqrt{s_{\text{NN}}} = 2.76 \text{ TeV}$ using two-particle correlations*, PhD thesis, University of Jyväskylä, 2018.
- ²⁴⁴⁸ [197] ALICE TPC upgrade, J. E. Brücken and T. E. Hildén, The GEM QA Protocol of the ALICE TPC Upgrade Project, in *5th International Conference on Micro Pattern Gas Detectors (MPGD2017) Temple University, Philadelphia, USA, May 22-26, 2017*, 2018, 1811.07043.
- ²⁴⁵² [198] T. Hildén *et al.*, Nucl. Instrum. Meth. **A770**, 113 (2015), 1704.06691.
- ²⁴⁵³ [199] ALICE Collaboration, P. Cortese, *ALICE transition-radiation detector: Technical Design Report*Technical Design Report ALICE (CERN, Geneva, 2001).
- ²⁴⁵⁶ [200] ALICE, G. Dellacasa *et al.*, (2000).
- ²⁴⁵⁷ [201] ALICE, S. Beole *et al.*, (1998).
- ²⁴⁵⁸ [202] for the ALICE, C. Zampolli, Particle Identification with the ALICE detector at the LHC, in *Proceedings, PLHC2012: Physics at the LHC 2012 (PLHC2012): Vancouver, BC, Canada, June 4-9, 2012*, 2012, 1209.5637.
- ²⁴⁶¹ [203] ALICE, G. Dellacasa *et al.*, (1999).
- ²⁴⁶² [204] ALICE, P. Cortese *et al.*, (2008).
- ²⁴⁶³ [205] J. Allen *et al.*, Report No. CERN-LHCC-2010-011. ALICE-TDR-14-add-1, 2010 (unpublished).
- ²⁴⁶⁵ [206] ALICE, P. Cortese *et al.*, (2004).
- ²⁴⁶⁶ [207] ALICE, A. I. Maevskaya, (2018), 1812.00594.
- ²⁴⁶⁷ [208] ALICE Collaboration, *ALICE Photon Multiplicity Detector (PMD): Technical Design Report*Technical Design Report ALICE (CERN, Geneva, 1999).
- ²⁴⁶⁹ [209] ACORDE, A. Fernández *et al.*, Nucl. Instrum. Meth. **A572**, 102 (2007), physics/0606051.
- ²⁴⁷¹ [210] ALICE, G. Dellacasa *et al.*, (1999).
- ²⁴⁷² [211] ALICE, S. Beole *et al.*, (1996).
- ²⁴⁷³ [212] J. Král, *Intrinsic transverse momentum distribution of jet constituents in p-Pb collisions at ALICE*, PhD thesis, University of Jyväskylä, 2014.

- 2475 [213] J. Kral, T. Awes, H. Muller, J. Rak, and J. Schambach, Nuclear Instruments
2476 and Methods in Physics Research Section A: Accelerators, Spectrometers,
2477 Detectors and Associated Equipment **693**, 261 (2012).
- 2478 [214] ALICE, K. Aamodt *et al.*, JINST **3**, S08002 (2008).
- 2479 [215] ALICE, B. B. Abelev *et al.*, Int. J. Mod. Phys. **A29**, 1430044 (2014),
2480 1402.4476.
- 2481 [216] ALICE, K. Aamodt *et al.*, JINST **5**, P03003 (2010), 1001.0502.
- 2482 [217] J. Alme *et al.*, Nucl. Instrum. Meth. **A622**, 316 (2010), 1001.1950.
- 2483 [218] R. Fruhwirth, Nucl. Instrum. Meth. **A262**, 444 (1987).
- 2484 [219] A. Maire, Track reconstruction principle in ALICE for LHC run I and run
2485 II. Principes de reconstruction de traces dans ALICE pour les runs I et II
2486 du LHC, General Photo, 2011.
- 2487 [220] ALICE, B. Abelev *et al.*, JHEP **03**, 053 (2012), 1201.2423.
- 2488 [221] ALICE, B. Abelev *et al.*, Phys. Lett. **B719**, 29 (2013), 1212.2001.
- 2489 [222] M. Cacciari, G. P. Salam, and G. Soyez, Eur. Phys. J. **C72**, 1896 (2012),
2490 1111.6097.
- 2491 [223] M. Cacciari, G. P. Salam, and G. Soyez, JHEP **04**, 063 (2008), 0802.1189.
- 2492 [224] T. Sjöstrand, S. Mrenna, and P. Z. Skands, Comput. Phys. Commun. **178**,
2493 852 (2008), 0710.3820.
- 2494 [225] Roounfold: Root unfolding framework, <http://hepunx.rl.ac.uk/~adye/software/unfold/RooUnfold.html>, 2013.
- 2496 [226] ALICE, S. Acharya *et al.*, JHEP **03**, 169 (2019), 1811.09742.
- 2497 [227] Y.-T. Chien and I. Vitev, JHEP **05**, 023 (2016), 1509.07257.